POLITECNICO
MILANO 1863

SCUOLA DI INGEGNERIA INDUSTRIALE
E DELL'INFORMAZIONE

A study on the fracture behaviour of a NBR/silica compound: effect of strain-induced softening and applied thermal treatment

TESI DI LAUREA MAGISTRALE IN

MATERIALS ENGINEERING AND NANOTECHNOLOGY

Author: **Alice Bianucci**

Student ID: 964882

Advisor: Claudia Marano

Co-advisor: Isabella Denora

Academic Year: 2021-2022

Abstract

This thesis work explores the mechanical behaviour of a silica-filled NBR compound, focusing on the changes induced in its response by the previous application of a deformation: the phenomenon is known as Mullins effect and is often referred to as strain-induced softening. It is generally studied by means of uniaxial tensile tests and, to our knowledge, no study on the effect of such strain-induced softening on the fracture behaviour of rubber compounds is reported in literature. As such, this work started with investigating the Mullins effect in uniaxial tension loading conditions and defining a thermal treatment that, as suggested by literature, could recover the stress-strain behaviour of the pristine material. In order to better understand if the thermal treatment could have any effect on the structure of the material, the effects of the thermal treatment on both tensile and fracture behaviour of the silica-filled NBR compound were studied in detail. Regarding the fracture, the study focused on both the crack initiation and the fracture propagation. The results showed that the thermal history significantly affects the starting point of the unstable propagation of the fracture process by reducing the fracture toughness. Its effect on the crack onset, instead, is quite limited. An attempt was made to correlate the behaviour observed in the crack propagation phase with a higher susceptibility to cavity formation when the material is thermally treated. It was also observed that a strain-induced softening caused a reduction in the fracture toughness. The same thermal treatment used to recover the Mullins effect in uniaxial tension was investigated for its ability to recover the fracture properties. Finally, from the study of the kinetics of the crack propagation, it was observed that the value of crack advancement required to start the unstable propagation phase was affected by neither the thermal history nor the strain-induced softening.

Keywords: Silica-filled NBR, Mullins effect, Fracture toughness, Cavities formation

Abstract in italiano

Questa tesi esplora il comportamento meccanico di una gomma NBR caricata con silice, concentrandosi sul cambiamento strutturale causato da una deformazione precedentemente applicata: questo fenomeno è noto come effetto Mullins ed è spesso indicato come *softening* indotto dalla deformazione. Generalmente viene studiato mediante prove di trazione uniassiale e, in base alla nostra conoscenza, in letteratura non è riportato alcuno studio riguardante l'effetto di tale *softening* sul comportamento a frattura del materiale. Pertanto, questo lavoro è iniziato con lo studio dell'effetto Mullins in condizioni di carico di trazione uniassiale e con la definizione di un trattamento termico che, come suggerito dalla letteratura, potesse recuperare il comportamento sforzo-deformazione del materiale pristino. Per capire meglio se il trattamento termico potesse avere qualche effetto sulla struttura del materiale, sono stati studiati in dettaglio gli effetti del trattamento termico sul comportamento a trazione e a frattura del materiale esaminato. Per quanto riguarda la frattura, lo studio si è concentrato sia sull'innesco che sulla propagazione della frattura. I risultati hanno mostrato che la storia termica influisce significativamente sul punto di inizio della propagazione instabile del processo di frattura, riducendo la tenacità a frattura. Il suo effetto sull'innesco della cricca, invece, è piuttosto limitato. Si è cercato di correlare il comportamento osservato nella fase di propagazione della cricca con una maggiore predisposizione alla formazione di cavità quando il materiale è trattato termicamente. È stato inoltre osservato che il *softening* indotto dalla deformazione causa una riduzione della tenacità a frattura. Lo stesso trattamento termico utilizzato per recuperare l'effetto Mullins in trazione uniassiale è stato studiato per la sua capacità di recuperare le proprietà a frattura. Infine, dallo studio della cinetica della propagazione della cricca, è stato osservato che il valore di avanzamento della cricca necessario per iniziare la fase di propagazione instabile non è influenzato né dalla storia termica né dal *softening* indotto dalla deformazione.

Parole chiave: NBR caricato con silice, Effetto Mullins, Tenacità a frattura, Formazione di cavità

Table of contents

Abstract ..... **i**

Abstract in italiano ..... **iii**

Table of contents ..... **v**

Introduction **1**

1 Theoretical background **3**

1.1. Elastomers 3

1.1.1. Thermodynamic approach 3

1.1.2. Statistical approach 4

1.1.3. Phenomenological approach 6

1.2. Rubber compound 8

1.2.1. Nitrile-butadiene rubber 8

1.2.2. Rubber curing 8

1.2.3. Filler reinforcement 10

1.3. Dissipative behaviour of rubbers 12

1.4. Mullins effect 13

1.4.1. Thermal recovery of Mullins effect 15

1.5. Fracture of rubber 18

1.6. Formation of cavities 21

2 Materials and methods **27**

2.1. Material 27

2.2. Preparation of specimens 28

2.3. Uniaxial tensile tests 31

2.4. Tests in pure shear loading condition 32

2.4.1. Loading-unloading cyclic tests 32
2.4.2. Fracture tests 33
2.5. Swelling tests 34
2.6. Digital Image Correlation analysis 35
3 Results and discussion 39
3.1. Characterization of the material 39
3.1.1. Monotonic uniaxial tensile tests 39
3.1.2. Crosslink density 43
3.2. Strain energy dissipation 44
3.3. Mullins effect 48
3.4. Thermal recovery of Mullins effect 49
3.5. Fracture tests 51
3.5.1. Effect of thermal treatment on fracture onset 56
3.5.2. Effect of thermal treatment on crack propagation 61
3.6. Crack length and crack growth rate 66
3.7. Formation of cavities 72
3.8. Stress softening in pure shear loading condition 76
4 Conclusions and future developments 85
Bibliography 89
List of Figures 97
List of Tables 101

Introduction

This thesis work is connected to a more comprehensive PhD project carried out by Isabella Denora. The research is part of the major project "Polymers4Hydrogen - Designed Polymers and their Composites for High Pressure Environments", in the framework of COMET – Competence Centers for Excellent Technologies (Austria). The project has the aim to design new polymeric materials to be used in the hydrogen infrastructure, in extreme conditions of temperature and pressure. Elastomers are usually used in some components of this infrastructure, such as seals and hoses. However, one of the major causes of failure in elastomers used in this type of applications is the rapid gas decompression (RGD). The elastomers investigated in the project are reinforced with fillers and have been modified in order to improve their RGD failure resistance. Our role in the project is the study of fracture properties of the elastomers under study, in relation to their structure (type of matrix, type and content of filler…). A possible correlation between their fracture properties and RGD failure resistance is also researched.

In order to define the mechanical properties required for the long-term employment of elastomers, the structural changes that occur in the material upon deformation must be taken into account. For example, when a previously stretched rubber is deformed for a second time, a reduction in the applied stress at the same strain level is observed: this effect is known in literature as Mullins effect, or strain-induced softening. The Mullins effect is often studied in relation to the uniaxial tensile behaviour of the material, and it has been demonstrated that the stress-strain curve can be recovered by swelling or by means of appropriate thermal treatments. However, how the strain-induced softening and its thermally induced recovery influence the fracture behaviour of the material is not reported in literature, to the best of my knowledge.

This thesis work focuses on the study of the fracture properties of a silica-filled NBR. More specifically, one of the aims is to investigate the effects that the thermal

treatments used to recover the Mullins effect in uniaxial tension have on the fracture behaviour of the material. Additionally, the effect of the strain induced softening on the fracture properties is investigated, and the thermally induced recovery of the fracture toughness is compared to the results obtained for the recovery of the uniaxial stress-strain behaviour.

The thesis is structured as follows.

Chapter 1 is dedicated to the theoretical background of the concepts that were used in the experimental work. A brief overview of the structure and properties of rubber compounds is presented. Particular attention was paid to a literature review about the recovery of the strain induced stress softening.

In Chapter 2, the materials and experimental methods used during the experimental work are described. Since one of the aims of the work is to compare materials with different thermal histories, details about the employed thermal treatments are provided.

In Chapter 3, the results of the experimental work are presented and discussed.

In Chapter 4, a summary of the main conclusions of the experimental work are presented, along with some possible future developments.

1 Theoretical background

1.1. Elastomers

The properties that set rubbers apart from other polymeric materials are their high deformability at low stress and their elastic behaviour, which allow them to undergo significant extension and recover their original dimensions with minimal or no residual deformation. More specifically, rubber elasticity has an entropic origin: when the material is stretched macroscopically, the chain configuration changes from the random coil, which characterizes the undeformed state, to an arrangement aligned along the direction of the deformation. Consequently, the state of disorder of the material decreases, which results in a decrease in entropy. When the applied force is removed, the material tends to increase its entropy level to return to its minimal free energy state.

This elastic behaviour is possible thanks to the structure that characterize this type of materials. Elastomers, indeed, are composed of polymeric chains linked to each other by the so-called crosslinks, which are formed during the vulcanization process. This allows the formation of a network that prevents the viscous sliding of the chains and allows the elastic recovery of the deformation when the load is removed.

Different approaches have been used to describe analytically the elasticity of rubbers: (i) the thermodynamic approach is based on thermodynamical considerations and focuses on the macroscopic behaviour of the material; (ii) the statistical approach, instead, focuses on the molecular structure of the material; (iii) the phenomenological approach is based on semi-empirical models.

1.1.1. Thermodynamic approach

In the thermodynamic approach the elasticity of rubbers is studied using energetic considerations. According to this approach, when the material is deformed at constant

temperature and pressure, the retraction force is given by an enthalpic and an entropic contribution

$$f = \left(\frac{\partial G}{\partial L}\right)_{T,P} = \left(\frac{\partial H}{\partial L}\right)_{T,P} - T\left(\frac{\partial S}{\partial L}\right)_{T,P} = \left(\frac{\partial H}{\partial L}\right)_{T,P} + T\left(\frac{\partial f}{\partial T}\right)_{P,L} \quad (1.1)$$

Equation 1.1 predicts a linear relationship between the force required to maintain the applied deformation (constant L) and the temperature. Experimental results at low strains, however, show a deviation from the expected linear behaviour: in particular, the force increases less quickly than expected, or even declines as the temperature rises. The latter phenomenon is known as thermoelastic inversion, and it is caused by the thermal expansion of the material. Figure 1.1 shows that for natural rubber the reversal in the slope of the stress-temperature plots occurs at an extension between 6% and 13%.

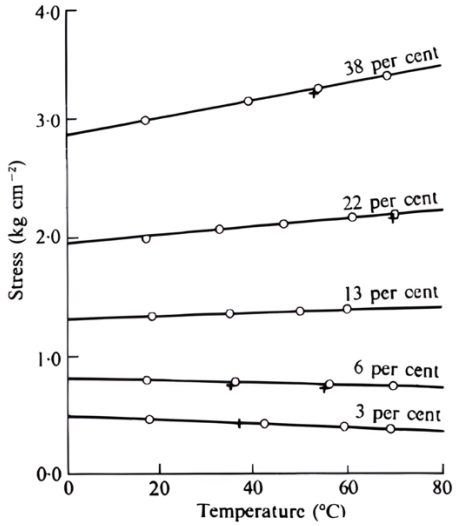

Figure 1.1. Stress-temperature curves obtained for natural rubber at elongations ranging between 3% and 38% [1].

1.1.2. Statistical approach

The thermodynamic approach set the basis for the development of the statistical theory, which allows to describe the mechanical behaviour of the rubber starting from molecular mechanics considerations.

The theory is based on treating the rubber macromolecules as Gaussian chains with one fixed end. If a phantom chain model is assumed, the distribution of end-to-end distances is given by

$$P(r) = \left[\frac{\beta^2}{\pi}\right]^{\frac{3}{2}} \exp(-\beta^2 r^2) \tag{1.2}$$

where r^2 is the mean square end-to-end distance and $\beta^2 = \frac{3}{2Nl^2}$, with N the number of links of length l in the chain.

In the so-called Kuhn model, the rubber is approximated to a network made of crosslinked sub-chains modelled as phantom chains. The assumptions upon which the molecular theory of rubber is based are the following:

- there is no change in volume upon deformation
- all the chains have the same connectivity
- the strain of the chains is coherent and proportional to the macroscopic strain of the material (affine deformation)
- the entropy of the network is equal to the sum of the entropies of the individual chains
- no entanglements, loops or dangling bonds are present

If these assumptions hold, the total work of deformation (W) is given by

$$W = \frac{1}{2} G(\lambda_1^2 + \lambda_2^2 + \lambda_3^3 - 3) \tag{1.3}$$

where λ_1, λ_2 and λ_3 are the stretch ratios in the three principal directions.

The term G represents the shear modulus, which depends on crosslink density and temperature according to the following relationship

$$G = Nk_BT = \frac{\rho RT}{M_c} \tag{1.4}$$

in which k_B is Boltzmann constant, ρ is the density of rubber, R is the constant of an ideal gas, and M_c is the average molecular weight between two crosslinks.

In the case of uniaxial tension $\lambda_1 = \lambda$ and $\lambda_2 = \lambda_3 = \frac{1}{\sqrt{\lambda}}$ therefore Equation 1.3 becomes

$$W = \frac{1}{2} G \left(\lambda^2 + \frac{2}{\lambda} - 3\right) \tag{1.5}$$

From Equation 1.5 it is possible to derive the constitutive equation of elasticity of rubbers

$$\sigma = \frac{dW}{d\lambda} = G\left(\lambda - \frac{1}{\lambda^2}\right) \tag{1.6}$$

Figure 1.2 shows the comparison between the theoretical behaviour predicted by the constitutive equation and the experimental data. The two curves are in agreement only up to $\lambda \approx 1.5$, while for $1.5 < \lambda < 6$ the experimental curve falls below the theoretical one. On the other hand, at higher elongations the experimental data show a stiffer behaviour than predicted; this is due to the limited extensibility of the polymeric chains.

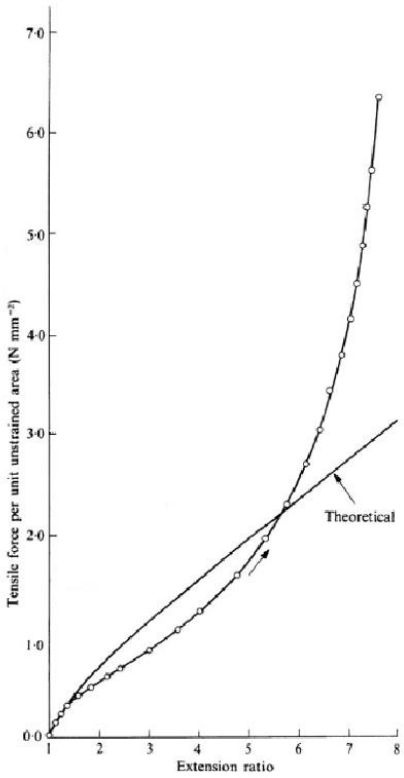

Figure 1.2. Comparison between the constitutive equation of elasticity (continuous line) and experimental data (dotted line) [2].

1.1.3. Phenomenological approach

In order to describe the behaviour of rubbers over a larger range of strains, a phenomenological approach is needed. Mooney was the first to use this kind of approach and developed the following semi-empirical model, which is known as

Mooney-Rivlin model and is valid under the assumptions of isotropy and incompressibility

$$\sigma = \left(C_1 + \frac{C_2}{\lambda}\right)\left(\lambda - \frac{1}{\lambda^2}\right) \tag{1.7}$$

Usually, the Mooney-Rivlin model is written in a more concise form using the reduced stress, which is defined as

$$\sigma^* = \frac{\sigma}{\lambda - \frac{1}{\lambda^2}} = C_1 + \frac{C_2}{\lambda} \tag{1.8}$$

Due to the limited extensibility of the chains, when the reduced stress is plotted as a function of λ^{-1}, a positive deviation from the linear trend predicted by Equation 1.8 is observed at high λ. Figure 1.3 shows the Mooney-Rivlin plots for natural rubber with increasing crosslink density: it can be observed that for rubbers with higher crosslink density the deviation from linearity is more pronounced and occurs at lower values of λ.

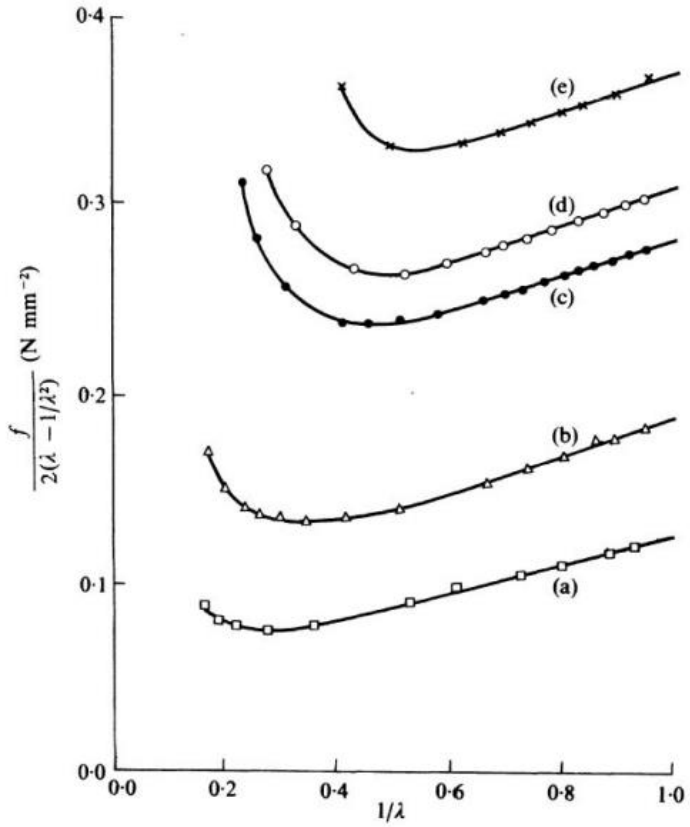

Figure 1.3. Mooney-Rivlin plots for natural rubber. Curves from (a) to (e) correspond to rubbers with increasing crosslink density [3].

1.2. Rubber compound

1.2.1. Nitrile-butadiene rubber

The material studied in this thesis is a nitrile-butadiene rubber, commonly known as NBR, which is an unsaturated synthetic copolymer of acrylonitrile and butadiene. Acrylonitrile content may vary between 18% and 50%. The polarity of the acrylonitrile monomer confers good resistance to fuels and oils. The glass transition temperature of NBR varies from -45°C to -25°C, increasing with the increase of the acrylonitrile content. Unlike other rubbers, such as natural rubber, nitrile rubber does not crystallize under strain. The unsaturation present in the butadiene groups causes susceptibility to oxygen and ozone attacks.

The ratio between acrylonitrile and butadiene groups plays a significant role in determining the properties of the rubber; besides the increase in T_g, an increase in the acrylonitrile content causes an increase in the heat resistance and strength, and a decrease in gas permeability.

1.2.2. Rubber curing

Vulcanization is a chemical process that allows the formation of junctions between the rubber chains, obtaining a chemically crosslinked molecular network. Vulcanization is the main responsible for the elastic behaviour of rubbers: indeed, the presence of the crosslinks prevents the viscous flow and allows the elastic recovery of the deformation when the load is removed.

The crosslinking process is usually carried out by heating the rubber compound containing the crosslinking agents in a compression moulding machine. The two most used crosslinking agents are sulphur and peroxides. The material studied in this thesis is crosslinked with sulphur. During the process, sulphur reacts with the unsaturated bonds present in the polymeric chains forming chemical crosslinks. The crosslinks can be in form of monosulphide ($-S-$), disulphide ($-S-S-$) or polysulphide ($-S_x-$); some loops and dangling bonds can also form. A schematic representation of a sulphur-crosslinked rubber is shown in Figure 1.4.

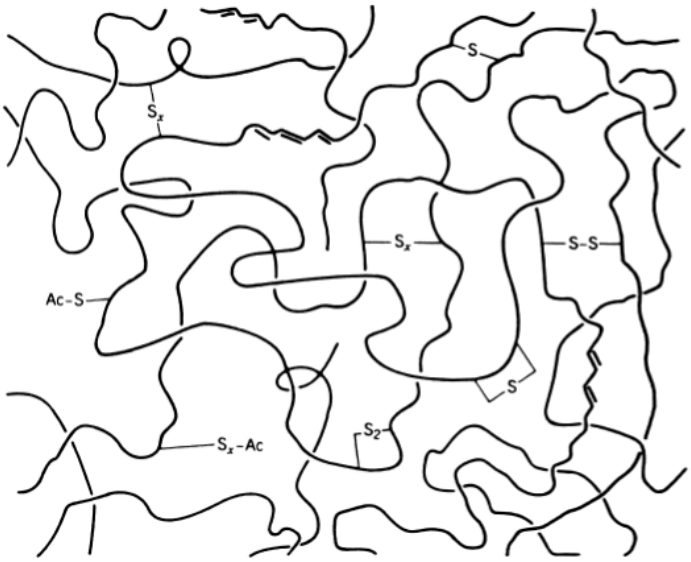

Figure 1.4. Schematic representation of crosslinked chains [4].

The rate and efficiency of the crosslinking process are increased by adding activators (e.g., zinc oxide and stearic acid) and organic-based accelerators (e.g., guianidines, thiazoles, xanthates) [5].

The crosslinking process can be monitored by analysing the torque-time curves, obtained from dynamic mechanical tests. A qualitative example of three possible results of such measurements is shown in Figure 1.5. After an initial decrease due to the heating of the sample, the torque increases because of the crosslinking onset; when the crosslinking is complete and a stable network is formed the torque remains constant, reaching a plateau. In certain cases, the torque may decrease due to the thermal instability of some crosslinks, causing the so-called reversion. In the presence of polysulphidic crosslinks, a slow increase in torque at long curing times can occur, which is referred to as creeping cure. This latter phenomenon is due to the breakdown and subsequent formation of crosslinks of lower sulphur rank, leading to an overall increase in the number of crosslinks [5].

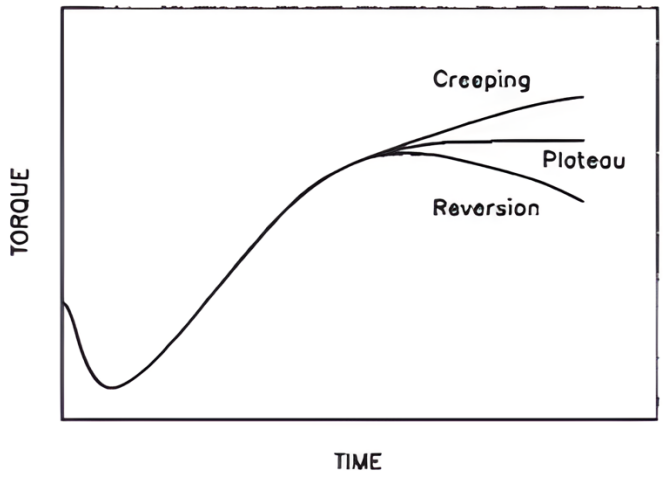

Figure 1.5. Qualitative representation of torque-time curves obtained from dynamical mechanical tests [5].

1.2.3. Filler reinforcement

Filler particles are added to the compound to reinforce the rubber matrix. The term reinforcement can refer to various aspects of the behaviour of the rubber; usually it is related to an increase in stiffness, modulus, tensile strength, tear strength, fatigue resistance, and abrasion resistance [6].

Along with carbon-black, silica is among the most widely used reinforcing fillers in the rubber industry. Silica, in particular, provides high tear strength, high modulus, and high fatigue resistance.

Silica consists of round particles with a diameter of about 10-100 nm. These particles join to form aggregates of irregular and branched shapes. The aggregates, in turn, can form bigger agglomerates thanks to polar forces. The agglomerates are broken down when the rubber is mixed with the filler and the other compound components; the aggregates, instead, cannot be broken down and are therefore considered the real reinforcing components. The strong interaction between silica particles is favoured by the presence of silanol groups ($Si-OH$), which lead to a polarity of the surface of silica.

Too strong interactions between filler particles are deleterious for the effective reinforcement of the rubber. In order to improve filler-rubber interactions, the surface of silica particles is modified using coupling agents. The coupling agent can be added

to the rubber compound during mixing (silanization treatment), or the silica can be pre-treated with the coupling agent before being added to the rubber compound (pre-silanization treatment).

During the silanization treatment, two chemical reactions occur: the first is the bonding between the coupling agent and the silica surface, while the second is the reaction of the coupling agent with the rubber matrix. The main disadvantage of this method is the generation of ethanol as a by-product of the silanization reaction, which causes a reduction in the mixing efficiency and favours the presence of porosity in the final compound [7]. The pre-silanization treatment overcomes these problems: in this case the production of ethanol as a by-product is avoided and the absence of the rubber matrix during the process allows higher yields of silanization [7].

The behaviour of the reinforced compound strongly depends on the dispersion of the filler. However, a total dispersion of filler particles in the rubber matrix is not desirable because it would lead to poor reinforcement [8]. The most effective reinforcement is achieved when a continuous filler network is formed inside the rubber matrix. Therefore, it is important for fillers to have the dual capacity of creating a network within the rubber while preventing the formation of large agglomerates that do not interact with the polymeric chains [8].

An important parameter for the rubber-filler interaction is the surface area of the filler particles, which is inversely proportional to the size: a large surface area leads to a higher interaction with the rubber matrix. The precise mechanisms by which this interaction influences the reinforcement process are not yet fully understood. In literature it is generally assumed the existence of a region near the surface of filler particles where the mobility of the rubber chains is strongly reduced. Consequently, in this area the rubber is stiffer than in the regions far away from the filler particles. More specifically, it has been verified [9] [10] the existence of three regions with varying degrees of mobility of the rubber chains: a region where the rubber is tightly bound to the filler particles, resulting in very limited mobility; a shell of rubber that interacts more loosely with the filler particles; and a portion of rubber that does not interact with the filler and has a mobility similar to that of pure rubber [8].

1.3. Dissipative behaviour of rubbers

Rubber compounds show a hysteretic behaviour, which is associated with the dissipation of energy during deformation. This phenomenon is evident while performing cyclic loading-unloading tests: the unloading curve, indeed, follows a lower path with respect to the loading one.

The input or strain energy (U_{tot}) and the elastically stored energy (U_e) can be obtained by integrating the loading and unloading curves, respectively. The dissipated strain energy (U_d) is given by the area between the loading and unloading path and can be computed as

$$U_d = U_{tot} - U_e \tag{1.9}$$

The dissipative response of the material depends on the material composition (nature of rubber and type of filler) and increases with the filler content, as shown in Figure 1.6 for NBR. Moreover, for each material, the energy dissipation increases as the applied strain increases. The primary cause of hysteresis is believed to be the disintegration and reaggregation of filler aggregates. Additionally, the interactions between the rubber and the filler are important in the dissipation mechanisms.

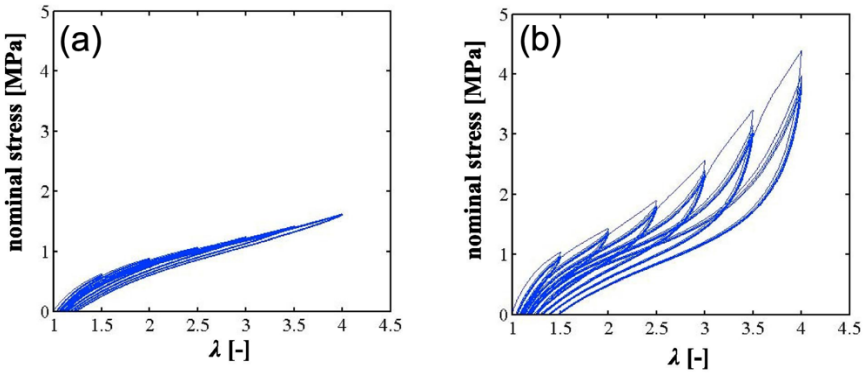

Figure 1.6. Mechanical response of NBR during cyclic uniaxial tests: (a) unfilled NBR; (b) NBR filled with 35 phr of carbon black[11].

1.4. Mullins effect

The phenomenon commonly known as “Mullins effect” was reported in literature for the first time by Bouasse and Carrière [12] in 1903 and later was thoroughly studied by Mullins, from whom it took its name.

The Mullins effect is experimentally observed by performing multi-cyclic loading-unloading tests: in the loading steps after the first cycle, lower stresses are observed for strains lower than the maximum strain applied in the first loading step. Figure 1.7 shows an example of the stress-strain curves obtained for a carbon black filled SBR from cyclic uniaxial tensile tests with increasing maximum strain every five cycles. From this example it is possible to highlight the main characteristics of the Mullins effect:

- most of the softening appears after the first cycle, and after a few cycles at the same level of strain a stabilization of the stress-strain response is observed
- the softening occurs at strains lower than the maximum strain ever applied to the material, while for higher strains the response goes back to the one of the pristine material
- the degree of softening increases with the increase of the maximum applied strain

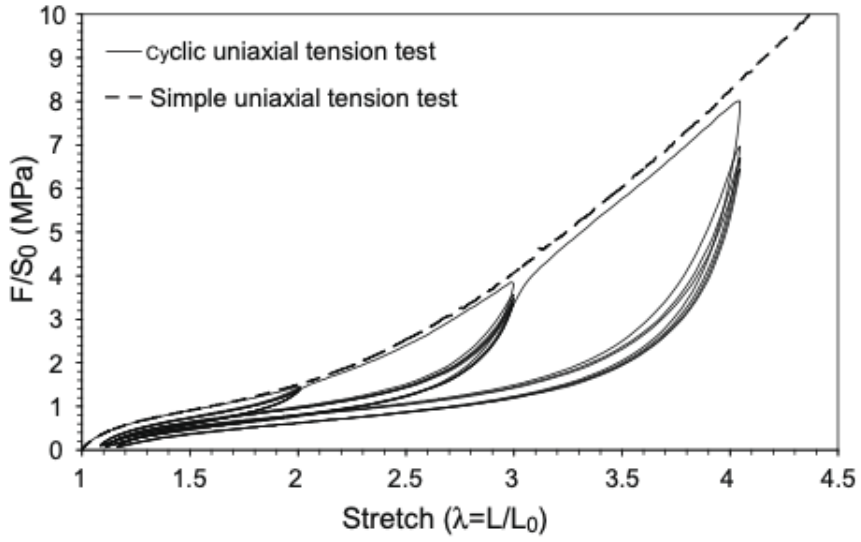

Figure 1.7. Stress-strain response of a 50 phr carbon-black filled SBR submitted to simple uniaxial tension and to cyclic uniaxial tension with increasing maximum strain every five cycles [13].

The pre-stretching leads to the presence of anisotropy in the material: indeed, the strain-induced softening has been observed to be more pronounced when the pre-stretched material is stretched again in the same direction of the pre-stretching, while its behaviour does not significantly change when it is stretched in the perpendicular direction [14][15].

The stress softening is strictly connected to the amount of the residual strain that is observed after a loading-unloading cycle. In particular, rubbers that exhibit the highest softening are the ones that also show the highest values of residual strain [16].

Although Mullins effect has been extensively studied in literature, an exhaustive understanding of its physical origin has not been achieved yet. One of the first attempts to find a physical explanation for the Mullins effect was developed by Mullins and Tobin [17]: since the rubber compounds are thought to be two-phase systems composed of regions of hard and soft rubber, they attributed the Mullins effect to the breakdown of hard regions during the first application of deformation, which would lead to an increase of the soft fraction of rubber. Other explanations found in literature can be grouped into the following categories:

- damage in the rubber matrix (e.g., chain scission [18], disentanglement [19], rearrangement of molecular network [20])
- modification of the filler network (e.g., filler aggregate or agglomerate fracture [21])
- change in the rubber-filler interface (e.g., molecule slipping [22] [23], bond breakage at the filler surface [24] [25])

1.4.1. Thermal recovery of Mullins effect

The changes in the material behaviour related to the Mullins effect are not permanent. In literature it has been reported that the behaviour of the pristine material can be recovered, at least partially, by swelling or by applying a proper thermal treatment. In some cases, the recovery is described as the recovery of the residual strain present after a loading-unloading cycle; in other cases, it is described as the recovery of the value of stress at a given level of strain or that of the entire stress-strain response of the material. The recovery of Mullins effect by means of a thermal treatment has been assessed for various combinations of rubber vulcanizates and fillers.

Mullins [14] and Laraba-Abbes et al. [26] studied the recovery of the stress-softening of natural rubber filled with carbon black. The former focused his attention on the stress needed to reach 200% of elongation after a pre-stretching at 320% strain and, as shown in Figure 1.8, observed that the recovery at a certain time increased by increasing the temperature at which the material was let recover after the preliminary stretching. The latter, instead, investigated the recovery of the entire stress-strain curve of specimens that were previously deformed to strains between 285% and 355%, and assessed a good recovery after a treatment at 95°C for 48 hours *in vacuo*.

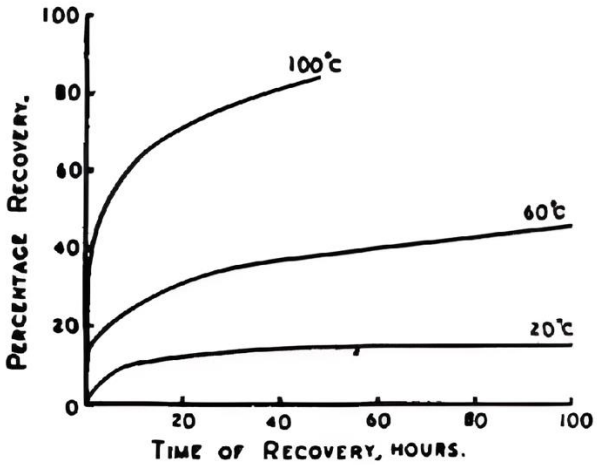

Figure 1.8. Percentage recovery of the stress needed to reach 200% elongation as a function of recovery time and thermal treatment temperature [14].

The degree of recovery is also influenced by the type of vulcanization. Harwood and Payne [20] studied the effect of the same thermal treatment (100°C for 24 hours *in vacuo*) on unfilled natural rubber with peroxide, monosulphide or polysulphide-based crosslinks. The specimens were pre-stretched at different strain levels (between 400% and 700% for peroxide-based compounds, and between 300% and 500% for sulphur-crosslinked rubbers). The compounds crosslinked with peroxide showed an almost complete recovery of the stress-strain curve, the ones that had polysulphidic crosslinks exhibited a very poor recovery, while the ones that contained monosulphidic crosslinks showed an intermediate behaviour. The lower amount of recovery observed in rubbers with polysulphidic crosslinks was attributed to the labile nature of the sulphur-sulphur link, which easily breaks under tension but can reform under stretching. This corresponds to a different spatial chain distribution, which results in a permanent residual deformation.

The effect of the type of crosslinking was studied also by Plagge and Klüppel [27], who focused on EPDM filled with carbon black. They performed 20 minutes long heat treatments at various temperatures on samples pre-stretched up to 200% strain. In the case of sulphur crosslinking, a good recovery was observed for $T > 110\,°C$; the compounds crosslinked with peroxide, instead, showed a poor recovery independently on the conditioning temperature. These results are in contrast with

what was observed by Harwood and Payne [20] and previously described; this leads to the conclusion that the recovery strongly depends on the type of rubber used, and it is difficult to find a general conclusion.

Plagge and Klüppel [27] also studied the effect of the filler type on the recovery of SBR, using the same experimental procedure adopted for EPDM: they observed that carbon black leads to a higher degree of recovery with respect to silica [27]. This result is confirmed by Diani et al. [13], who obtained the complete recovery of the stress-strain behaviour of a carbon black filled SBR pre-stretched to 200% strain and subjected to a heat treatment *in vacuo* at 80°C for 17 hours, as shown in Figure 1.9.

Finally, Li et al. [28] performed some experiments on NBR filled with carbon black, with the aim to assess the effect of filler volume fraction and of the duration of the thermal treatment at 80°C. The results show that, for materials pre-strained up to 300%, the recovery increases with an increase in the length of the thermal treatment and it decreases with an increase of carbon black content.

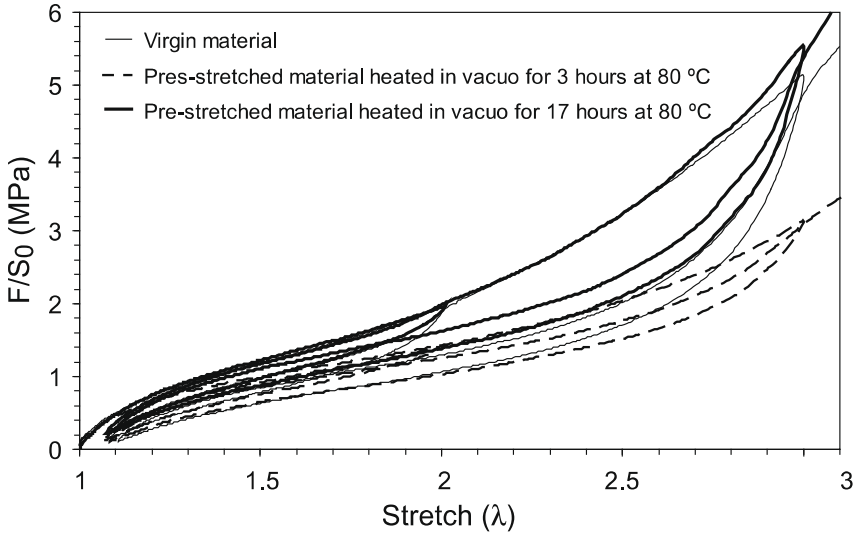

Figure 1.9. Stress-strain response of a 50 phr carbon-black filled SBR submitted to cyclic uniaxial tension in virgin state and in pre-stretched state after 3 and 17 h exposures to 80 °C [13].

The recovery of the Mullins effect by means of a thermal treatment depends on multiple factors, such as the time and temperature of the heat treatment, the crosslinking type of the compound, and the type of filler content. Table 1.1 shows a

summary of the experimental parameters used in literature to investigate the thermal recovery of the Mullins effect. It can be stated that it is not clear from literature how the temperature of the heat treatment should be chosen; indeed, it has not been found a correlation with neither the glass transition temperature nor the vulcanization temperature of different rubber compounds.

Table 1.1. Summary of the experimental parameters used in literature for the investigation of the thermal recovery of the Mullins effect.

Effects investigated	Paper	Material	Strain of pre-stretch	Thermal treatment
Time and temperature of thermal treatment	[14]	NR + CB	320%	20 – 100°C for 48 – 100 h
	[26]	NR + CB	285% - 355%	23°C for 3 months 95°C for 48 h
	[13]	SBR + CB	200%	80°C *in vacuo* for 3 and 17 h
	[27]	HNBR + CB	200%	23 – 170°C for 20 min
	[28]	NBR + CB	300%	80°C for 0.5 – 48 h
Crosslink type (sulphur and peroxide)	[20]	NR	300% - 700%	100°C *in vacuo* for 24 h
	[27]	EPDM + CB	200%	23 – 170°C for 20 min
Filler type	[27]	SBR + CB SBR + silica	200%	23 – 160°C for 20 min

1.5. Fracture of rubber

The fracture behaviour of rubbers is investigated using an energy-based criterion. This type of approach was first applied by Griffith [29] to brittle materials and is based on

the energy release rate, defined as the energy (U) dissipated during fracture per unit of newly created surface (A) at a fixed displacement l

$$G = -\left(\frac{\partial U}{\partial A}\right)_l \tag{1.10}$$

According to Griffith's criterion, fracture initiation occurs when the energy release rate exceeds a critical value G_c, which is an intrinsic characteristic of the material

$$G \geq G_c \tag{1.11}$$

In 1953 Rivlin and Thomas [30] extended Griffith's criterion to rubbers, introducing the tearing energy. Some years later, in 1968, Rice [31] introduced the J-integral and demonstrated that it is path independent in the case of linear and non-linear elastic materials; furthermore, he proved that the J-integral could be interpreted as the variation of elastic energy stored in the material per unit area of newly formed crack. As a result, for linear and non-linear elastic materials the J-integral is equal to the energy release rate defined in Equation 1.10, and a critical value (J_c) can be used to express the fracture toughness of non-linear elastic materials.

From the experimental point of view, the fracture behaviour of rubbers has been studied using several specimen geometries, some of which are shown in Figure 1.10. The most widely reported in literature is the notched pure-shear specimen, shown in Figure 1.11. When this specimen is loaded in mode I, which consists in applying a force in the direction perpendicular to the notch plane, it is possible to distinguish four regions, deformed in different ways:

- the region ahead of the notch tip (region A) is undeformed
- the central part of the specimen (region B) is in a state of pure shear stress
- the region that includes the notch tip (region C) is in a complicated state of stress
- the area near the force-free edge (region D) shows a deviation from the pure shear state of stress

During the propagation of the crack, region C shifts in the direction of crack growth, causing region A to grow at the expenses of region B.

In order to achieve a deformation close to pure shear in the centre of the specimen the ratio between the width (W) and the initial height (H_0) of the specimen should be $W/H_0 > 5$ [32]. Moreover, the initial notch length (a_0) should be $H_0/2 < a_0 < 0.6 \cdot W$.

The main reason of the extensive use of this type of specimen is that it allows for an easy calculation of the J-integral; this is possible using the single specimen method developed by Kim and Joe [33], who demonstrated that the J-integral at the fracture onset can be defined as

$$J_{onset} = \eta \frac{U_{onset}}{b(W - a_0)} \tag{1.12}$$

in which U_{onset} denotes the strain energy up to fracture initiation, b and W denote the thickness and the width of the specimen, respectively, and a_0 denotes the initial length of the notch. The parameter η is a dimensionless shape factor that can be considered unitary in the case of pure-shear specimens.

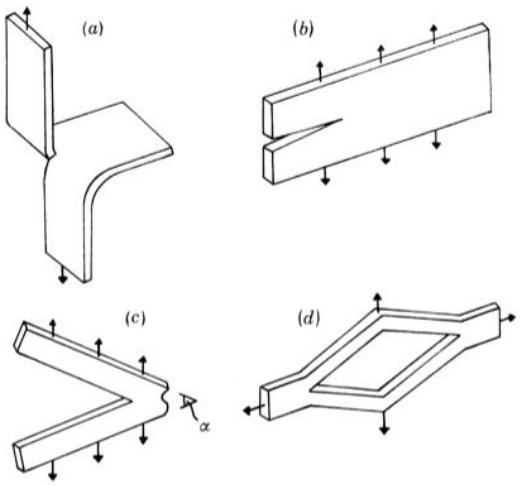

Figure 1.10. Specimen geometries used for the investigation of rubber fracture: (a) Trousers specimen; (b) pure shear specimen; (c) angled specimen; (d) split specimen [34].

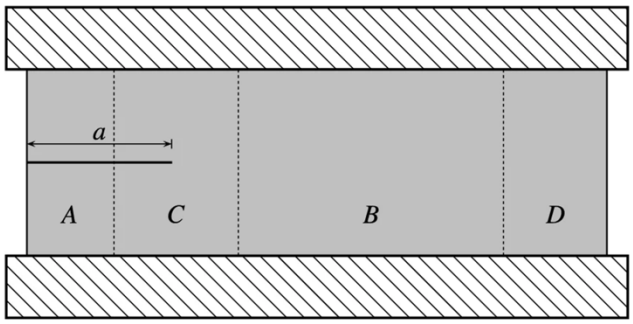

Figure 1.11. Pure shear specimen with a notch of length a [35].

When the load is applied to the specimen, the cut opens until a crack is initiated; after the fracture onset, the crack propagation continues only as long as the load is applied to the specimen. If the loading is stopped maintaining constant the applied elongation (i.e., no further energy is supplied to the material) the crack stops growing [30]. This stage is referred to as stable propagation. On the other hand, if the deformation of the specimen is continued, the crack propagation becomes unstable: the velocity of the crack suddenly becomes faster and does not cease even if the deformation is stopped [30]. Experimentally, the unstable propagation is identified in the force-displacement curve by a sudden drop of the force. In literature, however, there is no established standard procedure for determining the starting point of unstable propagation. Roucou et al. [36] considered the point at which a fast load drop occurs, as shown in Figure 1.12a. Elmukashfi [35], instead, considered the point at which the force first deviates from the monotonic increase trend, as shown in Figure 1.12b. Roucou et al. [36] also observed that unfilled SBR exhibits different type of crack surfaces during the two propagation stages. The stable propagation results in a rough surface, while the unstable propagation phase is characterized by a smooth surface.

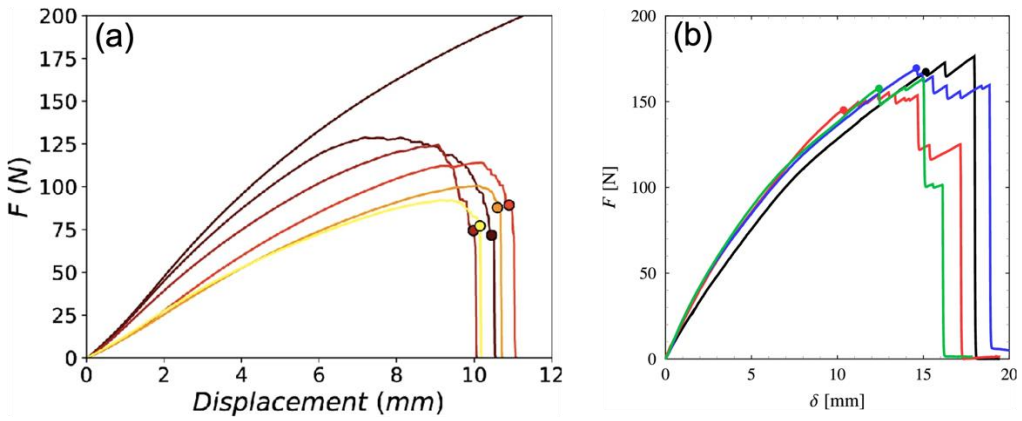

Figure 1.12. Definitions of unstable crack propagation starting point from literature: (a) in correspondence with the rapid force decrease [36]; (b) in correspondence with the force deviation from the monotonic increase [35].

1.6. Formation of cavities

Formation of cavities is one of the phenomena that can cause failure in rubber materials. Cavitation of the rubber matrix occurs when the rubber cannot contract

under a tensile load: as a result, the hydrostatic component of the tensile stress becomes more important causing the cavities to form and grow.

The first studies on cavitation were carried out by Gent and Lindley [37]. They approached the initiation of cavitation as an elastic instability of pre-existing defects of infinitesimally small dimension. In particular, they studied the problem of a spherical cavity of infinitesimal size present inside a rubber subjected to hydrostatic pressure. They assumed that the rubber remains an elastic solid for arbitrarily large deformations (i.e., the defect can grow only elastically) and developed the following relationship between the hydrostatic pressure (p) applied at infinity and the extension ratio (λ) at the surface of the cavity

$$p = \frac{E}{6}\left(5 - \frac{4}{\lambda} - \frac{1}{\lambda^2}\right) \tag{1.13}$$

in which E is the Young modulus of the rubber.

A limiting value can be obtained when λ goes to infinite, which means that the cavity becomes infinitely large

$$p_c = \frac{5}{6}E \tag{1.14}$$

They therefore assumed that cavitation occurs when the hydrostatic component of the stress approaches the value expressed by Equation 1.14.

They compared these theoretical findings with experimental results obtained from tests on poker-chip specimens of unfilled natural rubber, in which rubber disks are glued between two metallic cylinders and stretched along the thickness direction. This type of specimens allows to maximize the hydrostatic component of stress. By examining *post-mortem* specimens subjected to different levels of force, they observed that when the hydrostatic pressure was lower than p_c no cracks were present; above p_c, instead, a large number of cracks was detected. Further investigations performed on transparent specimens showed the formation of large voids, leading to the conclusion that the cracks observed at $p > p_c$ were due to cavitation.

Investigations on cavitation in presence of rigid spherical inclusions have also been performed (e.g., [38] [39]): rubber matrix cavitation was observed near the poles of the solid beads, and it was attributed to the highly triaxial stress present in those regions.

Even in this scenario, a strong correlation between the stress needed to initiate cavitation and the Young modulus of the rubber was established.

Lopez-Pamies et al. [40] developed a theory which extended Gent and Lindley's results to arbitrary loading conditions and random distributions of defects with different shapes: they confirmed that in the case of pure dilatational stresses their general criterion reduces to the one proposed by Gent and Lindley.

The works presented above relied on the idea that cavitation is essentially an elastic phenomenon. Another approach was taken in consideration by Williams and Schapery [41]. They studied the same infinitesimally small spherical cavity embedded in a rubber sphere but assumed that it could not only expand elastically but also by creation of new surfaces due to fracture. This extension was due to the observation that the strains at the cavity surface exceed the elastic limit of rubbers. Therefore, they proposed to consider the cavitation as a fracture phenomenon. The criterion that they proposed in the case of small cavities is the following

$$p_c = \frac{5}{6}E\left[1 - \frac{4}{5}\sqrt{\frac{E a_0}{6T}}\right] \tag{1.15}$$

in which E is the Young's modulus, T is the tearing energy, and a_0 is the initial radius of the cavity. It is interesting to notice that in the case of infinitesimally small cavities ($a_0 \sim 0$), the criterion reduces to the one proposed by Gent and Lindley and expressed in Equation 1.14.

More recently, Lefevre et al. [42] showed that the "elastic" theories developed by Gent and Lindley [37] and by Lopez-Pamies et al. [40] are in a good qualitative agreement with experiments, in the sense that they allow to easily determine where and when cavitation first occurs and how cavities continue growing and interacting once they have been "nucleated". From the quantitative point of view, the agreement is poor: this is mainly due to the fact that the material stops behaving as an elastic solid at large but finite deformations. Moreover, the rubber surrounding the defect at which cavitation occurs have different mechanical properties than the bulk rubber.

The theoretical studies and experiments presented above were carried out on unfilled rubbers. However, when dealing with filled rubbers, the issue becomes more

complicated due to the inherently heterogeneous structure of the material and the local confinement caused by the presence of nanofillers [43]. Moreover, in filled rubbers the cavitation of the rubber matrix is not the only phenomenon that can occur: debonding, which involves the failure of the rubber-filler interface, should also be considered. However, since it is experimentally challenging to distinguish between the cavities formed because of debonding and those formed because of cavitation, many studies present in literature discuss about cavitation as a whole, including both phenomena.

Gent and Park [39] carried out a study aimed at differentiating between cavitation and debonding. They considered a transparent silicone rubber and performed simple extension tests on rectangular strips containing a soda-lime glass inclusion with diameter of approximately 1 mm. In order to obtain strong and weak adhesion with the rubber matrix, the glass particles were treated with a primer and with a surfactant solution, respectively. Untreated glass beads were also considered. The results they obtained showed that:

- with strongly bonded inclusions, a small cavity formed near one pole of the inclusion in the direction of the applied load; as elongation progressed, the cavity grew in size coming into contact with the surface of the glass bead, and several other cavities formed at both poles
- with weakly bonded inclusions, the formation of cavities in the rubber near the poles of the bead was followed by an abrupt debonding
- with unbonded inclusions, debonding at one pole of the inclusion was first observed; at larger strains a smaller debonded region appeared at the other side of the inclusion

This study suggests that the interaction between the rubber and the filler particles has a significant impact in failure processes caused by the formation of cavities. This study, however, only examined a single inclusion of a much larger size than that of typical of filler particles, which are in the order of nanometers. Therefore, the situation in actual filled rubbers is likely to be even more complicated. The damaging process can be impacted by the non-uniformity of the rubber, which is, in turn, influenced by the formulation components and their distribution. Moreover, cavitation can be initiated by voids formed due to volatile substances or impurities [44].

In addition to mechanical tests, cavitation of rubbers has been studied with other complementary techniques, such as dilatometry [44] [45], X-ray microtomography [46] [47] and optical techniques [48] [49]. In this last case, rubber cavitation and matrix-filler debonding were correlated to a decreased transmittance of visible light [48].

2 Materials and methods

2.1. Material

The material studied in this thesis was supplied by Arlanxeo. It is an NBR with 18% acrylonitrile content and filled with 60 phr of pre-silanized silica. In particular, the employed silica is the Coupsil VP6508 grade produced by Evonik. The crosslinking is sulphur-based. The main components of the rubber compound are shown in Table 2.1. Other components include zinc oxide, stearic acid, antioxidants, and crosslinking accelerators.

Table 2.1. Main components of the studied rubber compound.

Component	Quantity [phr]
NBR	100
Silica	60
Sulphur	0.3

Crosslinking was obtained keeping the material at 170°C for 5 minutes, as suggested by Arlanxeo. A torque-time curve was provided by Arlanxeo and it is shown in Figure 2.1. It can be observed that at 170°C the material does not show signs of degradation for at least 30 minutes.

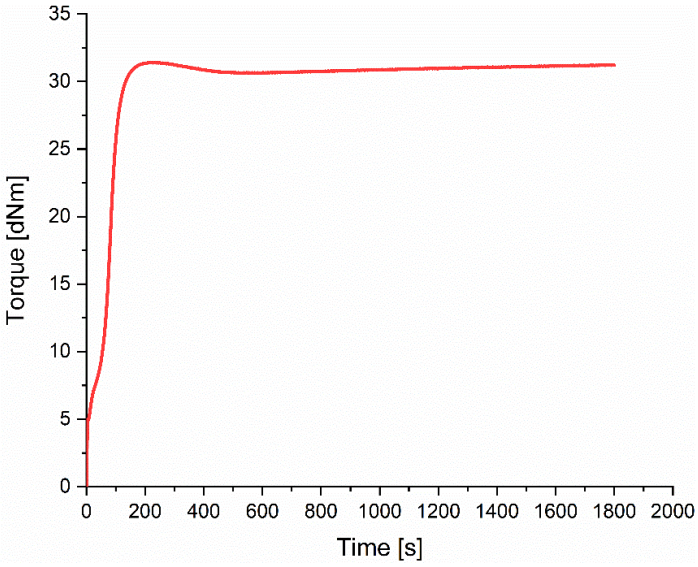

Figure 2.1. Torque-time curve for the NBR/silica compound supplied by Arlanxeo.

2.2. Preparation of specimens

Specimens for tests in uniaxial tension and pure shear conditions were prepared. In both cases the material was calendered at a temperature of 50°C to avoid any possible orientation of the polymeric chains. In the case of uniaxial tensile tests, square sheets with thickness of about 2 mm were obtained by compression moulding at 170°C at $P = 10\ MPa$. As suggested by the material supplier and referring to Figure 2.1, curing was carried out by keeping the material at 170°C for 5 minutes. Dumbbell specimens were then die-cut from the sheets. The geometry and the dimensions of the specimens comply with the specimen type 2 of the BS ISO 37:2017 standard [50] and are shown in Figure 2.2.

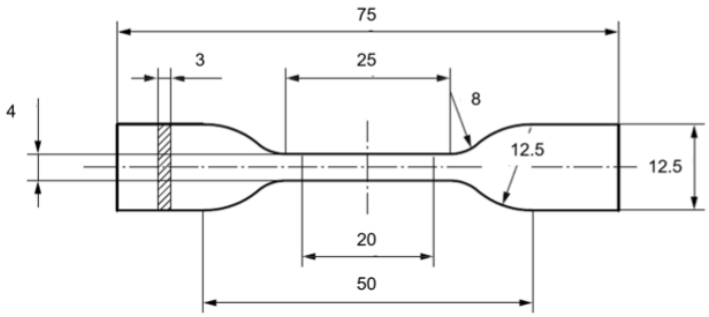

Figure 2.2. Geometry and dimensions of dumbbell specimens. Dimensions are in millimeters.

The specimens for tests in pure shear conditions were produced using home-made moulds. Curing was carried out by keeping the material at 170°C for 5 minutes. The geometry and dimensions of the pure shear specimen are shown in Figure 2.3, along with a schematic drawing of the clamping system.

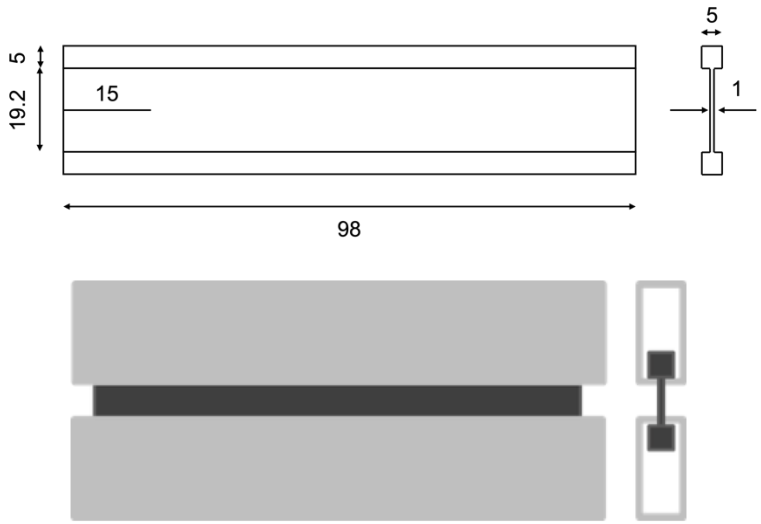

Figure 2.3. Geometry and dimensions (above) and aluminium clamping system (below) of pure shear specimens. Dimensions are in millimeters [51].

A post-curing treatment of further 5 minutes at 170°C, followed by a controlled cooling to room temperature at a rate of 1.5 °C/min, has been carried out in an oven (Figure 2.4b). The not post-cured and the post-cured material will be referred to as $NBR_{NO\ PC}$ and NBR, respectively.

One of the aims of this thesis work is to assess whether it is possible to recover the softening related to the Mullins effect by performing an appropriate thermal treatment on the softened material. As it will be described in Chapter 3, two different thermal treatments, referred to as TT1 and TT2, were adopted. TT1 consists in 23 minutes at 170°C, followed by a controlled cooling in oven at a rate of 1.5 °C/min. TT2, instead, consists in 105 minutes at 170°C followed by a cooling in open air.

The effect of these thermal treatments on both $NBR_{NO\ PC}$ and NBR was verified. Figure 2.4c and Figure 2.4d describe the whole thermal histories applied on the post-cured NBR, that will be referred to as NBR + TT1 and NBR + TT2.

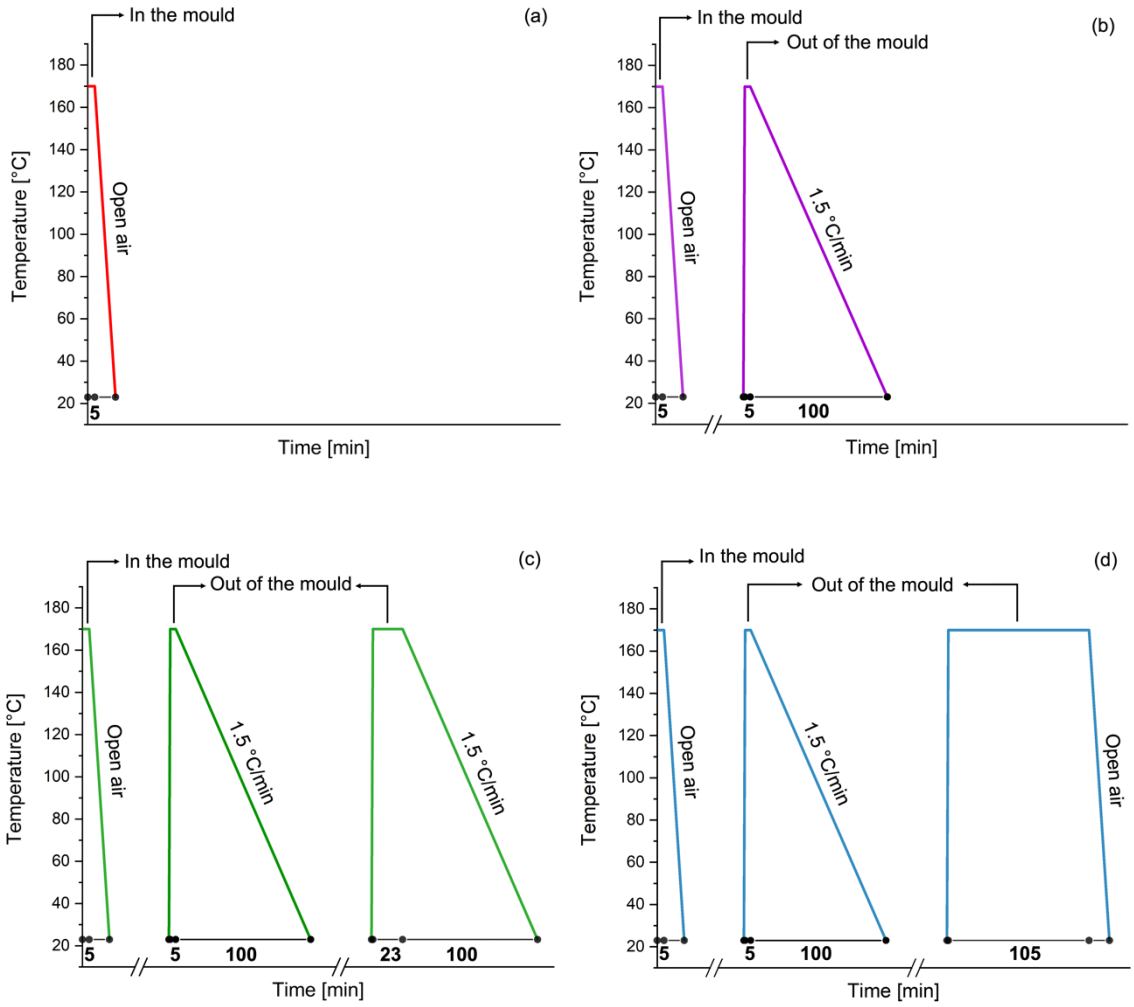

Figure 2.4. Thermal histories of the materials used in this thesis work: (a) $NBR_{NO\ PC}$; (b) NBR; (c) NBR + TT1; (d) NBR + TT2.

The reasons behind the choice of the parameters of the thermal treatments described above are the following:

- the temperature is equal to the temperature at which crosslinking was performed, to avoid any chemical reaction induced at a higher temperature
- the total time at a temperature higher than 50°C (50°C is the suggested calendering temperature and it is assumed that no crosslinking occurs below this temperature) is the same for the two thermal treatments
- the controlled cooling in the oven was introduced to exclude any possible effects due to the variety in the external conditions during cooling

- the rate of the controlled cooling in oven was the fastest possible using the oven at disposal

The mechanical tests were performed at least one hour after the end of the applied thermal history. A summary of all the materials that were used in this thesis is reported in Table 2.2.

Table 2.2. Summary of the materials and thermal treatments used in this thesis.

Material	Curing	Post-curing	TT1	TT2
NBR$_{NO\ PC}$	✓			
NBR$_{NO\ PC}$ + TT1	✓		✓	
NBR$_{NO\ PC}$ + TT2	✓			✓
NBR	✓	✓		
NBR + TT1	✓	✓	✓	
NBR + TT2	✓	✓		✓

2.3. Uniaxial tensile tests

Uniaxial tensile tests were carried out on an Instron 5967 dynamometer equipped with a 2 kN load cell and a pneumatic clamping system. Both monotonic and loading-unloading cyclic tests were carried out.

Tests were performed at room temperature (23°C) in displacement control at a displacement rate of 75 mm/min, which approximately corresponds to a nominal strain rate of 0.05 s^{-1}. The tests were video recorded using a 10 MPixel uEye UI 5490 SE camera with a framerate of 20 fps. The strains were evaluated from the videoframes using the video-extensometer method and are given by

$$\varepsilon = \frac{\Delta L}{L_0} \tag{2.1}$$

where ΔL is the relative distance between two lines previously drawn on the specimen at an initial distance L_0.

Monotonic uniaxial tensile tests were performed on all the materials reported in Table 2.2, with the aim to assess the effect of different thermal histories on the material response.

Cyclic loading-unloading tests were carried on the post-cured materials (NBR, NBR + TT1 and NBR + TT2) to investigate the softening related to the Mullins effect. Single cycle loading-unloading tests were performed on $NBR_{NO\ PC}$ and NBR + TT1 to evaluate the stored and dissipated energy.

2.4. Tests in pure shear loading condition

Tests in pure shear loading condition were performed at 23°C using an Instron 5967 dynamometer equipped with a 2 kN cell; home-made aluminium grips were used to fix the specimens. The displacement rate of the crosshead was set to 20 mm/min. The tests were video recorded using a 10 MPixel uEye UI 5490 SE camera with a framerate of 10 fps. The resolution of the images was below 0.0170 mm/pixel.

A black paint was sprayed on the surface of the specimens using an airbrush, in order to analyse the local displacements through Digital Image Correlation (DIC) and obtain the deformation field.

Pure shear specimens were used to carry out loading-unloading cycles and fracture tests.

2.4.1. Loading-unloading cyclic tests

Loading-unloading cyclic tests were carried out on un-notched specimens of $NBR_{NO\ PC}$ and NBR + TT1 to investigate the dissipative behaviour of the material.

The strains obtained from the Digital Image Correlation were compared with the ones obtained from the crosshead displacement using the following equation

$$\varepsilon = \frac{\Delta L}{L_0} \tag{2.2}$$

in which ΔL is the crosshead displacement and L_0 is the height of the specimen in the undeformed state.

The result of the comparison for a loading-unloading cycle up to 230% deformation is shown in Figure 2.5: since the two curves are almost identical, the strains in the case of cyclic tests were determined using the crosshead displacement and Equation 2.2.

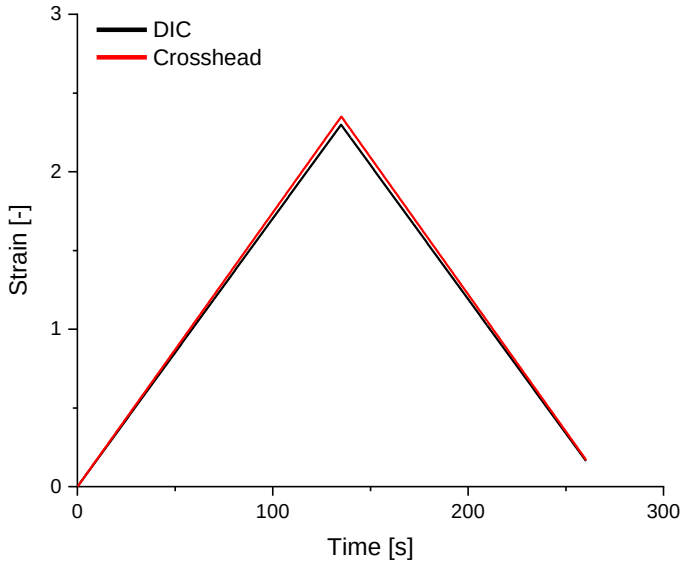

Figure 2.5. Comparison between the strain obtained from DIC analysis and from crosshead displacement for a single cycle test in pure shear configuration.

2.4.2. Fracture tests

In the case of fracture tests, a 15 mm long notch was cut at half height of one edge of the specimen using a razor blade and a plastic jig. In this case the strains were analysed through Digital Image Correlation using the software Vic-2D by Correlated Solutions.

Usually, the crack onset is determined from the videorecording of the test by identifying the point where the shape of the notch tip changes from blunt to sharp. However, in the case of the analysed material the identification of this transition was not straightforward.

For each specimen, the coordinate of the notch tip along the notch plane was tracked from the videorecording of the test and was plotted against the time. A linear fitting of the first 150–250 experimental points was performed; for each specimen the number of points considered was the one that maximised the fitting correlation coefficient (R^2).

In the same range of points, the average value and standard deviation of the difference between the experimental and fitting curves were computed.

The following quantities were determined:

- the time at which the difference between the experimental curve and the fitting line exceeds 3–4 pixels, depending on the resolution of the videorecording
- the time at which the difference between the experimental and fitting lines becomes bigger than the triple of the standard deviation

The crack onset time was then evaluated as the average of the values obtained following the two procedures described above. A validation of this method was done in the cases when it was possible to detect in the videorecording the transition of the notch tip from blunt to sharp.

The materials used for fracture tests were $NBR_{NO\ PC}$, NBR and NBR + TT1.

2.5. Swelling tests

The crosslink density was estimated through equilibrium swelling measurements in toluene. Due to the presence of the crosslinked network, the solvent is not able to dissolve the vulcanized rubber but it causes an isotropic expansion of the polymer network. The crosslinking degree can therefore be obtained through gravimetric measurements using the modified Flory-Rehner theory [52], according to which the crosslink density is given by

$$v_{swell} = \frac{-\ln(1-v_r) - v_r - \chi v_r^2}{V_0\left(v_r^{1/3} - \frac{2v_r}{f}\right)} \tag{2.3}$$

in which:

- V_0 is the molar volume of the solvent (in the case of toluene $V_0 = 106.3\ cm^3/mol$)
- χ is the rubber-solvent interaction parameter (in the case of NBR and toluene $\chi = 0.43$ [53])
- f is the functionality of the crosslinks (in the case of sulphur-based vulcanization $f = 4$)

- v_r is the volume fraction of rubber in the swollen system, given by

$$v_r = \left(1 + \frac{\rho_{comp} W_{swollen}}{\rho_s W_{dry}}\right)^{-1} \quad (2.4)$$

in which ρ_{comp} and ρ_s are the density of the rubber compound and of the solvent, respectively, $W_{swollen}$ is the weight of the swollen rubber, and W_{dry} is the weight of the dry rubber.

Small pieces of rubber were cut from compression moulded sheets and were immersed in toluene at 23°C for up to 96 hours. It was verified that after 48 hours swelling equilibrium was achieved, meaning that no more solvent could be absorbed by the rubber compound. Therefore, the swelling was performed for 48 h. The samples were then extracted from the toluene bath, dried with paper and left for 10 minutes under the hood to let the excess of solvent on the surface evaporate; they were then weighed, obtaining the term $W_{swollen}$ in Equation 2.4. In order to obtain W_{dry}, the swollen specimens were weighed after a drying step of 24 hours at 50°C into a vacuum oven. This treatment allows all the absorbed solvent to evaporate, along with eventual volatile substances and impurities that were present in the rubber and that were dissolved by the toluene

2.6. Digital Image Correlation analysis

Digital Image Correlation (DIC) is an optical technique that allows to obtain the full field of strains and displacements by processing the images of the specimen before and during deformation.

The analysis is carried out on a portion of specimen referred to as region of interest (ROI) and consists in a comparison process based on the sum-squared difference (SSD) correlation criteria. The information used to perform the correlation is the distribution of the grey scale intensity of the pixels of the image in the undeformed state, taken a s a reference, and the subsequent ones.

The grey value of one single pixel in the reference image cannot be univocally identified in a second image, as the same value can be found in many other pixels; for this reason, the correlation is performed considering small optically unique

neighbourhoods of pixels, called subsets, which can be univocally distinguished from the others. The spacing between the subsets takes the name of step and defines the measuring grid density.

In order to obtain unique and distinguishable subsets, a random speckle pattern is applied on the surface. The number of speckles that are deposited per unit area is important as it strongly influence the size of the subset that can be used; in particular, common guidelines [54] suggest to have 3x3 pixels in each speckle and at least 3x3 speckles in each subset. Pattern features that are smaller than 3 pixels may be aliased causing errors in the results; on the other hand, too large speckles will require larger subsets, which decrease the spatial resolution of the displacement and strain field. Moreover, to achieve an effective correlation the pattern must be isotropic, non-repetitive and characterized by high contrast. An example of three different speckle patterns is shown in Figure 2.6. Great attention must be put to the correct application of the pattern, in order to avoid the debonding or cracking of the pattern during deformation and minimize decorrelation problems during the analysis.

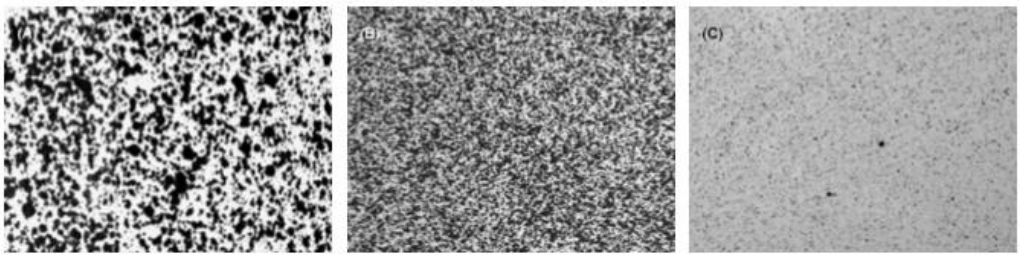

Figure 2.6. Patterns with different speckle size and density [55].

In tests that involve large deformations, as in the case of elastomers, the pattern may deform so much that the correlation with the reference undeformed image is lost. The solution to this problem is to perform an incremental correlation, in which the reference image is changed at every iteration of the analysis: in this case the displacement of the subsets at each time is determined with reference to the previous image and not using the undeformed image as a reference. The drawback of using this method is that it causes a progressive build-up of potential correlation errors.

The pattern may be applied using different techniques, such as stencils, airbrushes, or fine powders like a printer toner. In the case of the material studied in this thesis, the

best results were obtained by applying the pattern using an airbrush; since the material is translucid and has a yellowish/brownish colour, a black paint was used.

The software used to run the analysis was Vic-2D by Correlated Solutions. The employed subset dimension ranged between 33 and 43, depending on the testing conditions. The step was of 3 pixels for all the samples. It was decided not to use the incremental correlation because it provided very noisy results due to the accumulation of errors in the correlation. The levels of strains, in fact, are not so high to cause decorrelation with the undeformed image. The strain is calculated as a Green-Lagrange strain (ε_L), which can be converted to engineering strain using the following equation

$$\varepsilon = \sqrt{2\varepsilon_L + 1} - 1 \qquad (2.5)$$

3 Results and discussion

3.1. Characterization of the material

A preliminary characterization of the material was performed by means of uniaxial tensile tests and swelling measurements, with the goal to assess the effect of different thermal treatments on the behaviour of the material.

3.1.1. Monotonic uniaxial tensile tests

As already reported in Paragraph 2.2, two different thermal treatments were investigated: with TT1 the material is heated at 170°C for 23 minutes and then gradually cooled down to room temperature at a rate of 1.5 °C/min; with TT2 the material is heated at 170°C for 105 minutes and then let cool down to 23°C by leaving it in the open air. The thermal treatments were applied to both the not post-cured material ($NBR_{NO\ PC}$) and the post-cured material (NBR).

The nominal stress-strain curves obtained from uniaxial tensile tests performed on the not post-cured materials are shown in Figure 3.1. At least three specimens were tested for each case to assess the repeatability of the results. The results show that both thermal treatments have a stiffening effect on $NBR_{NO\ PC}$, probably due to a progression in the vulcanization process.

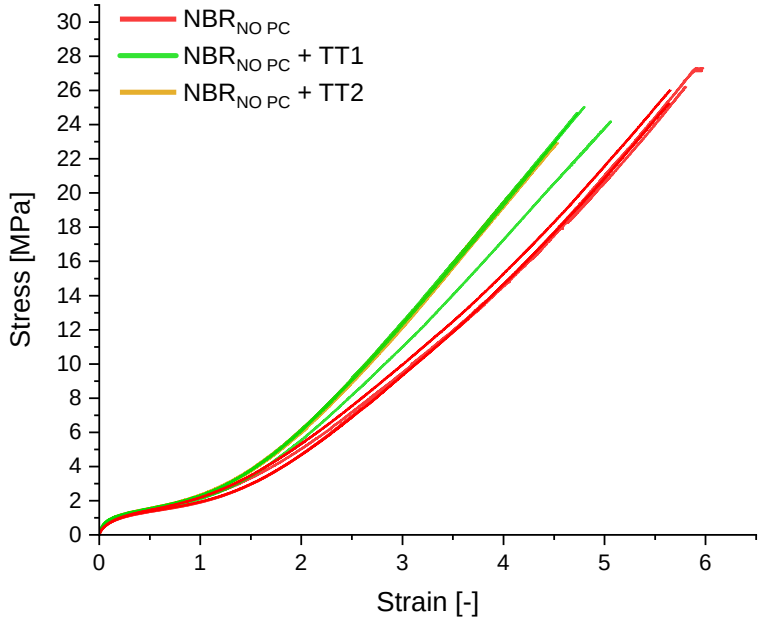

Figure 3.1. Stress-strain curves (T = 23 °C, $\dot{\varepsilon} = 0.05\ s^{-1}$) for $NBR_{NO\ PC}$, $NBR_{NO\ PC}$ + TT1 , $NBR_{NO\ PC}$ + TT2.

To better visualize the effect of the thermal treatments, the so-called Mooney-Rivlin plots, in which the reduced stress defined in Equation 1.8 is plotted as a function of $1/\lambda$, were used. The results are shown in Figure 3.2. The minimum of the curve is referred to as the reduced stress upturn point and is related to the maximum chain extension, which is in turn responsible of the stiffening effect observed at large strains in the stress-strain curves. At strain larger than the reduced stress upturn, dissipative deformation mechanisms take place (e.g., break of the extended chains or of physical crosslinks and chain recoil). The average values of reduced stress and strain at the upturn point for the three materials are summarized in Table 3.1. It can be observed that the reduced stress slightly increases with both thermal treatments, while a slight decrease in the strain is observed.

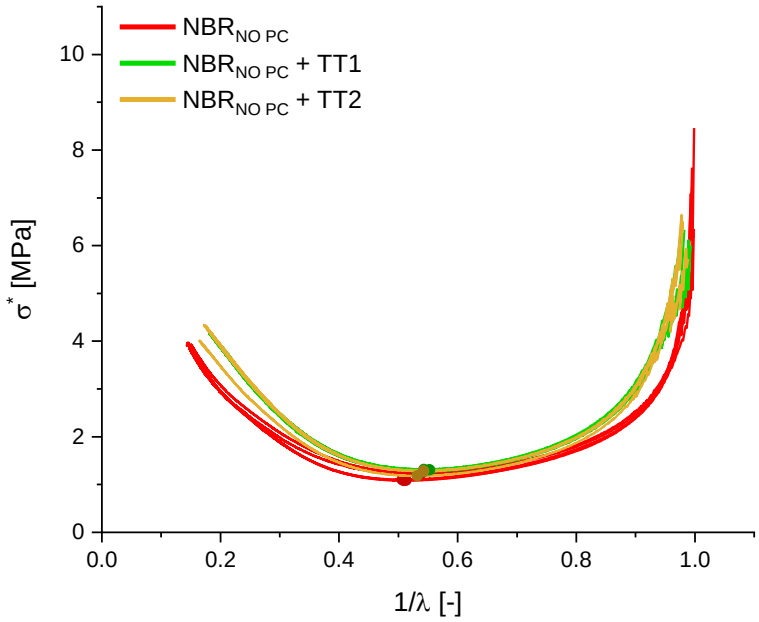

Figure 3.2. Mooney-Rivlin plots for $NBR_{NO\ PC}$, $NBR_{NO\ PC}$ + TT1 and $NBR_{NO\ PC}$ + TT2 with the indication of the reduced stress upturn point.

Table 3.1. Mean reduced stress and strain at upturn for $NBR_{NO\ PC}$, $NBR_{NO\ PC}$ + TT1 and $NBR_{NO\ PC}$ + TT2.

Material	Reduced stress at upturn [MPa]	Strain at upturn [-]
$NBR_{NO\ PC}$	1.15 ± 0.08	0.93 ± 0.05
$NBR_{NO\ PC}$ + TT1	1.25 ± 0.06	0.86 ± 0.02
$NBR_{NO\ PC}$ + TT2	1.30 ± 0.02	0.83 ± 0.02

Since the material behaviour, described by the stress-strain curve, changed as a result of the application of the thermal treatments, a post-curing treatment of 5 minutes at 170 °C followed by a controlled cooling in the oven at 1.5 °C/min was applied. The effect of the two thermal treatments on the post-cured material (NBR) was then assessed. The specimens tested were three for NBR and NBR + TT1, and two for NBR + TT2.

The results of the uniaxial tensile tests are shown in Figure 3.3 and Figure 3.4. It can be observed that TT1 has no significant effect on the stress-strain behaviour of the post-cured material; TT2, instead, causes a significant reduction in both the stress and strain at break. Apart from this aspect, the general trend of the stress-strain curve is not

affected by the two thermal treatments. No further significant change of the reduced stress and strain values at the upturn point, reported in Table 3.2, is observed: this suggests that the crosslinking process was most probably completed by post-curing.

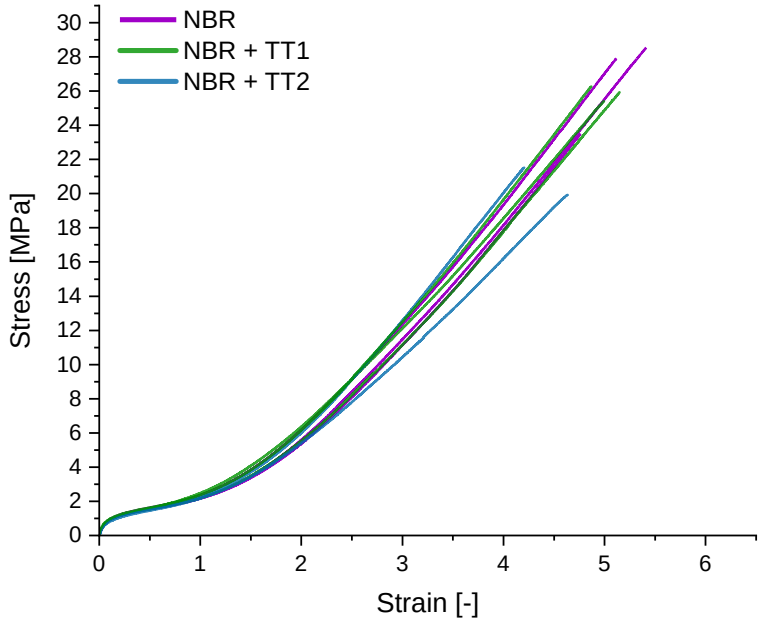

Figure 3.3. Stress-strain curves (T = 23 °C, $\dot{\varepsilon} = 0.05\ s^{-1}$) for NBR, NBR + TT1 and NBR + TT2.

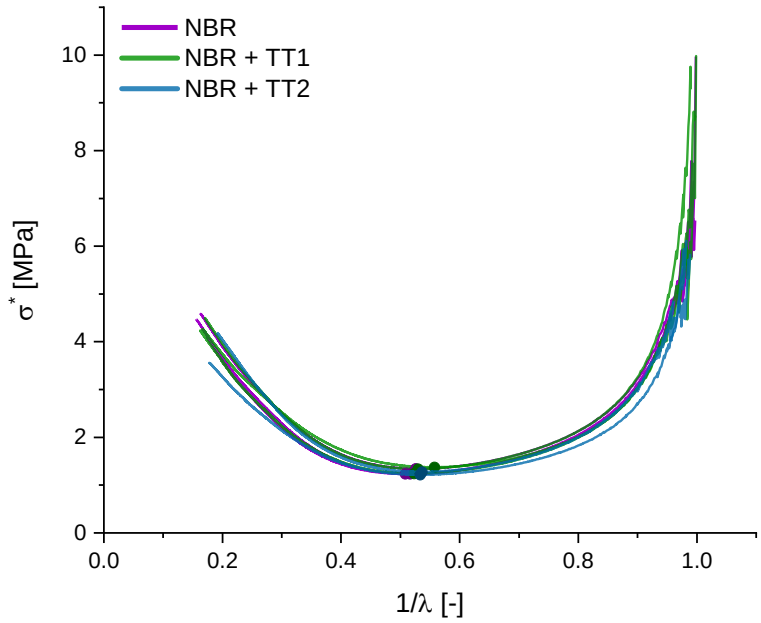

Figure 3.4. Mooney-Rivlin plots for NBR, NBR + TT1 and NBR + TT2 with the indication of the reduced stress upturn point.

Table 3.2. Mean reduced stress and strain at upturn point for NBR, NBR + TT1 and NBR + TT2.

Material	Reduced stress at upturn [MPa]	Strain at upturn [-]
NBR	1.27 ± 0.06	0.92 ± 0.03
NBR + TT1	1.31 ± 0.07	0.86 ± 0.06
NBR + TT2	1.24 ± 0.04	0.87 ± 0.01

3.1.2. Crosslink density

To evaluate the effect of the applied thermal history on the structure of the material, the crosslink density of $NBR_{NO\ PC}$, NBR and NBR + TT1 was evaluated using swelling measurements performed as described in Paragraph 2.5. These are the materials whose fracture behaviour was studied in detail, as it will be reported in Paragraph 3.5. The results are shown in Figure 3.5. It can be observed that the three materials show comparable values of crosslink density. This was expected in the case of NBR and NBR + TT1, as the stress-strain curves, shown in Figure 3.6, do not show a stiffening effect between the two. On the other hand, a lower crosslinking density was expected for $NBR_{NO\ PC}$ with respect to NBR and NBR + TT1, as lower stress values are measured at each strain for $NBR_{NO\ PC}$. This could be due to the fact that the swelling measurements do not detect only the chemical crosslinks but also the physical crosslinks that are related to the filler-rubber interactions.

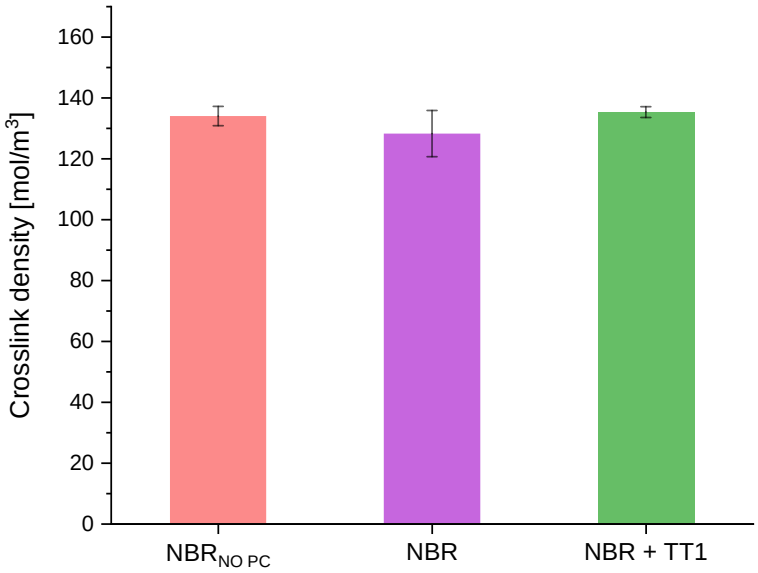

Figure 3.5. Crosslink density of $NBR_{NO\ PC}$, NBR and NBR + TT1.

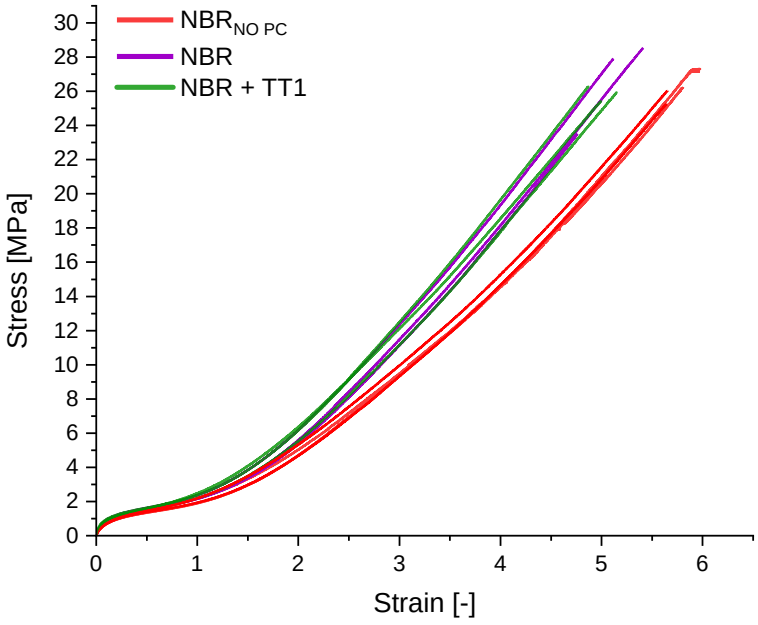

Figure 3.6. Stress-strain curves (T = 23 °C, $\dot{\varepsilon} = 0.05\ s^{-1}$) for $NBR_{NO\ PC}$, NBR and NBR + TT1.

3.2. Strain energy dissipation

Single cycle uniaxial tensile tests were performed to evaluate the energy that is stored and dissipated during the deformation of the material. The maximum strains that were reached ranged between 100% and 450%. The stress-strain curves are reported in Figure 3.7, while Figure 3.8 shows the stored (U_e) and dissipated (U_d) energy

components evaluated as the percentage with respect to the total strain energy and represented as a function of the maximum strain. It can be observed that at small strains the dissipated energy fraction is low, but it becomes larger than the stored one at strains higher than approximately 200%. Moreover, in the whole explored deformation range the material NBR + TT1 seems slightly more dissipative than $NBR_{NO\ PC}$. Further, by comparing the loading-unloading curves of the two materials for the same applied strain, it can be observed that the materials have a very similar elastic response, represented by the unloading curve: thus, the larger dissipation of NBR + TT1 has to be correlated to its larger strain energy due to a stiffer mechanical response.

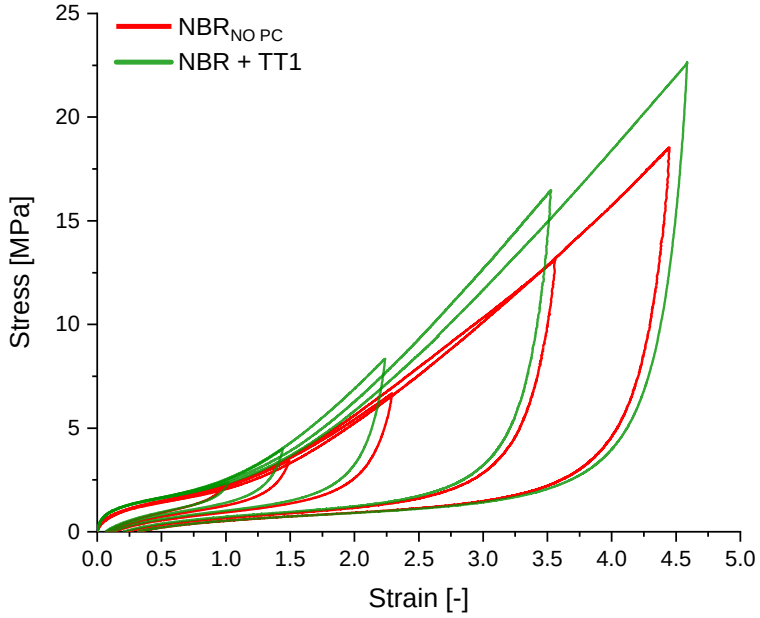

Figure 3.7. Stress-strain curves obtained from single cycle loading-unloading uniaxial tensile tests (T = 23 °C, $\dot{\varepsilon} = 0.05\ s^{-1}$) on $NBR_{NO\ PC}$ and NBR + TT1.

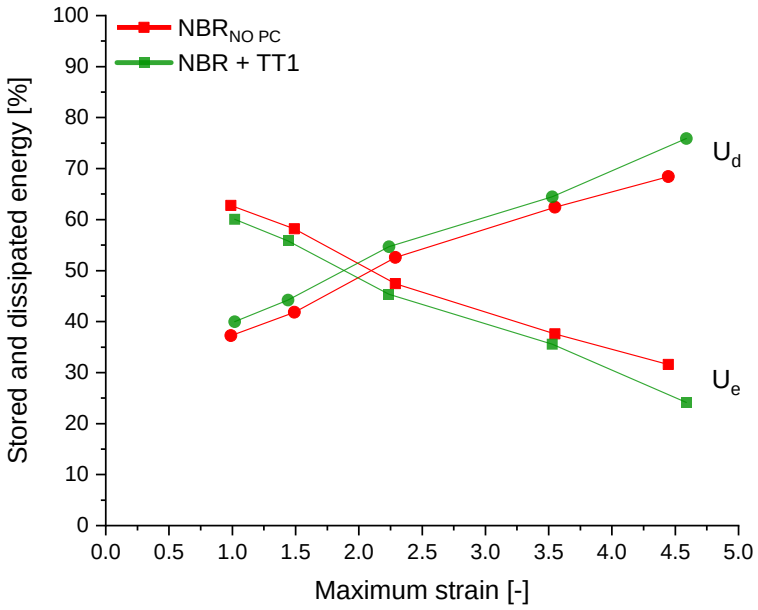

Figure 3.8. Elastically stored and dissipated energy components in uniaxial tension as a function of maximum strain for NBR$_{NO\ PC}$ and NBR + TT1.

The tests were repeated in pure shear loading conditions, using un-notched specimens. The maximum strains reached were 100%, 150% and 235%. At least two specimens for each level of strain were tested. For NBR$_{NO\ PC}$ at 235%, only one specimen was considered. Two other specimens were originally tested but showed a much softer behaviour that was not consistent with the curves obtained for lower strains; this behaviour was attributed to a defect in the production of the specimens and it was decided to exclude them from the results.

The stress-strain curves are shown in Figure 3.9, while the elastically stored (U_e) and dissipated (U_d) energy components as a function of the maximum strain are represented in Figure 3.10. It can be observed that the two materials exhibit a comparable dissipative behaviour in the whole range of explored strains. Moreover, the dissipated energy becomes higher than the elastically stored one for strains larger than 100%: this value is lower than that measured in uniaxial tensile tests.

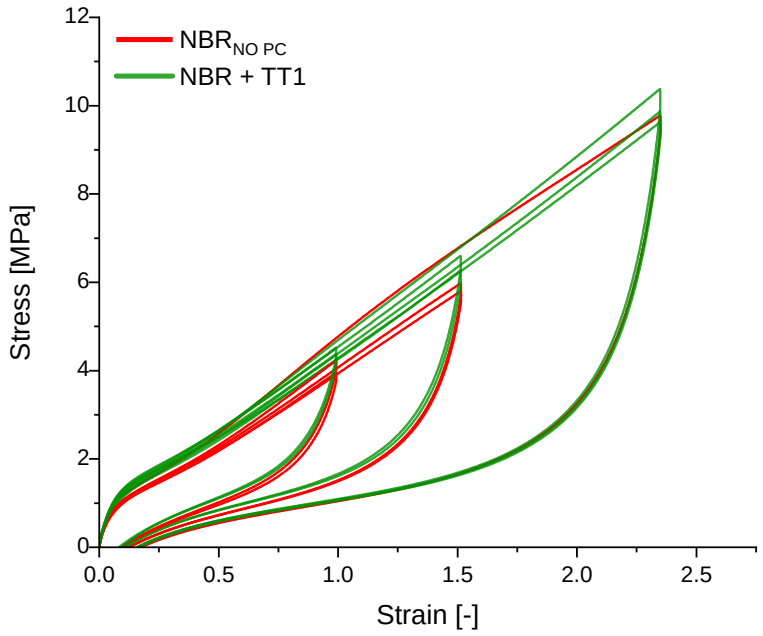

Figure 3.9. Stress-strain curves obtained from single cycle loading-unloading tests in pure shear loading conditions on NBR$_{NO\ PC}$ and NBR + TT1.

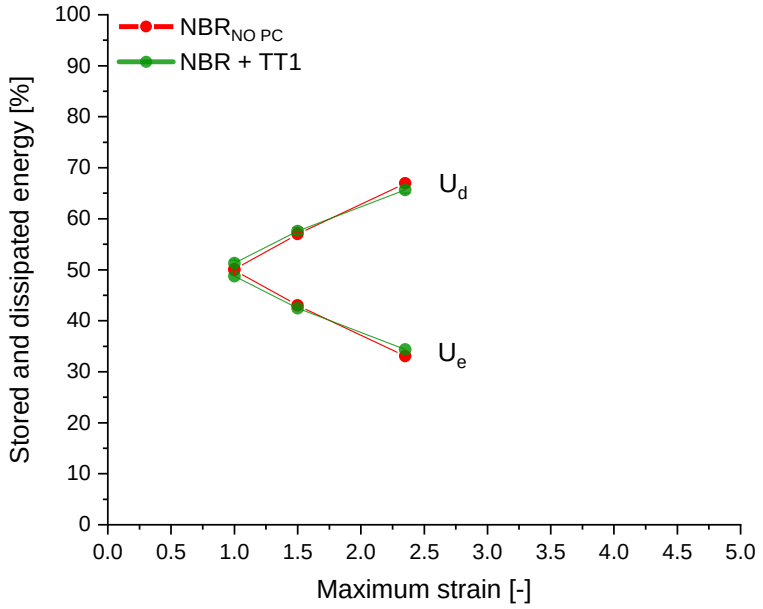

Figure 3.10. Elastically stored and dissipated energy components in pure shear configuration as a function of maximum strain for NBR$_{NO\ PC}$ and NBR + TT1.

Figure 3.11 shows the comparison between the dissipative components in uniaxial tension and pure shear loading conditions. It can be observed that both materials dissipate more in pure shear loading conditions than in uniaxial tension.

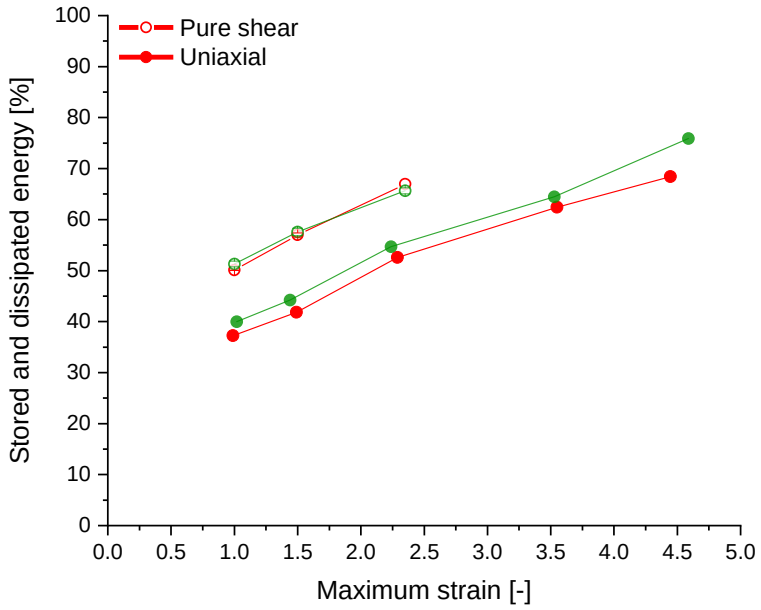

Figure 3.11. Dissipated energy component for tests in pure shear loading conditions and uniaxial tension on $NBR_{NO\ PC}$ and NBR + TT1.

3.3. Mullins effect

Cyclic uniaxial tests were performed in order to investigate the Mullins effect on the post-cured material (NBR). Ten loading-unloading cycles up to approximately 350% strain were applied to pristine NBR; the high number of cycles aimed to stabilize the stress softening effect. Four specimens were tested. The results are shown in Figure 3.12: for clarity, only one specimen and five cycles were reported. After the first cycle a stress softening is observed, as the loading curves of the first and second cycle do not coincide. Most of the softening occurs during the first cycle, and after a few cycles the behaviour of the material seems stabilized. This is confirmed by looking at the strain energy components, shown in Figure 3.13 and calculated as reported in Paragraph 1.3. It can also be observed that a strong reduction in the hysteresis, represented by the dissipated energy, occurs between the first and the second cycle, while the variation in the stored energy is much lower.

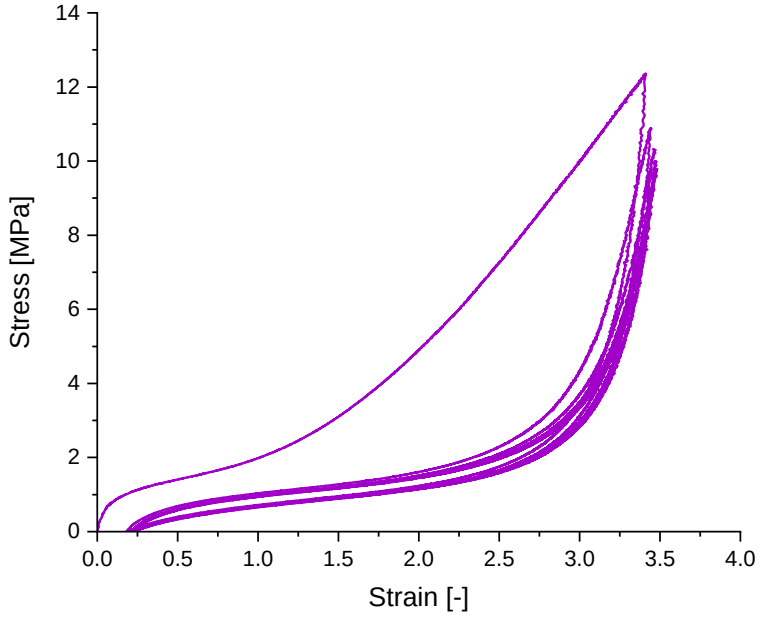

Figure 3.12. Cyclic uniaxial tensile stress-strain curve (T = 23 °C, $\dot{\varepsilon} = 0.05\ s^{-1}$) for NBR.

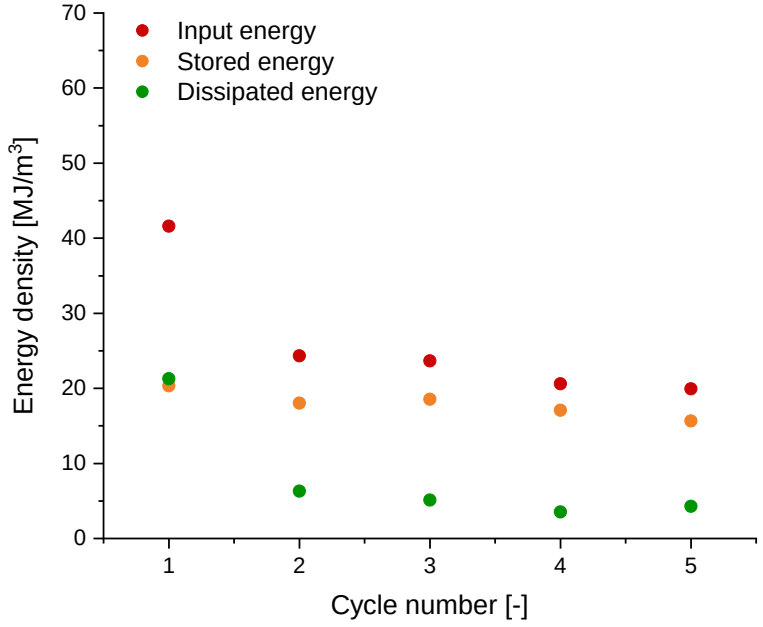

Figure 3.13. Input, stored and dissipated energy as a function of the number of deformation cycles for a specimen of NBR.

3.4. Thermal recovery of Mullins effect

After performing the multi-cycle loading-unloading test at 350% strain, specimens of the softened materials were treated using TT1 or TT2 thermal treatments. Then, the

specimens were tested again by applying two loading-unloading cycles. Two specimens were tested for each thermal treatment.

Figure 3.14. and Figure 3.15 show the results obtained using thermal treatments TT1 and TT2, respectively. For clarity, only one specimen and two loading-unloading cycles are reported. In the case of TT1, we observe a very good recovery of the stress-strain curve up to 100% strain and a good recovery up to 270% strain. For higher strains, a stiffer curve than that of the pristine NBR is obtained. In the case of TT2, a very good recovery of the stress-strain behaviour is obtained up to 200% strain. Again, for higher strains the softened and conditioned material is stiffer than the pristine one. This behaviour was observed also in literature (e.g., [13][26]) but it is still unclear why it occurs.

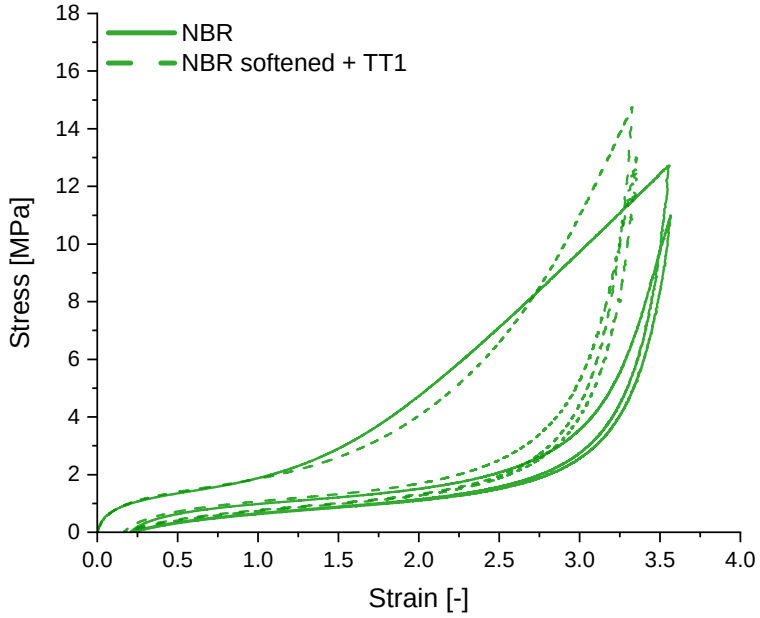

Figure 3.14. Stress-strain curves of two uniaxial tensile loading-unloading cycles for pristine NBR and NBR softened and thermally treated with TT1.

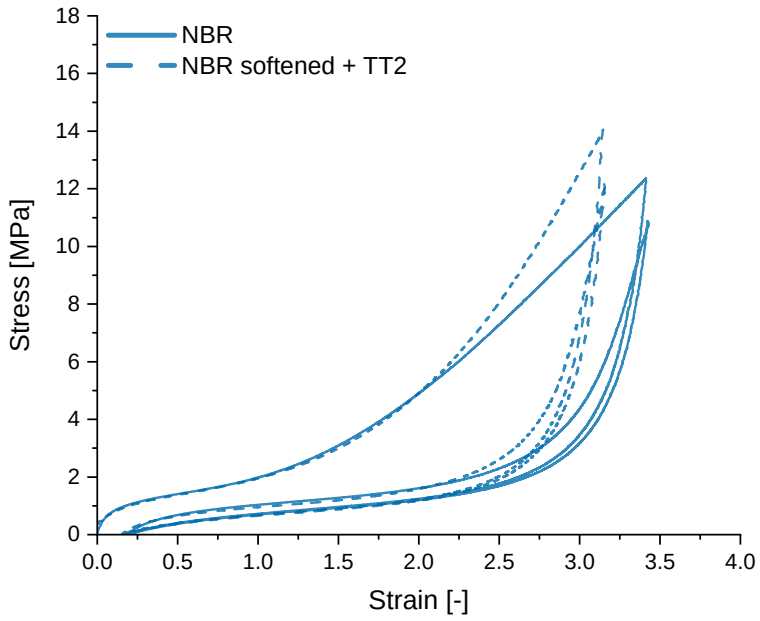

Figure 3.15. Stress-strain curves of two uniaxial tensile loading-unloading cycles for pristine NBR and NBR softened and thermally treated with TT2.

3.5. Fracture tests

Fracture tests were performed to assess the effect on NBR of the thermal treatment used to recover the strain-induced softening. Only TT1 was considered: this because, despite a lower recovery for strains between 100% and 200%, the stiffening effect present on the softened and conditioned material is observed at a higher strain (approximately 270% against 200% in the case of TT2). Moreover, uniaxial tensile tests showed that TT1 has a lower impact on the ultimate properties of the material. The behaviour of $NBR_{NO\ PC}$ was also assessed, in order to compare the effect of different thermal histories. At least five specimens for each material were tested.

It was observed that the crack always propagated along the initial notch plane, without evident deviations. In Figure 3.16 the force-time curves of $NBR_{NO\ PC}$, NBR and NBR + TT1 are shown. The final point of each curve corresponds to the propagation of the crack along the entire width of the specimen. The crack onset, represented by full dots, was determined as described in Paragraph 2.4.2. A stable crack propagation was initially observed, followed by an unstable and catastrophic propagation. As mentioned in Paragraph 1.5, literature does not report any standard procedure to identify the starting point of this unstable propagation. For the studied materials it can

be observed from Figure 3.16 that in some cases, after reaching the maximum value, the force stays almost constant for a while before quickly decreasing; in other cases, it immediately drops to zero. In this work it was decided to consider as the unstable propagation starting point the point at which the force reaches its maximum value, represented in Figure 3.16 by the star shaped points; indeed, the aim of this part of the research is to compare differently heat-treated materials, and the proposed methods seemed quite suitable because it allows to set a reference common to all the materials.

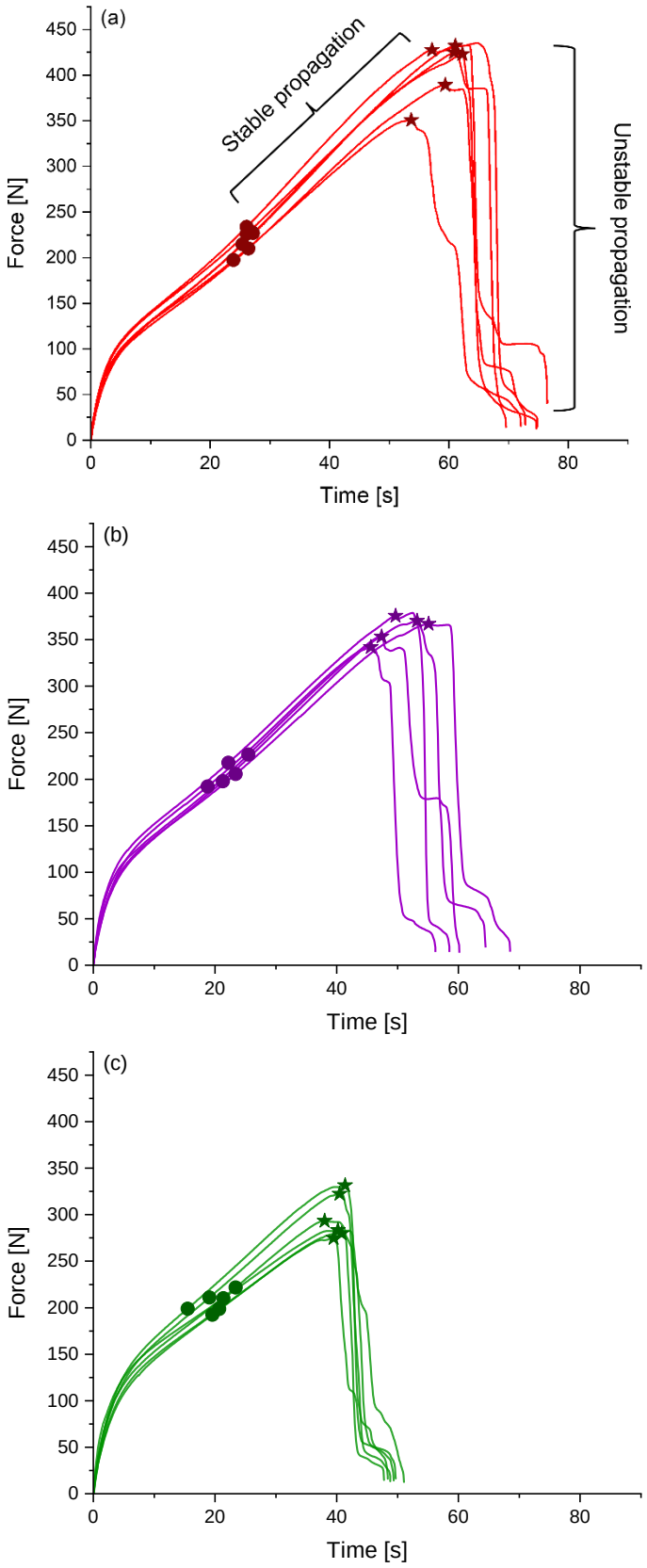

Figure 3.16. Force-time curves obtained from pure shear fracture tests: (a) $NBR_{NO\ PC}$; (b) NBR; (c) NBR + TT1.

Two tests were performed on NBR$_{NO\ PC}$ in order to verify the stability of crack propagation in different regions of the force-time curve. In the first case the loading was stopped at an intermediate point between the crack onset and the time at which the maximum force is reached. In the second case, the loading was stopped immediately after reaching the maximum force. By tracking the position of the notch tip from the videorecording of the test, the crack advancement (Δa) was measured and it was plotted as a function of time. The analysis of the videos showed a displacement of the notch tip even prior to the stable crack onset: this is caused by the lateral contraction of the specimen during deformation. In order to take this shrinkage into account, data were properly corrected: the displacement of the notch tip measured up to the stable crack onset was subtracted from the overall crack length. In this way, at the stable crack onset the crack advancement is equal to zero. It should be pointed out that this correction takes into account only the contraction that occurs on one edge before the stable crack onset; further contraction after the onset was neglected, since it was not possible to reliably estimate it.

The results are shown in Figure 3.17. It can be observed that when the loading is stopped at a loading time between the crack onset and that at which the force is maximum, the crack advancement reaches a plateau and there is no further propagation. Δa was tracked up to approximately 100 seconds but it was assessed that even after some minutes the crack did not propagate further. On the other hand, when the loading is stopped after reaching the maximum force, the crack continues propagating: it is observed that the crack propagation initially slows down and then accelerates again. Δa was tracked until the notch tip disappeared from the framing of the video but it was assessed that the crack spontaneously propagated along the whole width of the specimen.

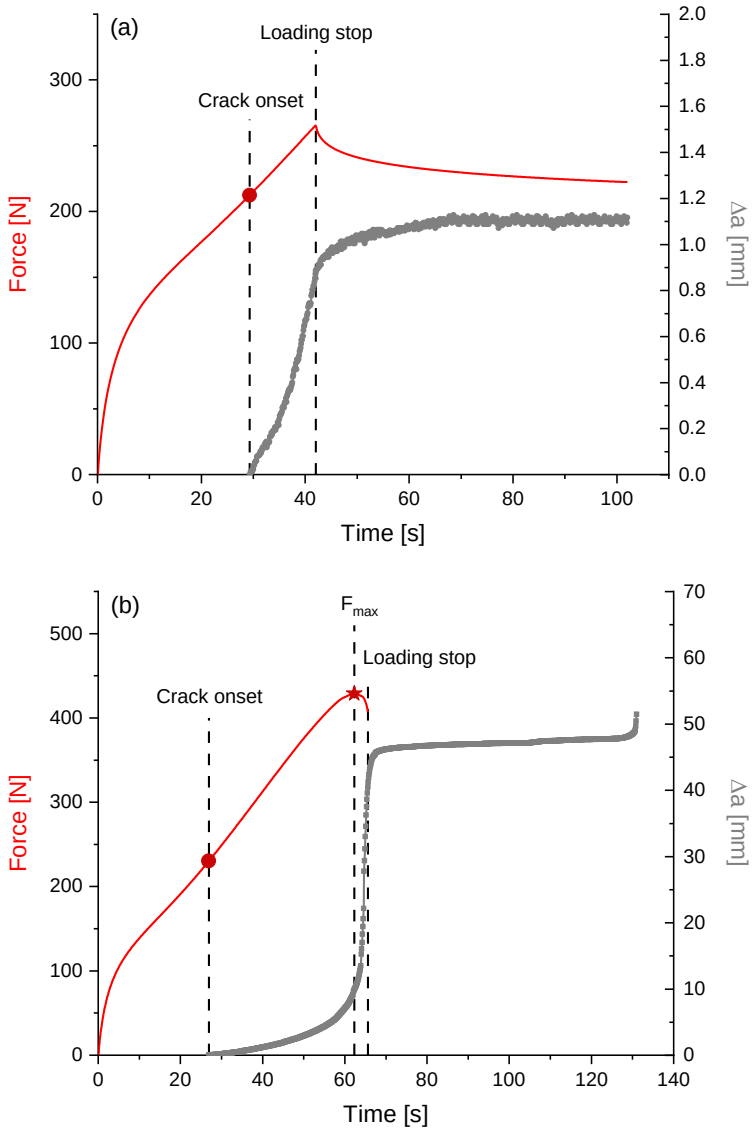

Figure 3.17. Force and crack advancement as a function of time for $NBR_{NO\ PC}$: (a) loading stop before reaching F_{max}; (b) loading stop immediately after F_{max}.

Comparing the curves represented in Figure 3.16 it can be observed that the maximum force is reached at progressively lower times when more severe thermal treatments are applied. This is an indication that NBR + TT1 shows the fastest crack propagation, while $NBR_{NO\ PC}$ shows the slowest crack propagation.

In order to take into account the geometry of the specimens, the J-integral applied up to the crack onset, calculated using Equation 1.12, is reported as a function of time in Figure 3.18. It can be observed that the material NBR + TT1 exhibits on average a slightly stiffer behaviour with respect to the other two.

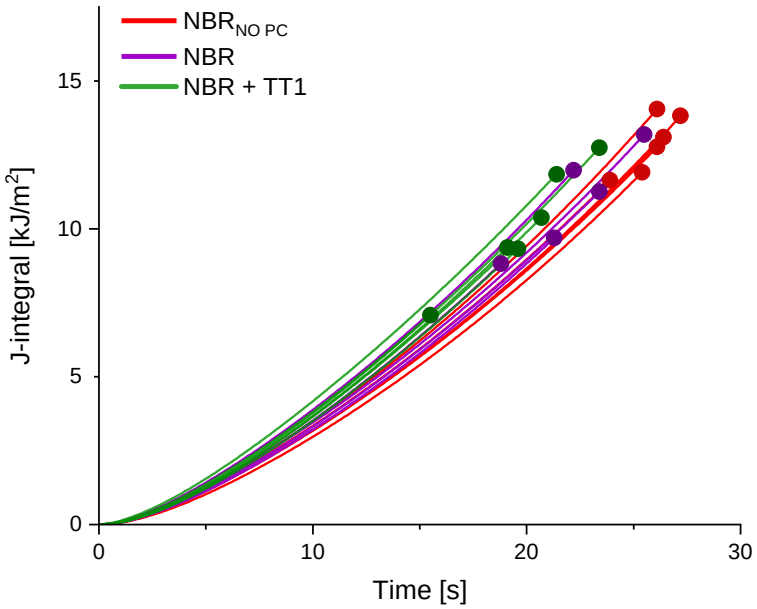

Figure 3.18. J-integral applied up to the crack onset as a function of time for NBR$_{NO\ PC}$, NBR and NBR + TT1.

3.5.1. Effect of thermal treatment on fracture onset

The fracture toughness of the three materials, expressed as the J-integral at the crack onset, is shown in Table 3.3 and Figure 3.19. A decrease in the fracture toughness between NBR$_{NO\ PC}$ and NBR is observed, while the fracture toughness of NBR is comparable to the one of NBR + TT1.

Table 3.3. J-integral at stable fracture onset for NBR$_{NO\ PC}$, NBR and NBR + TT1.

Material	J-integral at stable fracture onset [kJ/m²]
NBR$_{NO\ PC}$	12.88 ± 0.98
NBR	10.99 ± 1.75
NBR + TT1	10.12 ± 2.01

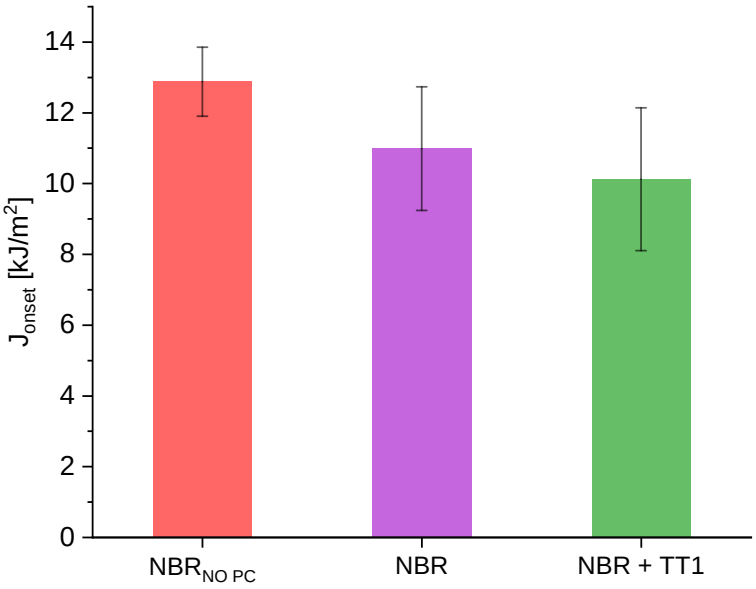

Figure 3.19. J-integral at crack onset for $NBR_{NO\ PC}$, NBR and NBR + TT1.

A statistical two-sample t-test with $\alpha = 0.05$ was performed in order to evaluate the statistical significance of the difference between the values obtained. This type of test returns the so-called p-value: if the p-value is higher than α it means that there is no significant difference between the mean values of the two populations. The results are summarized in Table 3.4. It is observed that the mean value of fracture toughness of NBR + TT1 can be considered statistically equal to the one of NBR, while it differs from the fracture toughness of $NBR_{NO\ PC}$. For what concerns the comparison between $NBR_{NO\ PC}$ and NBR, it resulted that the difference between their fracture toughness is not significant; however, the p-value is very close to the threshold value of $\alpha = 0.05$, therefore this result should be confirmed with further tests.

These results are in agreement with the uniaxial tensile tests, from which NBR resulted to have a stress-strain response similar to that of NBR + TT1, being stiffer than $NBR_{NO\ PC}$.

Table 3.4. Results of the statistical t-test performed on the J-integral at crack onset.

Materials compared	p-value	Result
$NBR_{NO\ PC}$ - NBR	0.07	No significant difference
NBR – NBR + TT1	0.47	No significant difference
$NBR_{NO\ PC}$ – NBR + TT1	0.02	Significant difference

Figure 3.20 shows the strains along the loading direction measured at the crack onset along the notch plane and plotted as a function of the distance from the notch tip. The strains were obtained thanks to Digital Image Correlation analysis. In the region in close proximity to the notch tip a whitening of the materials was observed: an example of a frame extracted from the videorecording of a fracture test on NBR + TT1 is shown in Figure 3.21. This made it impossible to achieve a reliable correlation in that region. It was assessed that the minimum distance at which reliable strains can be measured is 1.30 mm from the notch tip. The values of strain measured at the crack onset at such a distance from the notch tip are referred to as strain close to the notch tip (ε_{close}) and are represented in Figure 3.22. Figure 3.23, instead, shows the values of strain measured far from the notch tip (ε_{far}). It is observed that within the experimental dispersion the three materials show comparable values of ε_{close}. With regards to the strains far from the notch tip, a higher variability it is observed. A statistical t-test was performed to assess whether the mean values of ε_{far} can be considered comparable. The results are reported in Table 3.5 and show that the difference between the NBR$_{NO\ PC}$ and NBR is statistically significant, while NBR and NBR + TT1 can be considered statistically equal. It can also be observed that both ε_{close} and ε_{far} are smaller than 100%, which, as reported in Paragraph 3.2, is the threshold above which the dissipated energy component in pure shear loading condition is higher than the elastically stored one.

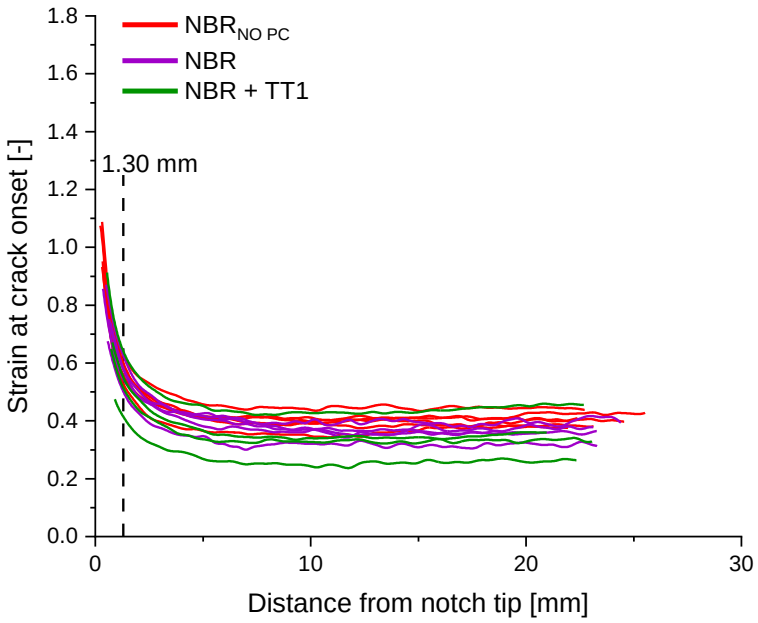

Figure 3.20. Strain distribution along the notch plane at crack onset. The dashed line indicates the distance from the notch tip at which ε_{close} was measured.

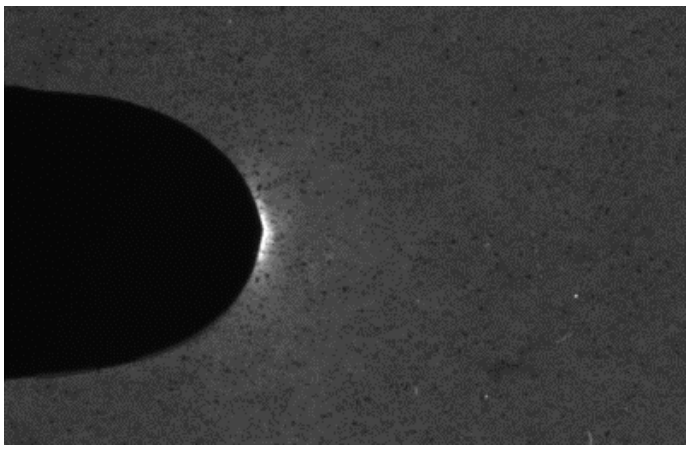

Figure 3.21. Whitening observed near the notch tip of NBR + TT1 during a fracture test.

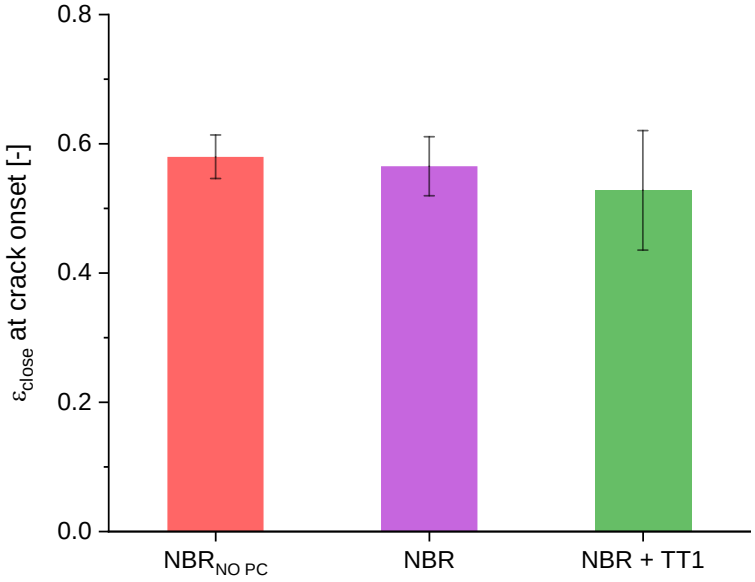

Figure 3.22. Strains at crack onset measured at a distance of 1.30 mm from the notch tip.

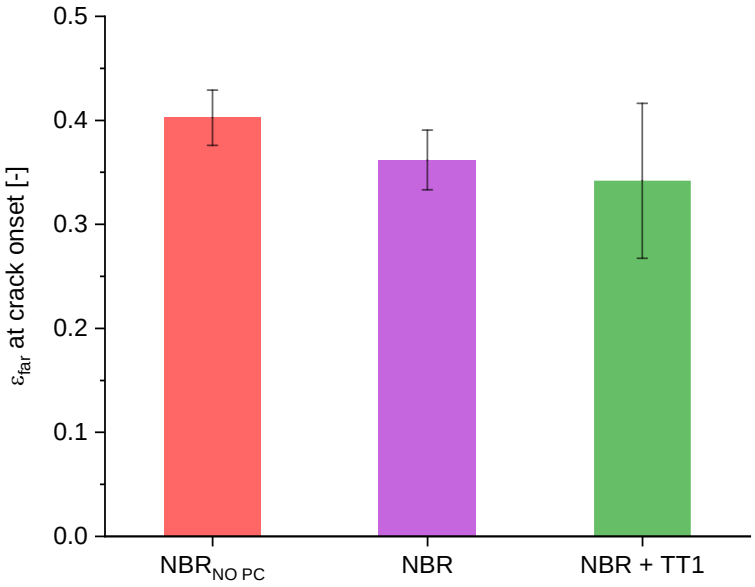

Figure 3.23. Strains at crack onset measured far from the notch tip.

Table 3.5. Results of the statistical t-test performed on the strains at crack onset far from the notch tip.

Materials compared	p-value	Result
$NBR_{NO\ PC}$ - NBR	0.04	Significant difference
NBR – NBR + TT1	0.64	No significant difference
$NBR_{NO\ PC}$ – NBR + TT1	0.20	No significant difference

3.5.2. Effect of thermal treatment on crack propagation

As reported in Paragraph 3.5, the fracture becomes unstable in correspondence with F_{max}, which is highlighted in Figure 3.24 for all the specimens analysed. The value of the applied J-integral in correspondence with F_{max} was calculated taking into account the propagation of the crack. Equation 1.12 therefore becomes

$$J(t) = \eta \frac{U(t)}{b[W - a(t)]} \tag{3.1}$$

The notch length $a(t)$ was obtained from the videorecording of the tests using the procedure reported in Paragraph 3.5

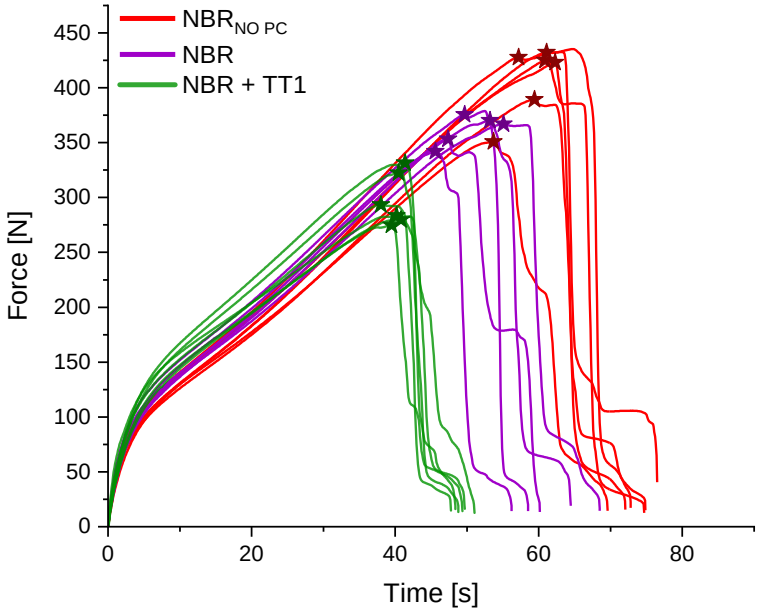

Figure 3.24. Force-time curve of $NBR_{NO\ PC}$, NBR and NBR + TT1 with the indication of the point of maximum force.

The values of J-integral at the maximum force are shown in Figure 3.25. It can be observed that both the post-curing treatment and TT1 cause a significant reduction in the J-integral at F_{max}.

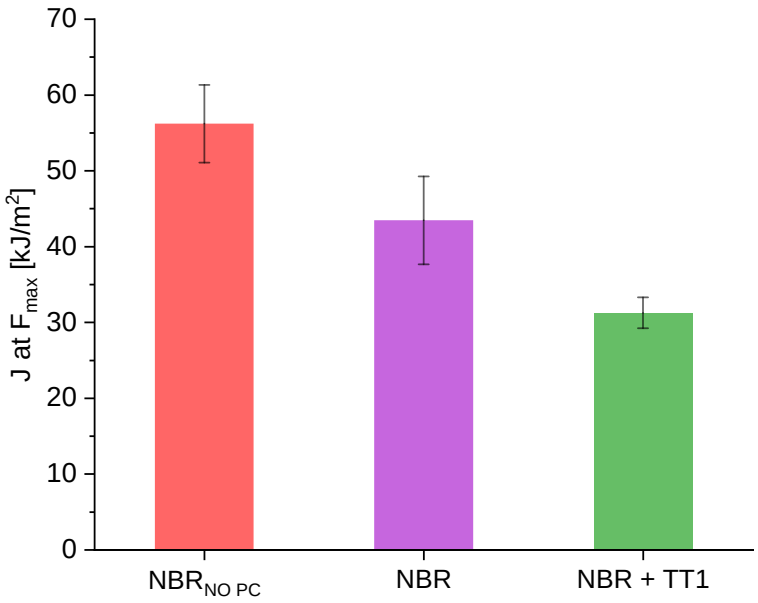

Figure 3.25. J-integral at F_{max} for $NBR_{NO\ PC}$, NBR and NBR + TT1.

In order to better highlight the effect of the thermal treatments on NBR fracture toughness, the relative change in the J-integral of NBR and NBR + TT1 with respect to $NBR_{NO\ PC}$ was computed both for its value at crack initiation and for that at F_{max}. The results are shown in Table 3.6 and Table 3.7: it can be observed that the thermal treatments have a more deleterious effect on the unstable fracture than on the onset of stable fracture.

Table 3.6. J-integral at crack onset and its relative variation with respect to $NBR_{NO\ PC}$.

Material	J_{onset} [kJ/m²]	Relative variation of J_{onset} compared to $NBR_{NO\ PC}$ [%]
$NBR_{NO\ PC}$	12.88 ± 0.98	-
NBR	10.99 ± 1.75	-14.7 ± 15.05
NBR + TT1	10.12 ± 2.01	-21.4 ± 16.74

Table 3.7. J-integral at F_{max} and its relative variation with respect to $NBR_{NO\ PC}$.

Material	J at F_{max} [kJ/m²]	Relative variation of J at F_{max} compared to $NBR_{NO\ PC}$ [%]
$NBR_{NO\ PC}$	56.21 ± 5.14	-
NBR	43.45 ± 5.80	-22.7 ± 12.51
NBR + TT1	31.24 ± 2.03	-44.4 ± 6.24

The strains along the loading direction measured along the notch plane in correspondence with the maximum force are shown in Figure 3.26 as a function of the distance from the notch tip. As in the case of the crack onset reported in Paragraph 3.5.1, the DIC software could not analyse the region very close to the notch tip. In this case, the minimum distance at which it was possible to obtain reliable DIC measurements was equal to 1.27 mm. Figure 3.27 shows the strains measured at such a distance from the notch tip (ε_{close}), while Figure 3.28 shows the strains measured far from the notch tip (ε_{far}). The application of progressively more severe thermal treatments causes a reduction in the strain both close and far from the notch tip.

Comparing these results with the characterization of the strain energy dissipation reported in Paragraph 3.2, it can be observed that for $NBR_{NO\ PC}$ the value of strain at F_{max} close to the notch tip is higher than 100%, which was the threshold above which the dissipated energy component in pure shear loading condition is higher than the stored one. In the case of NBR + TT1, instead, the strain at F_{max} close to the notch tip is smaller than 100%. For both materials, the strains at F_{max} close to the notch tip are smaller than the threshold value above which the dissipated energy component in uniaxial tension is higher than the stored one. If the strains measured far from the notch tip are considered, it can be observed that for both materials they are smaller than the threshold value above which the dissipated energy component is higher than the stored one, both in uniaxial tension and in pure shear configuration.

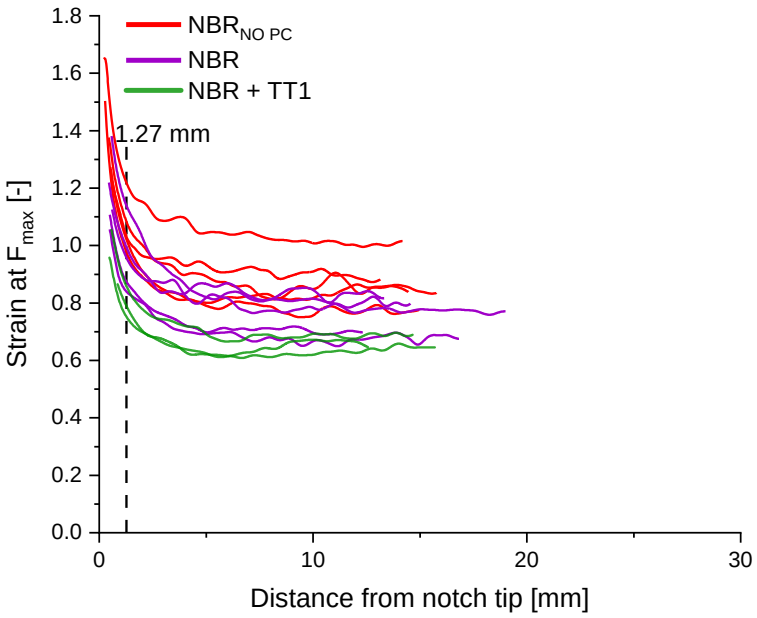

Figure 3.26. Strains along the notch plane at start of unstable fracture. The dashed line indicates a distance of 1.27 mm from the notch tip.

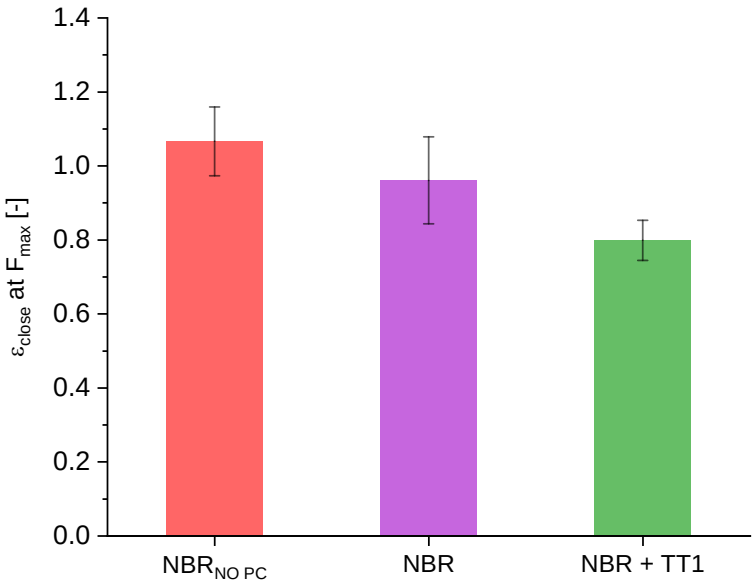

Figure 3.27. Strains at F_{max} measured at a distance of 1.27 mm from the notch tip.

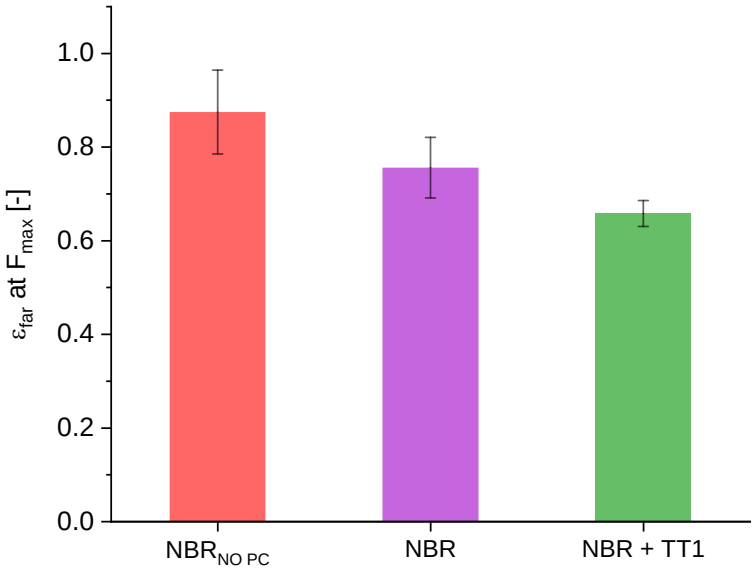

Figure 3.28. Strains at F_{max} measured far from the notch tip.

The J-integral at F_{max} ($J_{F_{max}}$) can be considered as the sum of an elastically stored (J_e) and dissipated (J_d) component

$$J_{F\max} = J_e + J_d \tag{3.2}$$

The two components can be computed using the components of the overall input energy evaluated in correspondence of the strain at F_{max} far from the onset. The values of the overall input energy were obtained from the cyclic tests in pure shear loading condition performed on NBR and NBR + TT1 and reported in Paragraph 3.2. As shown in Figure 3.9, those tests were performed in a strain range of 100–235%, which is higher than the strains at F_{max} measured far from the onset (0.87 for $NBR_{NO\ PC}$ and 0.66 for NBR + TT1). The values of the stored and dissipated energy components used to compute J_e and J_d were therefore obtained by fitting linearly the data shown in Figure 3.10. The results are reported in Table 3.8. It can be observed that $NBR_{NO\ PC}$ shows higher stored and dissipated J-integral components than NBR + TT1. This suggests that the thermal treatment causes a structural change in the material, which leads NBR + TT1 to dissipate less energy up to the unstable propagation starting point.

Table 3.8. Elastically stored and dissipated J-integral up to F_{max} for $NBR_{NO\ PC}$ and NBR + TT1.

Material	ε_{far} at F_{max} [-]	Dissipated energy at ε_{far} at F_{max} [-]	J_e [kJ/m²]	J_d [kJ/m²]
$NBR_{NO\ PC}$	0.87	0.488	28.78	27.43
NBR + TT1	0.66	0.481	16.23	15.02

3.6. Crack length and crack growth rate

Figure 3.29 shows the crack advancement (Δa) of the three materials as a function of time. It is assumed that before the crack onset the notch length is equal to the initial notch length and thus the crack advancement is equal to zero. For this reason, in Figure 3.29 the crack advancement is represented starting from the stable crack onset time. The crack advancement was measured until the notch tip disappeared from the framing of the video.

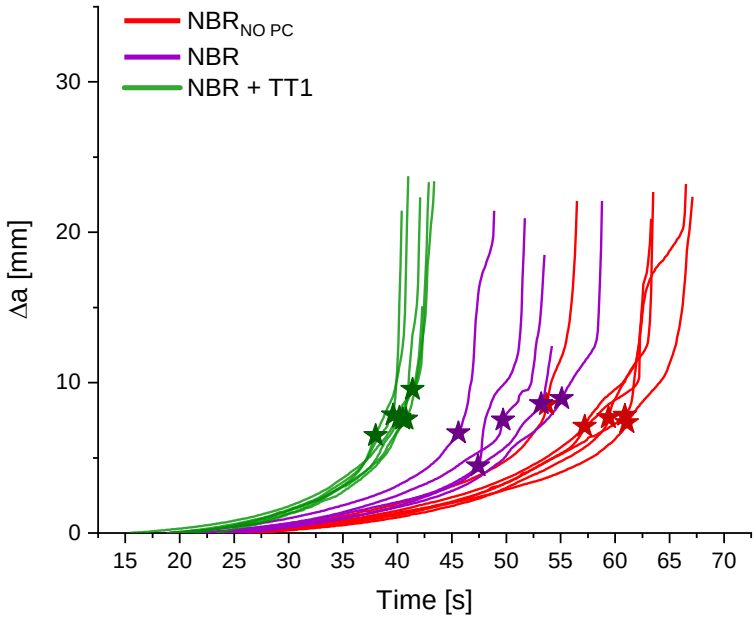

Figure 3.29. Crack advancement of $NBR_{NO\ PC}$, NBR and NBR + TT1 as a function of time with the indication of the starting point of unstable propagation.

The values of Δa corresponding to the beginning of unstable fracture propagation are shown in Figure 3.30 for the three materials. Within the experimental variability, it

seems that, irrespective of the material, the unstable fracture starts at a similar value of Δa, that thus results to be a critical value.

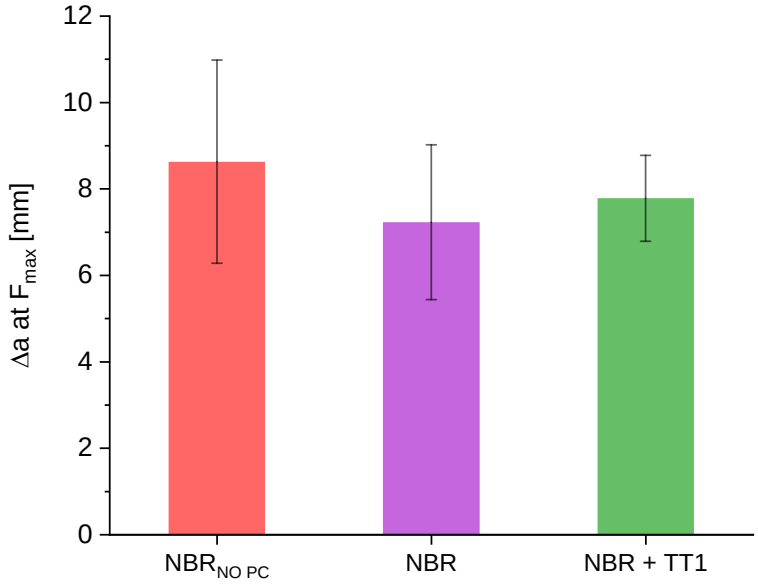

Figure 3.30. Crack advancement at the starting point of the unstable propagation for NBR$_{NO\ PC}$, NBR and NBR + TT1.

The applied J-integral after the crack onset, evaluated using Equation 3.1, is represented as a function of Δa in Figure 3.31. Because the fast crack propagation does not guarantee the synchronization between the data obtained from the videorecording and the data obtained from the dynamometer, no data relevant to the unstable propagation were reported. This type of curve is conceptually similar to the resistance curves used in fracture mechanics, in which the energy release rate is represented as a function of crack growth. It can be observed that the application of progressively more severe thermal treatments causes a reduction in the resistance to crack advancement.

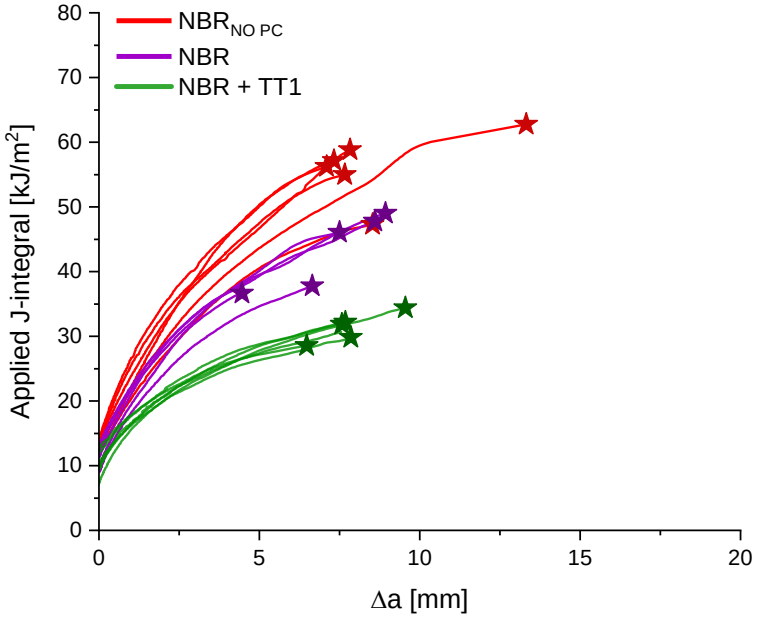

Figure 3.31. Applied J-integral after the crack onset as a function of Δa for NBR$_{NO\ PC}$, NBR and NBR + TT1.

For a deeper analysis, the crack growth rate ($\dot{a}$) was computed through numerical differentiation of the crack length; the results for the three materials are shown in Figure 3.32, where the values of $\dot{a}$ at the time at which the maximum force is reached ($\dot{a}_{F_{max}}$) are indicated by star shaped points.

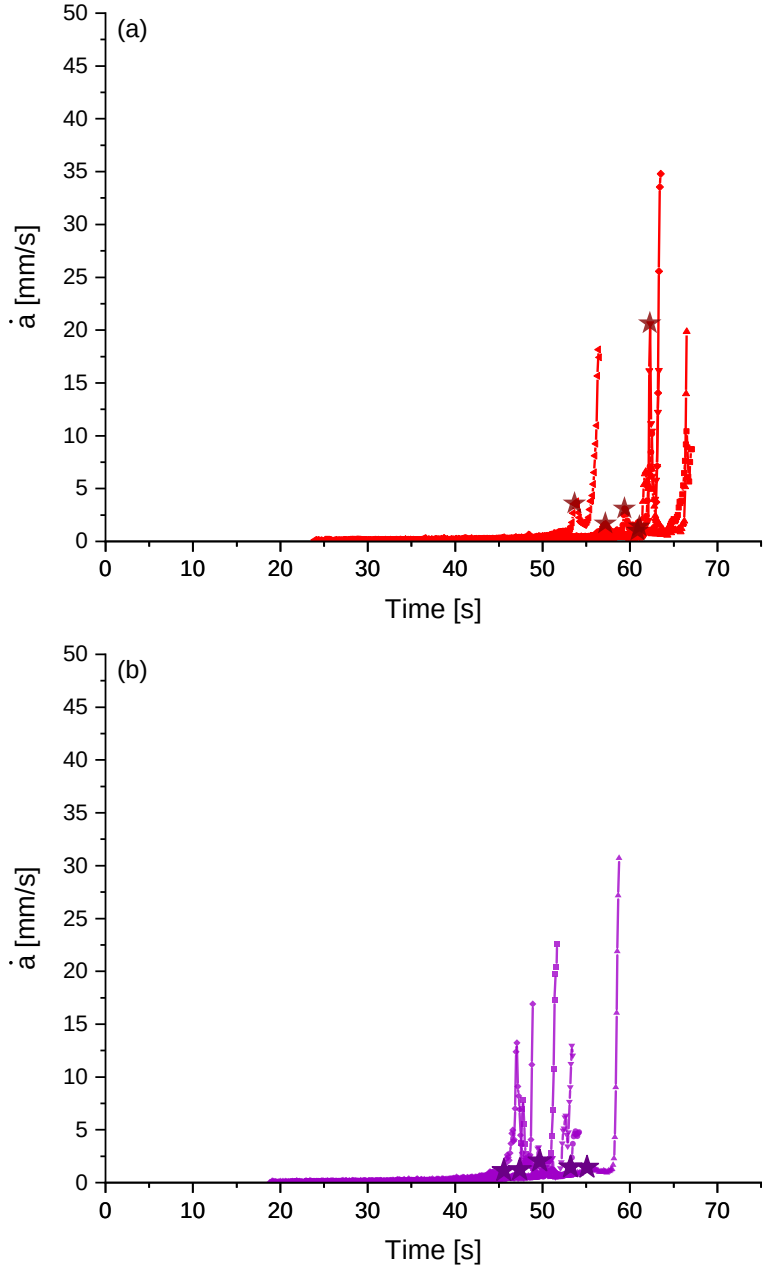
(a)
ȧ [mm/s]
Time [s]
(b)
ȧ [mm/s]
Time [s]

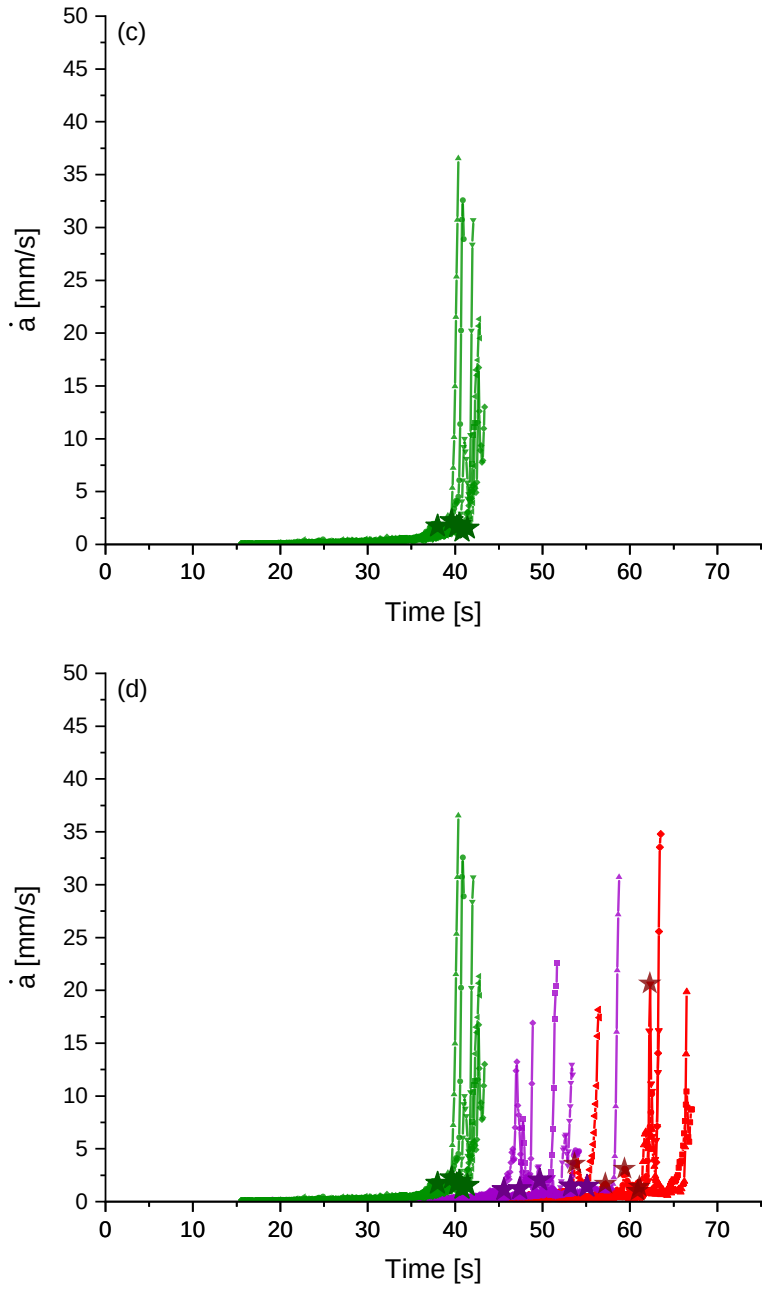

Figure 3.32. Crack growth rate with the indication of the starting point of unstable propagation: (a) $NBR_{NO\ PC}$, (b) NBR, (c) NBR + TT1, (d) comparison between the three materials.

It can be observed that the crack does not propagate at constant velocity but there are some acceleration and deceleration phases which lead to the presence of peaks in the $\dot{a} - t$ curve. These peaks correspond to a deviation of the force from the increasing monotonic trend observed in the force-time curves in Figure 3.24. If F_{max} is measured at the beginning of this deviation, $\dot{a}_{F_{max}}$ is located on a relative maximum of $\dot{a}$, and

the plateau of the force corresponds to a deceleration of the crack. If, on the other hand, F_{max} is measured shortly before the drop of the force, the crack propagation is accelerating. Nevertheless, in these cases $\dot{a}_{F_{max}}$ is approximately equal to any previous relative maximum value.

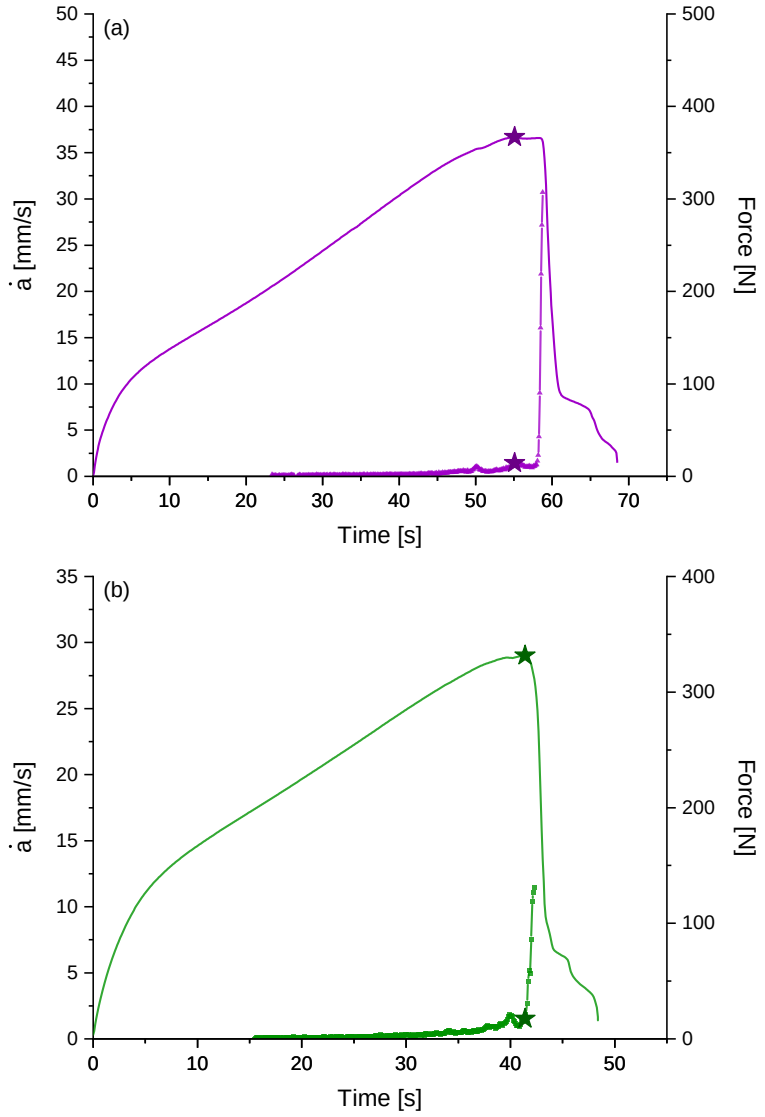

Figure 3.33. Force and crack growth rate as a function of time: (a) $\dot{a}_{F_{max}}$ located at the local maximum of $\dot{a} - t$ curve, (b) $\dot{a}_{F_{max}}$ located at the start of rapid increase of $\Delta\dot{a}$.

The mean values of the crack growth rate at F_{max} ($\dot{a}_{F_{max}}$) for the three materials are represented in Figure 3.34. In the case of $NBR_{NO\,PC}$, it is observed from Figure 3.32 that one specimen exhibits a very high value of $\dot{a}_{F_{max}}$ compared to the other specimens: this specimen was considered an outlier and was not included in the calculation of the average value.

It can be observed that the unstable fracture onset occurs when a similar value of crack growth rate is achieved. In the case of $NBR_{NO\ PC}$ a high dispersion in the data is obtained.

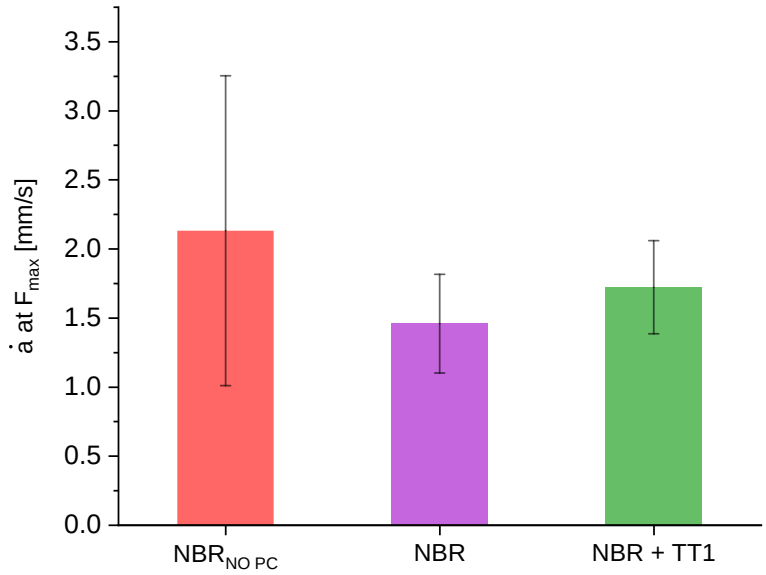

Figure 3.34. Mean values of $\dot{a}$ at maximum force for $NBR_{NO\ PC}$, NBR and NBR + TT1.

3.7. Formation of cavities

While performing the experimental tests, a whitening of the material was observed. During fracture tests the whitening occurred just in the region close to the notch tip of notched pure shear specimens; instead, in tensile tests on un-notched pure shear and dumbbell specimens a uniform whitening that increased with strain was observed along the specimen gauge length. In literature this whitening effect has been observed and studied mainly for rubber-toughened polymers (e.g., [56] [57] [58]) and silicone adhesives (e.g., [59]) and has been correlated to the formation of cavities in the rubber compound. It was therefore taken into consideration the hypothesis that the different behaviour at the start of unstable fracture was linked to a different susceptibility to the formation of cavities in the material.

A quantitative evaluation of the whitening of the samples was performed by analysing the videorecordings of the tests; the images were processed in grey mode using the ImageJ software and the mean grey scale intensity value of the central part of the

specimen was evaluated at different levels of deformation. Only uniaxial tensile tests were analysed; in the case of pure shear tests, the application of the black pattern needed for the DIC analysis made it impossible to achieve reliable results. The quantity that will be used to perform the comparison between the materials will be called whitening index and is given by

$$whitening\ index = \frac{G_{\varepsilon_i} - G_0}{G_0}\ 100 \tag{3.3}$$

in which G_{ε_i} and G_0 are the mean grey scale intensity at the deformation ε_i and of the undeformed specimen, respectively. The use of the relative percent difference allows the measurement not to be affected by the differences caused by variations in the lighting of different samples. This methodology allows to obtain only an indicative evaluation of the whitening effect, since the experimental setup and the lighting system is not optimized for this type of measurement. However, these evaluations are useful to perform a comparison between different materials. Moreover, similar methodologies have been used in literature (e.g., [58]) to assess the strain-induced whitening observed in rubber-toughened polymers.

The images used to perform the calculation were the ones corresponding to the monotonic and cyclic uniaxial tensile tests reported in Paragraph 3.1 and Paragraph 3.2, respectively. Only $NBR_{NO\ PC}$ and NBR + TT1 were considered. An example of the whitening observed at different levels of deformation on a specimen of $NBR_{NO\ PC}$ during an uniaxial tensile test is shown in Figure 3.35.

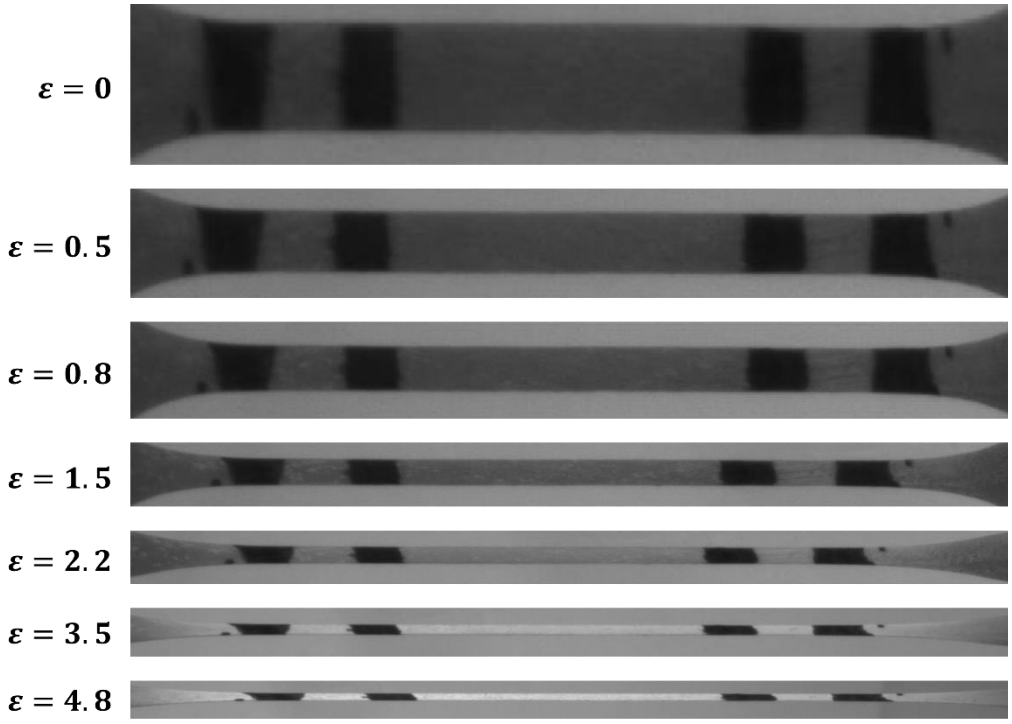

Figure 3.35. Images extracted from the videorecording of a uniaxial tensile test on $NBR_{NO\ PC}$ showing the whitening of the specimen.

The whitening index is represented as a function of the strain in Figure 3.36. It can be observed that both materials show an increase in the slope at approximately 150% strain. Another observation is that up to 220% strain the two materials show comparable behaviour, even though $NBR_{NO\ PC}$ seems to have a higher whitening index; at higher strains the two curves deviate, with NBR + TT1 showing a more pronounced increase of whitening index with the applied strain. This may suggest that in NBR + TT1 more cavities are formed, leading to premature failure with respect to $NBR_{NO\ PC}$. It should be considered that the observed whitening can also be influenced by a change in the refractive index caused by the orientation of the polymeric chains during the deformation.

One possible objection could be that the level of strain at which a difference between the two materials is observed is higher than the strains ε_{close} measured at F_{max}, which were around 106% for the $NBR_{NO\ PC}$ and 80% for the NBR + TT1 (see Figure 3.27). However, as reported in Paragraph 3.5.2, some difficulties were encountered in the measurement of the strain in close proximity to the crack tip due to the presence of the whitening. In particular, the distance along the notch plane at which the strains were

evaluated is bigger than the size of the whitened zone observed in fracture tests, which was evaluated to be smaller than 0.5 mm. It is assumed that the strains in this region will be higher than the ones measured through Digital Image Correlation. Moreover, the area near the crack tip is in a more complicated state of stress than the uniaxial tension for which the whitening was quantitatively evaluated: this may lead to formation of cavities at strains lower than what was observed in uniaxial tension. It was possible to evaluate the whitening index on one pure shear specimen of NBR + TT1 that was not treated with the black pattern needed for the DIC analysis. The comparison with the results obtained for uniaxial tension is shown in Figure 3.37. It can be observed that in pure shear loading condition the change in slope occurs at a lower strain than in uniaxial tension. Even if the data for $NBR_{NO\ PC}$ are missing, it can be assumed that the deviation between $NBR_{NO\ PC}$ and NBR + TT1 in pure shear loading conditions takes place at a lower strain level than those at which it occurs in uniaxial tension. Thus it is expected that for similar values of applied strains, more cavities are formed in NBR + TT1 than in $NBR_{NO\ PC}$. These assumptions should in any case be confirmed in the future by computing the whitening index in pure shear loading conditions also for $NBR_{NO\ PC}$ and by refining the methodology with which the whitening index is evaluated.

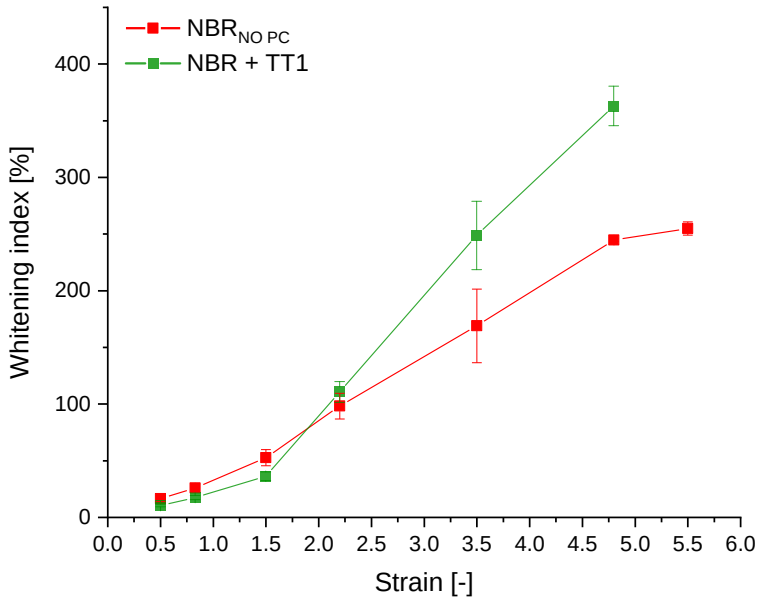

Figure 3.36. Whitening index in uniaxial tension as a function of strain for $NBR_{NO\ PC}$ and NBR + TT1.

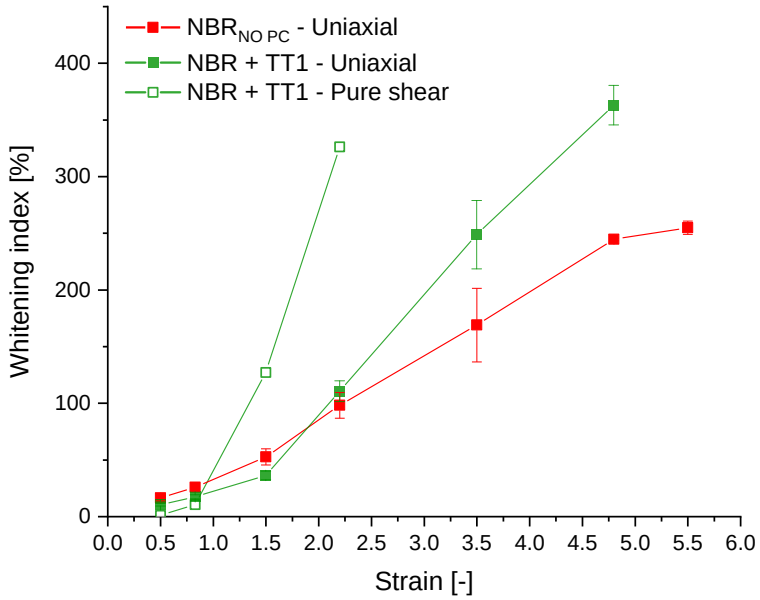

Figure 3.37. Whitening index in uniaxial tension (NBR$_{NO\ PC}$ and NBR + TT1) and pure shear loading conditions (NBR + TT1) as a function of strain.

3.8. Stress softening in pure shear loading condition

The effect of the strain induced softening on the fracture of the post-cured material (NBR) was assessed. The recovery effect of thermal treatment TT1 was also investigated.

Three loading-unloading cycles up to 250% strain were performed on six NBR un-notched pure shear specimens. The level of strain was higher than the one measured close to the notch tip ($\varepsilon > \varepsilon_{close}$), both at crack onset and at F_{max}. Three specimens were then notched and tested at fracture: in the following, they will be identified as NBR softened. Three more specimens were conditioned with TT1, then notched and tested at fracture: they will be identified as NBR softened + TT1.

Figure 3.38 reports the force-time curves of the fracture tests on NBR softened and NBR softened + TT1. For comparison, the results obtained from the fracture tests on NBR and NBR + TT1, already reported in Paragraph 3.5, are reported too. The dots and the stars indicate the crack onset and the maximum force, respectively. As expected, NBR softened shows lower force values with respect to NBR. As far as the unstable fracture, it seems to occur at a time similar to that of NBR. This may suggest that the kinetics of the propagation is not influenced by the softening, while it is strongly

influenced by the applied thermal history, as already observed in Paragraph 3.6. From the comparison between the curves of NBR softened and NBR softened + TT1, it is observed that TT1 induced only a partial recovery of the force-time curve. This result is different from what was observed in the uniaxial tensile tests: in that case, indeed, the thermal treatment allowed to recover almost completely the stress-strain curve. Further, the time at which the catastrophic fracture begins is decreased by the heat treatment, resulting close to that of the non-softened material after the same thermal treatment (NBR + TT1).

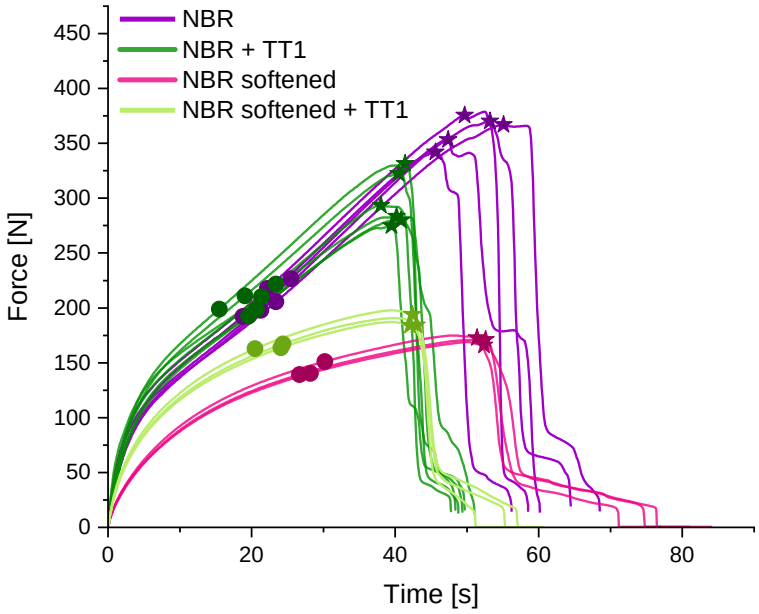

Figure 3.38. Force-time curves for NBR, NBR + TT1, NBR softened and NBR softened + TT1.

The J-integral at the crack onset of NBR softened and NBR softened + TT1 are represented in Figure 3.39 and compared to that of NBR and NBR + TT1. It can be observed that the softening causes a reduction in the fracture toughness evaluated as J_{onset}. Moreover, NBR softened and NBR softened + TT1 show comparable values of fracture toughness, meaning that the thermal treatment does not induce a complete recovery of the Mullins effect, despite what suggested by uniaxial tensile tests.

This is not in accordance with what was observed in Denora and Marano [60], who studied an HNBR filled with carbon black. The results showed that the same thermal

treatment allowed the recovery of both the uniaxial tensile stress-strain response and the fracture toughness evaluated at the crack onset.

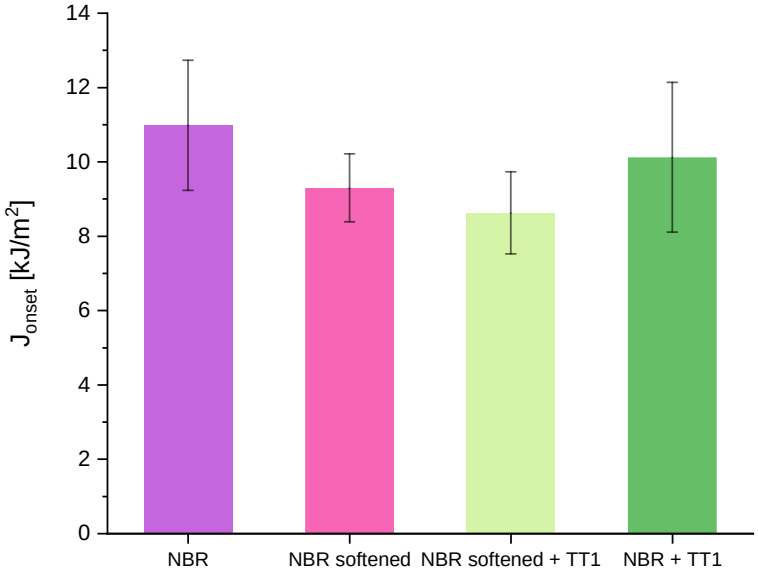

Figure 3.39. J-integral at crack onset for NBR, NBR softened and NBR softened + TT1.

Figure 3.40 shows the J-integral evaluated at the starting point of the unstable fracture. As seen for the crack onset, the softening causes a reduction in the fracture toughness evaluated as J at F_{max}, which is not recovered using thermal treatment TT1.

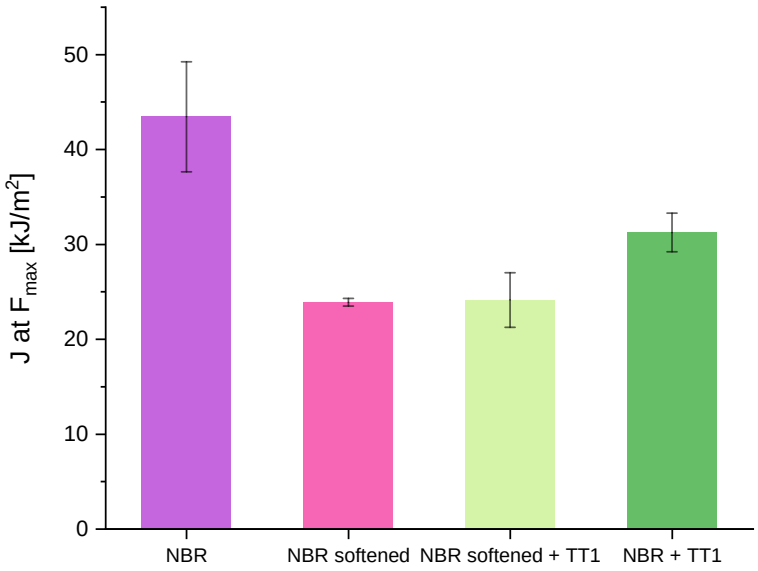

Figure 3.40. J-integral at start of unstable fracture for NBR, NBR softened and NBR softened + TT1.

The average values of the J-integral at the crack onset and at the start of unstable propagation are summarized in Table 3.9 and Table 3.10, respectively. The relative variation with respect to NBR was also computed. It is observed that the softening has a more significant effect on the unstable fracture than on the crack onset. A similar result was observed when dealing with the effect of the thermal treatment on the pristine material (see Table 3.6 and Table 3.7): this suggests that the unstable propagation of the crack is more sensitive to structural changes of the material than the crack onset.

Table 3.9. J-integral at crack onset and its relative variation with respect to NBR.

Material	J_{onset} [kJ/m²]	Relative variation of J_{onset} compared to NBR [%]
NBR	10.99 ± 1.75	-
NBR softened	9.30 ± 0.91	-15.3 ± 15.3
NBR softened + TT1	8.63 ± 1.10	-21.4 ± 16.0

Table 3.10. J-integral at start of unstable propagation and its relative variation with respect to NBR.

Material	$J_{unstable}$ [kJ/m²]	Relative variation of $J_{unstable}$ compared to NBR [%]
NBR	43.46 ± 5.80	-
NBR softened	23.90 ± 0.40	-45.0 ± 7.4
NBR softened + TT1	24.13 ± 2.87	-44.5 ± 9.9

Figure 3.41 and Figure 3.42 show Δa and $\dot{a}$ as a function of time, respectively. The mean values of these quantities evaluated at the starting point of unstable propagation are shown in Figure 3.43 and Figure 3.44. In the case of softened NBR + TT1, one of the specimens showed a very high value of both critical Δa and $\dot{a}$; this specimen was not considered for the calculation of the average values.

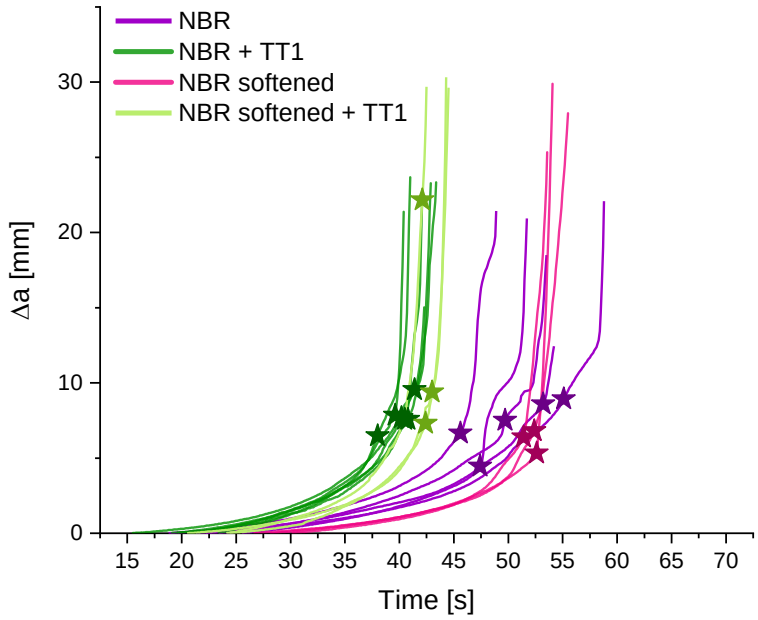

Figure 3.41. Δa as a function of time for NBR, NBR + TT1, NBR softened and NBR softened + TT1.

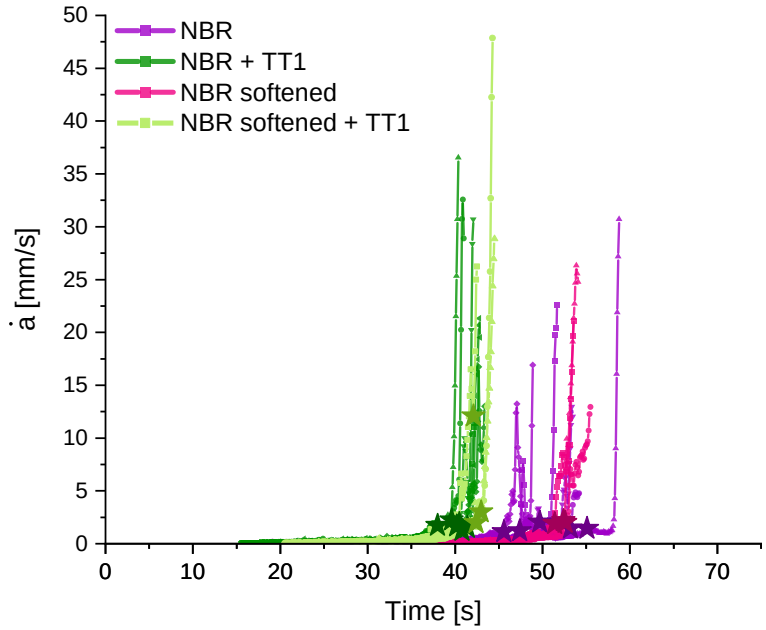

Figure 3.42. $\dot{a}$ as a function of time for NBR, NBR + TT1, NBR softened and NBR softened + TT1.

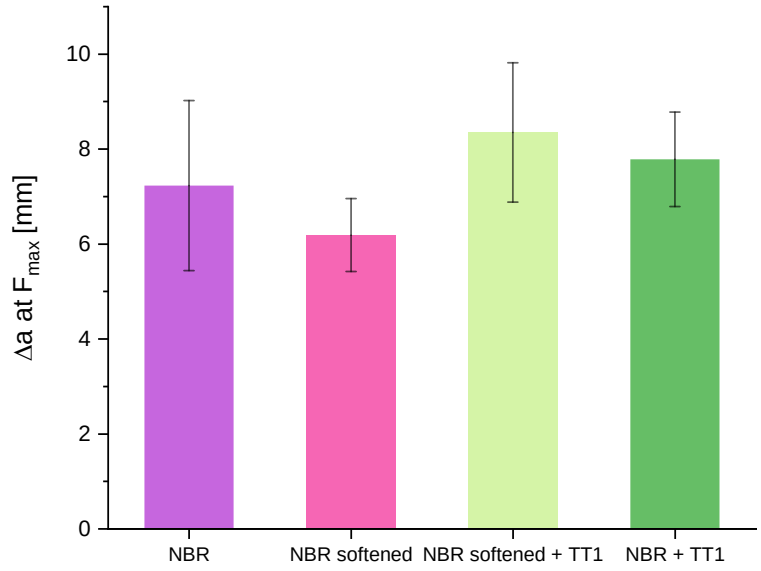

Figure 3.43. Δa at start of unstable propagation for NBR, NBR + TT1, NBR softened and NBR softened + TT1.

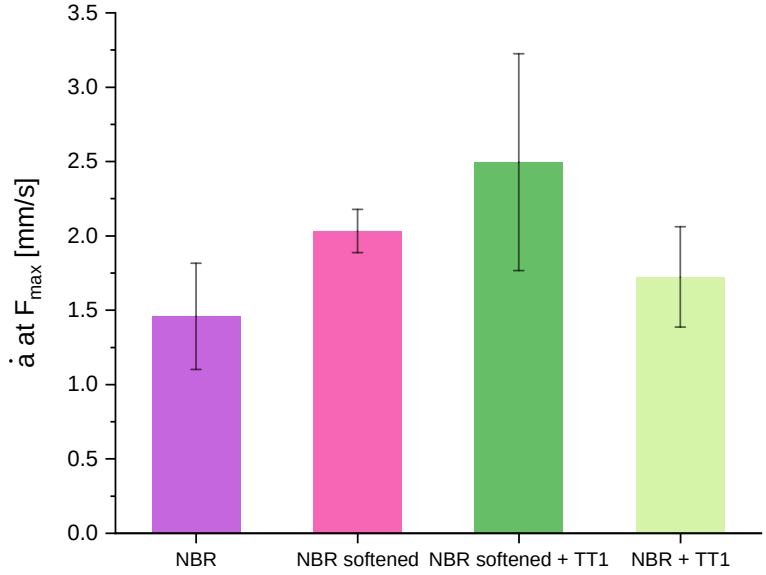

Figure 3.44. $\dot{a}$ at start of unstable propagation for NBR, NBR + TT1, NBR softened and NBR softened + TT1.

A statistical two-sample t-test with $\alpha = 0.05$ was performed in order to evaluate the statistical significance of the difference between the values obtained. The results for Δa and $\dot{a}$ are shown in Table 3.11 and Table 3.12, respectively.

It is observed that at the start of the unstable propagation all the materials show a comparable crack advancement, suggesting that the crack advancement is critical for the start of the unstable propagation.

The effect of the softening on the crack velocity can be evaluated from the comparison between NBR and NBR softened: an increase in the velocity of the crack at the start of unstable propagation is observed, while the crack advancement does not change. The comparison between NBR and softened NBR + TT1 shows that after the application of the recovery thermal treatment, the velocity of the crack returns to be comparable to the one of pristine NBR. However, this conclusion must be treated with caution, as the results of $\dot{a}$ of softened NBR + TT1 show a high variability: the result of the statistical t-test should therefore be confirmed with further tests.

Table 3.11. Results of statistical t-test performed on Δa.

Materials compared	p-value	Result
NBR – NBR softened	0.30	No significant difference
NBR + TT1 – NBR softened + TT1	0.68	No significant difference
NBR softened – NBR softened + TT1	0.25	No significant difference
NBR – NBR softened + TT1	0.47	No significant difference

Table 3.12. Results of statistical t-test performed on $\dot{a}$.

Materials compared	p-value	Result
NBR – NBR softened	0.02	Significant difference
NBR + TT1 – NBR softened + TT1	0.36	No significant difference
NBR softened – NBR softened + TT1	0.53	No significant difference
NBR – NBR softened + TT1	0.27	No significant difference

The J-integral applied between the crack onset and the start of unstable propagation is represented as a function of Δa in Figure 3.45. It is observed that the softening causes a decrease in the resistance to crack growth. Moreover, the application of TT1 to NBR softened does not induce a recovery of the resistance but actually causes a slight further decrease.

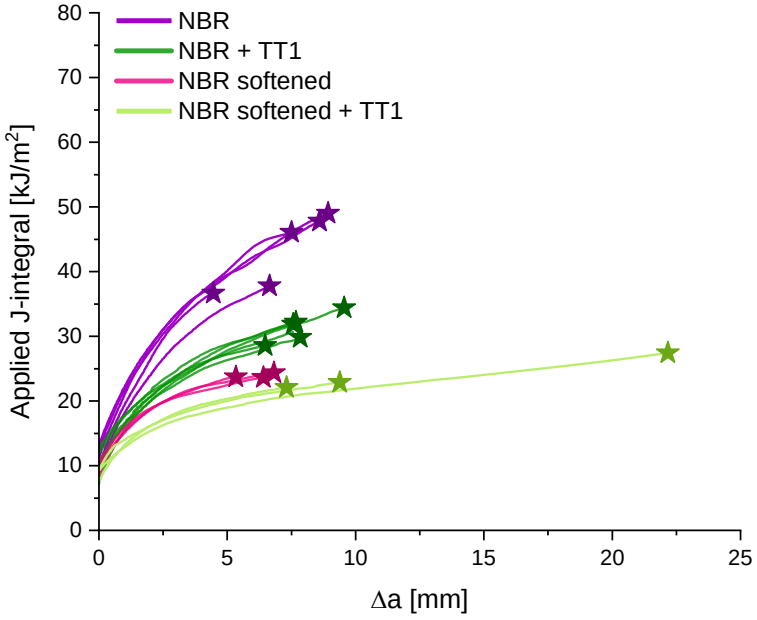

Figure 3.45. Applied J-integral after the crack onset as a function of Δa for NBR, NBR + TT1, NBR softened and NBR softened + TT1.

4 Conclusions and future developments

In this work, the mechanical behaviour of a NBR compound filled with silica was characterized. More specifically, the work started with the investigation of the strain-induced softening that is observed when a previously stretched rubber compound is deformed a second time; particular attention was put into the definition of a thermal treatment that allows to recover this effect. In order to better understand what this recovery implies, a study of the effects of the employed thermal treatments on the fracture behaviour was conducted. The effect of the strain-induced material softening on its fracture behaviour and toughness was evaluated. The ability of the material to recover its original fracture behaviour through a heat treatment was compared with its ability to recover its uniaxial tensile response through the same thermal treatment.

The main experimental activities and results are summarized below.

- The behaviour of the material in monotonic uniaxial tensile loading conditions was characterized focusing the attention on two different thermal treatments. It was assessed that both thermal treatments cause a change in the material response, suggesting that the crosslinking was most probably not completed during the curing process. The material was stabilized by applying a post-curing treatment and it was assessed that the two thermal treatments did not have a significant effect on the response of the post-cured material.
- The post-cured material was used to investigate the strain-induced softening effect. The two thermal treatments previously considered were used to verify the thermal recover of the stress softening. It was assessed that both thermal treatments allow to recovery almost completely the stress-strain behaviour of the pristine material.
- Attention was focused on the effects of one of the two thermal treatments, and a characterization of the dissipative behaviour of the material was performed

both in uniaxial tension and in pure shear configuration. This analysis was conducted comparing the not post-cured material and the post-cured and thermally treated material. It was assessed that both materials dissipate more in pure shear loading conditions than in uniaxial tension. In pure shear the two materials show a comparable behaviour, while in uniaxial tension the conditioned material showed a slightly higher dissipation.

- In order to gain further understanding of the structural changes induced by the thermal treatment used for the recovery of the stress softening, its effect on the fracture behaviour of the material was investigated. The post-cured and thermally treated material was compared with the post-cured and not post-cured ones. The effect on both the crack onset and the propagation of the crack was assessed. It was found that the thermal treatments have a more deleterious effect on the unstable propagation than on the crack onset. In particular, for the thermally treated materials the unstable propagation phase starts at shorter times and the J-integral applied when the unstable propagation starts is lower
- The kinetics of the stable crack growth was analysed by measuring the crack advancement as a function of time and evaluating the crack propagation velocity. Their values at the start of unstable crack propagation were calculated: it was observed that the values of crack advancement and crack propagation rate are the same, irrespective of the thermal history considered.
- An attempt to correlate the different behaviour at fracture to a different materials susceptibility to formation of cavities was made: the progressive whitening observed during the deformation was evaluated for differently heat treated materials, which showed a different response.
- The effect of the material softening induced in the pure shear configuration on the fracture behaviour of the post-cured material was investigated. The softening causes a reduction in the value of the applied J-integral, both at the crack onset and at the start of the unstable crack propagation. The effect of the same thermal treatment used to recovery the uniaxial tensile stress-strain behaviour was assessed. It was observed that it did not induce a recovery of the fracture toughness, neither at the crack onset nor at the start of the unstable propagation.

- The value of crack advancement needed to start the unstable propagation in pure shear fracture tests resulted to be unaffected by both the softening and the applied thermal treatments. This suggests that the crack advancement plays a critical role in the transition from stable to unstable crack propagation.

It must be emphasized how the results of the comparison between different materials can vary significantly depending on whether the analysis focuses on crack initiation or on the starting point of unstable propagation. For this reason, the Polymers4Hydrogen project, mentioned in the introduction of this thesis, is exploring a correlation between the fracture toughness and the results of rapid gas decompression by considering both the crack initiation and the starting point of unstable fracture.

In the future, further understanding of the critical role of the crack advancement on the start of the unstable propagation and its physical meaning should be gained. Additionally, further investigation is needed to understand why the thermal treatment that recovers the Mullins effect in uniaxial tension does not induce a recovery of the fracture properties. Finally, there is still much work to be done in studying the whitening effect and its relationship to cavity formation. Specifically, a more precise method of evaluating the whitening should be developed to quantitatively assess the phenomenon also in the region near the notch tip during fracture tests.

Bibliography

[1] R. L. Anthony, R. H. Caston, and E. Guth, "Equations of State for Natural and Synthetic Rubber-like Materials. I - Unaccelarated Natural Soft Rubber," *J Phys Chem*, vol. 46, no. 8, pp. 826–840, 1942, doi: 10.1021/j150422a005.

[2] L. R. G. Treloar, *The Physics of Rubber Elasticity*. Oxford University Press, 1975.

[3] L. Mullins, "Determination of Degree of Crosslinking in Natural Rubber Vulcanizates. Part IV. Stress-Strain Behavior at Large Extensions," *J Appl Polym Sci*, vol. 2, no. 6, pp. 257–263, 1959, doi: 10.1002/app.1959.070020601.

[4] J. E. Mark, B. Erman, and F. Eirich, Eds., *Science and Technology of Rubber*, Third. Elsevier Academic Press, 2005.

[5] A. N. Gent, *Engineering with Rubber - How to Design Rubber Components*, Third. Hanser Publications, 2012.

[6] G. Heinrich, M. Kluppel, and T. A. Vilgis, "Reinforcement of elastomers," *Curr Opin Solid State Mater Sci*, vol. 6, no. 3, pp. 195–203, 2002, doi: 10.1016/S1359-0286(02)00030-X.

[7] P. Bernal-Ortega, R. Anyszka, Y. Morishita, R. Di Ronza, and A. Blume, "Comparison between SBR Compounds Filled with In-Situ and Ex-Situ Silanized Silica," *Polymers (Basel)*, vol. 13, no. 2, pp. 1–15, 2021, doi: 10.3390/polym13020281.

[8] R. Scotti, M. D'Arienzo, B. Di Credico, L. Giannini, and F. Morazzoni, "Silica–Polymer Interface and Mechanical Reinforcement in Rubber Nanocomposites," in *Hybrid Organic-Inorganic Interfaces*, D. H. Delville and A. Taubert, Eds., 2018. doi: 10.1002/9783527807130.ch4.

[9] H. Lüchow, E. Breier, and W. Gronski, "Characterization of polymer adsorption on disordered filler surfaces by transversal 1H NMR relaxation," *Rubber Chemistry and Technology*, vol. 70, no. 5, pp. 747–758, 1997, doi: 10.5254/1.3538457.

[10] N. K. Dutta *et al.*, "High resolution solid-state n.m.r. investigation of the filler-rubber interaction: 1. High speed 1H magic-angle spinning n.m.r. spectroscopy in carbon black filled styrene-butadiene rubber," *Polymer (Guildf)*, vol. 35, no. 20, pp. 4293–4299, 1994, doi: 10.1016/0032-3861(94)90085-X.

[11] M. T. Loukil, G. Corvec, E. Robin, M. Miroir, J. B. Le Cam, and P. Garnier, "Stored energy accompanying cyclic deformation of filled rubber," *Eur Polym J*, vol. 98, pp. 448–455, 2018, doi: 10.1016/j.eurpolymj.2017.11.035.

[12] H. Bouasse and Z. Carrière, "Sur les courbes de traction du caoutchouc vulcanisé," *Annales de la Faculté des sciences de l'Université de Toulouse pour les sciences mathématiques et les sciences physiques*, vol. 5, no. 3, pp. 257–283, 1903.

[13] J. Diani, B. Fayolle, and P. Gilormini, "A review on the Mullins effect," *Eur Polym J*, vol. 45, no. 3, pp. 601–612, 2009, doi: 10.1016/j.eurpolymj.2008.11.017.

[14] L. Mullins, "Effect of stretching on properties of rubber," *Rubber Chemistry and Technology*, vol. 21, no. 2, pp. 275–289, 1947, doi: 10.5254/1.3546914.

[15] T. T. Mai, Y. Morishita, and K. Urayama, "Induced anisotropy by Mullins effect in filled elastomers subjected to stretching with various geometries," *Polymer (Guildf)*, vol. 126, pp. 29–39, 2017, doi: 10.1016/j.polymer.2017.08.012.

[16] A. Dorfmann and R. W. Ogden, "A constitutive model for the Mullins effect with permanent set in particle-reinforced rubber," *Int J Solids Struct*, vol. 41, no. 7, pp. 1855–1878, 2004, doi: 10.1016/j.ijsolstr.2003.11.014.

[17] L. Mullins and N. R. Tobin, "Theoretical model for the elastic behavior of filler-reinforced vulcanized rubbers," *Rubber Chemistry and Technology*, vol. 30, no. 2, pp. 555–571, 1957, doi: 10.5254/1.3542705.

[18] N. Suzuki, M. Ito, and F. Yatsuyanagi, "Effects of rubber/filler interactions on deformation behavior of silica filled SBR systems," *Polymer (Guildf)*, vol. 46, no. 1, pp. 193–201, 2005, doi: 10.1016/j.polymer.2004.10.066.

[19] D. E. Hanson *et al.*, "Stress softening experiments in silica-filled polydimethylsiloxane provide insight into a mechanism for the Mullins effect," *Polymer (Guildf)*, vol. 46, no. 24, pp. 10989–10995, 2005, doi: 10.1016/j.polymer.2005.09.039.

[20] J. A. C. Harwood and A. R. Payne, "Stress Softening in Natural Rubber Vulcanizates. Part IV. Unfilled Vulcanizates," *J Appl Polym Sci*, vol. 10, no. 8, pp. 1203–1211, 1966, doi: 10.1002/app.1966.070100811.

[21] G. Kraus, C. W. Childers, W. Rollmann, and D. Dapnrtmen, "Stress Softening in Carbon Black-Reinforced Vulcanizates. Strain Rate and Temperature Effects," *J Appl Polym Sci*, vol. 10, no. 2, pp. 229–244, 1966, doi: 10.1002/app.1966.070100205.

[22] R. Houwink, "Slipping of molecules during the deformation of reinforced rubber," *Rubber Chemistry and Technology*, vol. 29, no. 3, pp. 888–893, 1956, doi: 10.5254/1.3542602.

[23] E. M. Dannenberg and J. J. Brennan, "Strain energy as a criterion for stress softening in carbon-black filled vulcanizates," *Rubber Chemistry and Technology*, vol. 39, no. 3, pp. 597–608, 1966, doi: 10.5254/1.3544867.

[24] A. F. Blanchard and D. Parkinson, "Breakage of carbon-rubber networks by applied stress," *Ind Eng Chem*, vol. 44, no. 4, pp. 799–812, 1952, doi: 10.1021/ie50508a034.

[25] F. Bueche, "Molecular Basis for the Mullins Effect," *J Appl Polym Sci*, vol. 4, no. 10, pp. 107–114, 1960, doi: 10.1002/app.1960.070041017.

[26] F. Laraba-Abbes, P. Ienny, and R. Piques, "A new 'Tailor-made' methodology for the mechanical behaviour analysis of rubber-like

materials: II. Application to the hyperelastic behaviour characterization of a carbon-black filled natural rubber vulcanizate," *Polymer (Guildf)*, vol. 44, no. 3, pp. 821–840, 2003, doi: 10.1016/S0032-3861(02)00719-X.

[27] J. Plagge and M. Klüppel, "Mullins effect revisited: Relaxation, recovery and high-strain damage," *Mater Today Commun*, vol. 20, 2019, doi: 10.1016/j.mtcomm.2019.100588.

[28] Z. Li, H. Xu, X. Xia, Y. Song, and Q. Zheng, "Energy dissipation accompanying Mullins effect of nitrile butadiene rubber/carbon black nanocomposites," *Polymer (Guildf)*, vol. 171, pp. 106–114, 2019, doi: 10.1016/j.polymer.2019.03.043.

[29] A. A. Griffith, "The phenomena of rupture and flow in solids," *Philos Trans R Soc Lond*, vol. 221, pp. 163–198, 1920, doi: 10.1098/rsta.1921.0006.

[30] R. S. Rivlin and A. G. Thomas, "Rupture of Rubber. I. Characteristic Energy for Tearing," *Journal of Polymer Science*, vol. 10, no. 3, pp. 291–318, 1953, doi: 10.1002/pol.1953.120100303.

[31] J. R. Rice, "A path independent integral and the approximate analysis of strain concentration by notches and cracks," *J Appl Mech*, vol. 35, no. 2, pp. 379–386, 1968, doi: 10.1115/1.3601206.

[32] O. H. Yeoh, "Analysis of deformation and fracture of 'pure shear' rubber testpiece," *Plastics, Rubber and Composites*, vol. 30, no. 8, pp. 389–397, 2001, doi: 10.1179/146580101101541787.

[33] B. H. Kim and C. R. Joe, "Single specimen test method for determining fracture energy (Jc) of highly deformable materials," *Eng Fract Mech*, vol. 32, no. 1, pp. 155–161, 1989, doi: 10.1016/0013-7944(89)90213-0.

[34] A. N. Gent, "Cavitation in rubber: a cautionary tale," *Rubber Chemistry and Technology*, vol. 63, no. 3, pp. 49–53, 1990, doi: 10.5254/1.3538266.

[35] E. Elmukashfi, "An experimental method for estimating the tearing energy in rubber-like materials using the true stored energy," *Sci Rep*, vol. 11, no. 1, 2021, doi: 10.1038/s41598-021-95151-y.

[36] D. Roucou, J. Diani, M. Brieu, and A. Mbiakop-Ngassa, "Critical strain energy release rate for rubbers: single edge notch tension versus pure shear tests," *Int J Fract*, vol. 216, no. 1, pp. 31–39, 2019, doi: 10.1007/s10704-018-00336-8.

[37] A. N. Gent and P. B. Lindley, "Internal rupture of bonded rubber cylinders in tension," *Proc R Soc Lond A Math Phys Sci*, vol. 249, pp. 195–205, 1961, doi: 10.1098/rspa.1959.0016.

[38] A. E. Oberth and R. S. Bruenner, "Tear Phenomena around Solid Inclusions in Castable Elastomers," *Transactions of the Society of Rheology*, vol. 9, no. 2, pp. 165–185, 1965, doi: 10.1122/1.548997.

[39] A. N. Gent and B. Park, "Failure processes in elastomers at or near a rigid spherical inclusion," *J Mater Sci*, vol. 19, pp. 1947–1956, 1984, doi: 10.1007/BF00550265.

[40] O. Lopez-Pamies, M. I. Idiart, and T. Nakamura, "Cavitation in elastomeric solids: I - A defect-growth theory," *J Mech Phys Solids*, vol. 59, no. 8, pp. 1464–1487, 2011, doi: 10.1016/j.jmps.2011.04.015.

[41] M. L. Williams and R. A. Schapery, "Spherical flow instability in hydrostatic tension," *International Journal of Fracture Mechanics*, vol. 1, pp. 64–72, 1965, doi: 10.1007/BF00184154.

[42] V. Lefèvre, K. Ravi-Chandar, and O. Lopez-Pamies, "Cavitation in rubber: an elastic instability or a fracture phenomenon?," *Int J Fract*, vol. 192, no. 1, pp. 1–23, 2015, doi: 10.1007/s10704-014-9982-0.

[43] C. Creton and M. Ciccotti, "Fracture and adhesion of soft materials: A review," *Reports on Progress in Physics*, vol. 79, no. 4, 2016, doi: 10.1088/0034-4885/79/4/046601.

[44] E. Euchler *et al.*, "Cavitation in Rubber Vulcanizates Subjected to Constrained Tensile Deformation," in *Advances in Polymer Science*, 2021, pp. 203–224. doi: 10.1007/12_2020_65.

[45] J. De Crevoisier *et al.*, "Volume changes in a filled elastomer studied via digital image correlation," *Polym Test*, vol. 31, no. 5, pp. 663–670, 2012, doi: 10.1016/j.polymertesting.2012.04.003.

[46] C. E. Federico, G. Rauchs, O. Kotecky, S. Westermann, and F. Addiego, "Cavitation in thermoplastic-reinforced rubber composites upon cyclic testing: Multiscale characterization and modelling," *Polymer (Guildf)*, vol. 211, 2020, doi: 10.1016/j.polymer.2020.123084.

[47] C. E. Federico *et al.*, "Resolving cavitation in silica-filled styrene-butadiene rubber composites upon cyclic tensile testing," *Polym Test*, vol. 100, 2021, doi: 10.1016/j.polymertesting.2021.107274.

[48] L. B. Tunnicliffe, A. G. Thomas, and J. J. C. Busfield, "Light scattering and transmission studies of nanofiller particulate size, matrix cavitation, and high strain interfacial dewetting behavior in silica-elastomer composites," *J Polym Sci B Polym Phys*, vol. 49, no. 15, pp. 1084–1092, 2011, doi: 10.1002/polb.22285.

[49] S. Géhant and R. Schirrer, "Multiple Light Scattering and Cavitation in Two Phase Tough Polymers," *J Polym Sci B Polym Phys*, vol. 37, no. 2, pp. 113–126, 1999, doi: 10.1002/(sici)1099-0488(19990115)37:2<113::aid-polb2>3.0.co;2-p.

[50] BS ISO 37:2017, *Rubber, vulcanized or thermoplastic — Determination of tensile stress-strain properties*.

[51] R. Calabrò, "Mechanical characterization of elastomers under quasi-static and dynamic biaxial loading conditions," Phd Thesis, Politecnico di Milano, 2013.

[52] P. J. Flory and J. Rehner, "Statistical mechanics of cross-linked polymer networks II. Swelling," *J Chem Phys*, vol. 11, no. 11, pp. 521–526, 1943, doi: 10.1063/1.1723792.

[53] J. Brandrup, E. H. Immergut, and E. A. Grulke, *Polymer handbook*. Wiley, 1999.

[54] H. Schreier, J.-J. Orteu, and M. A. Sutton, *Image Correlation for Shape, Motion and Deformation Measurements*. Boston, MA: Springer US, 2009. doi: 10.1007/978-0-387-78747-3.

[55] B. Pan, H. Xie, Z. Wang, K. Qian, and Z. Wang, "Study on subset size selection in digital image correlation for speckle patterns," *Opt Express*, vol. 16, no. 10, pp. 7037–7048, 2008, doi: 10.1364/OE.16.007037.

[56] D. Dompas, G. Groeninckx, M. Isogawa, T. Hasegawa, and M. Kadokura, "Toughening behaviour of rubber-modified thermoplastic polymers involving very small rubber particles: 2. Rubber cavitation behaviour in poly(vinyl chloride)/methyl methacrylate-butadiene-styrene graft copolymer blends," *Polymer (Guildf)*, vol. 35, no. 22, pp. 4750–4759, 1994, doi: 10.1016/0032-3861(94)90728-5.

[57] C. B. Bucknall and R. R. Smith, "Stress-whitening in High-impact Polystyrenes," *Polymer (Guildf)*, vol. 6, no. 8, pp. 437–446, 1965, doi: 10.1016/0032-3861(65)90028-5.

[58] H. Nathani, A. Dasari, and R. D. K. Misra, "On the reduced susceptibility to stress whitening behavior of melt intercalated polybutene-clay nanocomposites during tensile straining," *Acta Mater*, vol. 52, no. 11, pp. 3217–3227, 2004, doi: 10.1016/j.actamat.2004.03.021.

[59] M. Drass, J. Muth, C. Louter, and J. Schneider, "Stress whitening effects in transparent structural silicone adhesives," *Glass Structures and Engineering*, vol. 4, no. 3, pp. 433–448, 2019, doi: 10.1007/s40940-019-00102-9.

[60] I. Denora and C. Marano, "Fracture behavior of filled elastomers: How do strain induced softening and its thermally induced recovery affect the fracture toughness?," in *Constitutive Models for Rubber XII*, CRC Press, 2022, pp. 321–327. doi: 10.1201/9781003310266-53.

List of Figures

Figure 1.1. Stress-temperature curves obtained for natural rubber at elongations ranging between 3% and 38% [1]. 4
Figure 1.2. Comparison between the constitutive equation of elasticity (continuous line) and experimental data (dotted line) [2]. 6
Figure 1.3. Mooney-Rivlin plots for natural rubber. Curves from (a) to (e) correspond to rubbers with increasing crosslink density [3]. 7
Figure 1.4. Schematic representation of crosslinked chains [4]. 9
Figure 1.5. Qualitative representation of torque-time curves obtained from dynamical mechanical tests [5]. 10
Figure 1.6. Mechanical response of NBR during cyclic uniaxial tests: (a) unfilled NBR; (b) NBR filled with 35 phr of carbon black[11]. 12
Figure 1.7. Stress-strain response of a 50 phr carbon-black filled SBR submitted to simple uniaxial tension and to cyclic uniaxial tension with increasing maximum strain every five cycles [13]. 14
Figure 1.8. Percentage recovery of the stress needed to reach 200% elongation as a function of recovery time and thermal treatment temperature [14]. 16
Figure 1.9. Stress-strain response of a 50 phr carbon-black filled SBR submitted to cyclic uniaxial tension in virgin state and in pre-stretched state after 3 and 17 h exposures to 80 °C [13]. 17
Figure 1.10. Specimen geometries used for the investigation of rubber fracture: (a) Trousers specimen; (b) pure shear specimen; (c) angled specimen; (d) split specimen [34]. 20
Figure 1.11. Pure shear specimen with a notch of length a [35]. 20
Figure 1.12. Definitions of unstable crack propagation starting point from literature: (a) in correspondence with the rapid force decrease [36]; (b) in correspondence with the force deviation from the monotonic increase [35]. 21
Figure 2.1. Torque-time curve for the NBR/silica compound supplied by Arlanxeo. 28

Figure 2.2. Geometry and dimensions of dumbbell specimens. Dimensions are in millimeters. 28
Figure 2.3. Geometry and dimensions (above) and aluminium clamping system (below) of pure shear specimens. Dimensions are in millimeters [51]. 29
Figure 2.4. Thermal histories of the materials used in this thesis work: (a) $NBR_{NO\ PC}$; (b) NBR; (c) NBR + TT1; (d) NBR + TT2. 30
Figure 2.5. Comparison between the strain obtained from DIC analysis and from crosshead displacement for a single cycle test in pure shear configuration. 33
Figure 2.6. Patterns with different speckle size and density [55]. 36
Figure 3.1. Stress-strain curves (T = 23 °C, $\varepsilon = 0.05\ s - 1$) for $NBR_{NO\ PC}$, $NBR_{NO\ PC}$ + TT1 , $NBR_{NO\ PC}$ + TT2. 40
Figure 3.2. Mooney-Rivlin plots for $NBR_{NO\ PC}$, $NBR_{NO\ PC}$ + TT1 and $NBR_{NO\ PC}$ + TT2 with the indication of the reduced stress upturn point. 41
Figure 3.3. Stress-strain curves (T = 23 °C, $\varepsilon = 0.05\ s - 1$) for NBR, NBR + TT1 and NBR + TT2. 42
Figure 3.4. Mooney-Rivlin plots for NBR, NBR + TT1 and NBR + TT2 with the indication of the reduced stress upturn point. 42
Figure 3.5. Crosslink density of $NBR_{NO\ PC}$, NBR and NBR + TT1. 44
Figure 3.6. Stress-strain curves (T = 23 °C, $\varepsilon = 0.05\ s - 1$) for $NBR_{NO\ PC}$, NBR and NBR + TT1. 44
Figure 3.7. Stress-strain curves obtained from single cycle loading-unloading uniaxial tensile tests (T = 23 °C, $\varepsilon = 0.05\ s - 1$) on $NBR_{NO\ PC}$ and NBR + TT1. 45
Figure 3.8. Elastically stored and dissipated energy components in uniaxial tension as a function of maximum strain for $NBR_{NO\ PC}$ and NBR + TT1. 46
Figure 3.9. Stress-strain curves obtained from single cycle loading-unloading tests in pure shear loading conditions on $NBR_{NO\ PC}$ and NBR + TT1. 47
Figure 3.10. Elastically stored and dissipated energy components in pure shear configuration as a function of maximum strain for $NBR_{NO\ PC}$ and NBR + TT1. 47
Figure 3.11. Dissipated energy component for tests in pure shear loading conditions and uniaxial tension on $NBR_{NO\ PC}$ and NBR + TT1. 48
Figure 3.12. Cyclic uniaxial tensile stress-strain curve (T = 23 °C, $\varepsilon = 0.05\ s - 1$) for NBR. 49

Figure 3.13. Input, stored and dissipated energy as a function of the number of deformation cycles for a specimen of NBR. 49
Figure 3.14. Stress-strain curves of two uniaxial tensile loading-unloading cycles for pristine NBR and NBR softened and thermally treated with TT1. 50
Figure 3.15. Stress-strain curves of two uniaxial tensile loading-unloading cycles for pristine NBR and NBR softened and thermally treated with TT2. 51
Figure 3.16. Force-time curves obtained from pure shear fracture tests: (a) $NBR_{NO\ PC}$; (b) NBR; (c) NBR + TT1. 53
Figure 3.17. Force and crack advancement as a function of time for $NBR_{NO\ PC}$: (a) loading stop before reaching F_{max}; (b) loading stop immediately after F_{max}. 55
Figure 3.18. J-integral applied up to the crack onset as a function of time for $NBR_{NO\ PC}$, NBR and NBR + TT1. 56
Figure 3.19. J-integral at crack onset for $NBR_{NO\ PC}$, NBR and NBR + TT1. 57
Figure 3.20. Strain distribution along the notch plane at crack onset. The dashed line indicates the distance from the notch tip at which $\varepsilon close$ was measured. 59
Figure 3.21. Whitening observed near the notch tip of NBR + TT1 during a fracture test. 59
Figure 3.22. Strains at crack onset measured at a distance of 1.30 mm from the notch tip. 60
Figure 3.23. Strains at crack onset measured far from the notch tip. 60
Figure 3.24. Force-time curve of $NBR_{NO\ PC}$, NBR and NBR + TT1 with the indication of the point of maximum force. 61
Figure 3.25. J-integral at F_{max} for $NBR_{NO\ PC}$, NBR and NBR + TT1. 62
Figure 3.26. Strains along the notch plane at start of unstable fracture. The dashed line indicates a distance of 1.27 mm from the notch tip. 64
Figure 3.27. Strains at F_{max} measured at a distance of 1.27 mm from the notch tip. 64
Figure 3.28. Strains at F_{max} measured far from the notch tip. 65
Figure 3.29. Crack advancement of $NBR_{NO\ PC}$, NBR and NBR + TT1 as a function of time with the indication of the starting point of unstable propagation. 66
Figure 3.30. Crack advancement at the starting point of the unstable propagation for $NBR_{NO\ PC}$, NBR and NBR + TT1. 67

Figure 3.31. Applied J-integral after the crack onset as a function of Δa for NBR$_{NO\ PC}$, NBR and NBR + TT1. 68
Figure 3.32. Crack growth rate with the indication of the starting point of unstable propagation: (a) NBR$_{NO\ PC}$, (b) NBR, (c) NBR + TT1, (d) comparison between the three materials..... 70
Figure 3.33. Force and crack growth rate as a function of time: (a) $aFmax$ located at the local maximum of $a - t$ curve, (b) $aFmax$ located at the start of rapid increase of Δa. 71
Figure 3.34. Mean values of a at maximum force for NBR$_{NO\ PC}$, NBR and NBR + TT1. 72
Figure 3.35. Images extracted from the videorecording of a uniaxial tensile test on NBR$_{NO\ PC}$ showing the whitening of the specimen. 74
Figure 3.36. Whitening index in uniaxial tension as a function of strain for NBR$_{NO\ PC}$ and NBR + TT1. 75
Figure 3.37. Whitening index in uniaxial tension (NBR$_{NO\ PC}$ and NBR + TT1) and pure shear loading conditions (NBR + TT1) as a function of strain. 76
Figure 3.38. Force-time curves for NBR, NBR + TT1, NBR softened and NBR softened + TT1. 77
Figure 3.39. J-integral at crack onset for NBR, NBR softened and NBR softened + TT1. 78
Figure 3.40. J-integral at start of unstable fracture for NBR, NBR softened and NBR softened + TT1. 78
Figure 3.41. Δa as a function of time for NBR, NBR + TT1, NBR softened and NBR softened + TT1. 80
Figure 3.42. a as a function of time for NBR, NBR + TT1, NBR softened and NBR softened + TT1. 80
Figure 3.43. Δa at start of unstable propagation for NBR, NBR + TT1, NBR softened and NBR softened + TT1. 81
Figure 3.44. a at start of unstable propagation for NBR, NBR + TT1, NBR softened and NBR softened + TT1. 81
Figure 3.45. Applied J-integral after the crack onset as a function of Δa for NBR, NBR + TT1, NBR softened and NBR softened + TT1. 83

List of Tables

Table 1.1. Summary of the experimental parameters used in literature for the investigation of the thermal recovery of the Mullins effect. 18
Table 2.1. Main components of the studied rubber compound. 27
Table 2.2. Summary of the materials and thermal treatments used in this thesis. 31
Table 3.1. Mean reduced stress and strain at upturn for $NBR_{NO\ PC}$, $NBR_{NO\ PC}$ + TT1 and $NBR_{NO\ PC}$ + TT2. 41
Table 3.2. Mean reduced stress and strain at upturn point for NBR, NBR + TT1 and NBR + TT2. 43
Table 3.3. J-integral at stable fracture onset for $NBR_{NO\ PC}$, NBR and NBR + TT1. 56
Table 3.4. Results of the statistical t-test performed on the J-integral at crack onset. . 57
Table 3.5. Results of the statistical t-test performed on the strains at crack onset far from the notch tip. 60
Table 3.6. J-integral at crack onset and its relative variation with respect to $NBR_{NO\ PC}$. 62
Table 3.7. J-integral at F_{max} and its relative variation with respect to $NBR_{NO\ PC}$. 63
Table 3.8. Elastically stored and dissipated J-integral up to F_{max} for $NBR_{NO\ PC}$ and NBR + TT1. 66
Table 3.9. J-integral at crack onset and its relative variation with respect to NBR. 79
Table 3.10. J-integral at start of unstable propagation and its relative variation with respect to NBR. 79
Table 3.11. Results of statistical t-test performed on Δa. 82
Table 3.12. Results of statistical t-test performed on a. 82